BRNO UNIVERSITY OF TECHNOLOGY

VYSOKÉ UČENÍ TECHNICKÉ V BRNĚ

FACULTY OF MECHANICAL ENGINEERING

FAKULTA STROJNÍHO INŽENÝRSTVÍ

INSTITUTE OF SOLID MECHANICS, MECHATRONICS AND BIOMECHANICS

ÚSTAV MECHANIKY TĚLES, MECHATRONIKY A BIOMECHANIKY

DEVELOPMENT OF A METHODOLOGY FOR FATIGUE CRACK LENGTH DETERMINATION USING DIGITAL IMAGE CORRELATION

VÝVOJ METODIKY PRO STANOVENÍ DÉLKY ÚNAVOVÉ TRHLINY POMOCÍ KORELACE DIGITÁLNÍCH OBRAZŮ

DOCTORAL THESIS

DIZERTAČNÍ PRÁCE

AUTHOR — Ing. Bořek Ščerba

AUTOR PRÁCE

SUPERVISOR — doc. Ing. Tomáš Návrat, Ph.D.

ŠKOLITEL

BRNO 2025

Abstract

Stopping fatigue tests for visual readings is labor-intensive and conflicts with uninterrupted acquisition recommended in fatigue crack growth rate standards. Furthermore, measuring fatigue crack length during ongoing tests reduces operator workload and enables automation. This thesis develops a digital image correlation (DIC)–based methodology that replaces visual inspection with a traveling microscope (VIM) and validates it against VIM data across materials, specimen sizes and types, and load levels, while also comparing it with a DIC thresholding approach, the Strain threshold method (STM). Sensitivity to input parameters is analyzed, limitations are identified, and user recommendations are formulated. The core estimator is a physics-based Inflection point method (IPM) and its fast, filtered implementation (fIPMf).

The workflow is as follows. DIC provides displacements via software-defined "virtual extensometers" laid out along the expected crack path. The resulting curve is a projection of crack opening displacements. Gaussian Process Regression—used here to mitigate spatial noise—fits this curve, and the inflection point of the fitted curve is taken as the crack tip (IPM). Its fast implementation (fIPM) restructures processing and reduces computation time by 55%; the filtered variant (fIPMf) adds an adaptive Kalman filter with a soft-monotonicity safeguard to stabilize the time series, reducing temporal noise by about an order of magnitude to sub-micrometer levels.

Validation used compact tension and middle tension specimens, with all the methods (VIM, IPM, and STM) applied to the same images acquired from the same side of the specimen, removing through-thickness bias from unequal crack lengths. The first validation compared crack-length results on images acquired during test stoppages. In this setting, IPM matched the VIM baseline with a root-mean-square error (RMSE) of 31 μm, while STM reached 274 μm. The most important sensitivity finding was the negligible load dependence of IPM, in contrast to STM.

An additional validation compared crack-growth-rate results from VIM and fIPMf on the same samples measured sequentially. VIM data were fitted with the NASGRO equation and used as a baseline; fIPMf results deviated by approximately 20-30%, which is comparable to the spread among VIM datasets themselves. For real-time use, fIPMf offers the same data-processing frequency as STM, which is more than 10× higher than for full-field DIC.

In summary, the proposed methodology enables non-interruptive, VIM-comparable crack-length and crack-growth evaluation during running tests and outperforms STM by a large margin. It offers a processing speed of about 20 frames/s. Key benefits include a threshold-free, physics-based estimator; robust adaptive fitting and filtering that learn during the test and react to changing conditions; and negligible load-level sensitivity, enabling K-decreasing tests to identify the stress intensity factor threshold—something difficult with STM.

Keywords (alphabetical order)

Crack opening displacement (COD) profile; Digital image correlation (DIC) for fatigue testing; Fatigue crack length measurement in metals; Fatigue crack growth rate evaluation; Inflection point method for crack-tip localization (IPM); Strain threshold method (STM); Virtual extensometers for crack monitoring; Visual inspection with a traveling microscope (VIM).

Bibliographic Citation

ŠČERBA, Bořek. *Development of a Methodology for Fatigue Crack Length Determination using Digital Image Correlation*. Online, doctoral Thesis. Tomáš NÁVRAT (supervisor). Brno: Brno University of Technology, Faculty of Mechanical Engineering, 2025. Available at: https://www.vut.cz/en/students/final-thesis/detail/163150. [accessed 2025-08-30].

Statement of Honor

I declare that I have independently completed this dissertation under the supervision of doc. Ing. Tomáš Návrat, Ph.D., using my own knowledge and the literature listed in the references.

In Třinec, on August 30, 2025 …….

Ing. Bořek Ščerba

Acknowledgement

I would like to thank my supervisor, Tomáš Návrat, for his guidance, patience, and constructive feedback throughout the preparation of this thesis. I am also grateful to X-Sight for their support and for providing a stimulating working environment, and to the Institute of Physics of Materials, Brno (Czech Academy of Sciences), for providing access to facilities, samples, a validation dataset, and valuable consultations. Last but not least, I thank my wife, Veronika, and my three daughters, Nora, Klára, and Sára, for their patience, understanding, and constant support during the preparation of this thesis.

Content

1 Introduction

Building and construction have always been part of human nature, from flint tools to the wheel, leading to the creation of trains, ships, and airplanes. When a machine, device, or tool is created, it should reliably perform its function. Any malfunction can cause damage, harm, or even loss of human life. Cracks that lead to premature fractures are one of the most common causes of structural failure and are described as "a major and perplexing problem in all structures" [1]. The significance of this problem increased with the advent of the industrial revolution and the increased use of iron and steel. During this time, the first articles and pioneering works on the topic began to appear, such as [2], [3], [4], and, in the twentieth century, [5], [6], [7].

However, it was Griffith's work ([8], [9]) that formed "the foundation of modern fracture theory"[10]. Since then, many quantitative approaches to evaluate the effect of cracks have been proposed. Notable contributions include Irwin [11], [12] and Orowan [13] in linear elastic fracture mechanics, Wells [14] and Rice [15] in the field of elastic plastic fracture mechanics, and Paris [16] in fatigue crack propagation. The crack length is one of the most crucial parameters in these approaches, making it essential to master its measurement in related experiments.

Many traditional methods for measuring crack length have been developed, continuously improved, and are still widely used for both monotonic and cyclic tests. Examples of these methods[1] include the compliance method, the electric potential drop technique, the foil strain gauge approach, the crack opening displacement (COD) technique, and the extensively used Visual inspection method (VIM) among non-contact approaches.

When VIM is utilized to determine the length of a crack in a fatigue test, a traveling microscope, or an equivalent magnifying device[2] is used to identify the crack tip. The position of the crack tip is determined by using, for example, a fine optical grid created beforehand on the sample [17] or a digital indicator associated with the optical device [18]. This is performed manually by a technician, who must stop the test before collecting the necessary values. This conventional non-contact method raises the question: Can the crack length be measured without stopping the test, as recommended by the relevant standard [19]? Achieving this could reduce operator workload, simplify the measurement process, and enable a higher level of automation. Digital image correlation (DIC) might provide a solution to this challenge.

Digital image correlation (DIC) is an optical method used to track full-field 2D or 3D displacements on the surface of a test specimen during a mechanical test [20]. Since its introduction in the early 1980s [21], DIC algorithms have significantly advanced, evolving into one of the most robust non-destructive techniques for measuring surface deformation across various experimental mechanics applications [22], some of which will be detailed later in this chapter.

Compared to conventional contact displacement or strain gauges, digital image correlation (DIC) offers a full-field approach that is better suited to describe heterogeneous deformations. When compared to other full-field optical methods for deformation measurements, such as holographic interference, electronic speckle pattern interferometry, or speckle photography, DIC provides several advantages.

[1] which will be discussed and referenced in section 2.1.

[2] e.g., a charge-coupled device camera with a wide-angle lens and extension tubes or spacer rings to increase the optical system’s magnification.

These include relatively simple preparation of the measuring system, lower requirements for the experimental environment allowing for easy outside-the-laboratory testing, no need for a laser light source, a high degree of automation in measurement and data processing, and compatibility with various magnifying instruments or other devices [22]. Additionally, the technique is independent of the tested material and the scale of testing, ranging from macroscale to the order of nanometers [20] [23].

Recently, the equipment needed to acquire quality images for DIC has become widely affordable. Additionally, low-resolution cameras[3] are sufficient for precise measurements, as DIC algorithms use subpixel interpolation to enhance accuracy [24], making it a cost-effective solution. The availability of many open-source codes (e.g., AL-DIC, Ncorr, PReDIC) and commercial software (e.g., VIC from Correlated Solutions, GOM from Zeiss, Alpha from Czech developer X-Sight) has facilitated its rapid adoption in both industry and the scientific community, expanding its application to various areas and presenting new challenges.

DIC plays a crucial role in modern mechanical testing. In material testing, it is commonly found in tensile testing laboratories as part of video-extensometers, which replace traditional extensometers. These are used to determine Young's modulus and Poisson's ratio, even at elevated temperatures up to 1100 °C [25]. Additionally, it is also used to measure the coefficient of thermal expansion [26] among basic mechanical properties. DIC has also significantly contributed to the development and deeper understanding of fracture mechanics, enabling the determination of the stress intensity factor (SIF) [27], Williams' expansion [28], J-integral [29] and the exploration of fatigue crack propagation [30]. DIC is also utilized to validate finite element models of processes [31] and components [32]. Furthermore, it is employed in vibration measurements using high-speed [33] or even low-speed [34] cameras.

[3] starting from resolutions below 1 megapixel, e.g., the FLIR Blackfly S offers a 0.4-megapixel variant [153].

2 Literature Review: Crack Length Measurement

To provide a comprehensive overview of crack length measurement, this Chapter first outlines conventional approaches, followed by those based on digital image correlation.

2.1 Conventional Methods

The well-known conventional testing technique for monitoring subcritical crack growth is based on changes in elastic compliance. It is simple to use, as it involves measuring two fundamental quantities in solid mechanics: applied load and specimen deflection [35]. This technique has been recognized since the work of Irwin and Kies in the 1960s [36]. Since then, the approach has been further developed, with multiple corrections proposed for standard test specimens, as reviewed in [35].

Another method is the electric potential drop. This technique "involves applying a constant current through a cracked specimen in such a way that a change in crack length alters the potential difference" [37]. Both direct current (DCPD) and alternating current (ACPD) can be used. The DCPD approach is simpler, as it does not require advanced electronics, but it necessitates higher accuracy in voltage measurement; whereas the ACPD approach requires more complex electronics but is less demanding in terms of voltage measurement accuracy [37].

In the work of Deans and Richards [38], a method was published to assess crack length from strain gauge measurements on the back face[4] of the compact tension (CT) or T-type wedge opening loading (WOL) specimen. This method is called the back-face strain. From the measured compressive strain, the crack length is calculated using the proposed equations.

The crack length can also be measured using foil strain gauges, such as those with wires that break as the crack grows [39], providing discrete information on its length, or strain gauges marketed under the commercial name KRAK-GAGE. In short, it is a "bondable, thin, electrically insulated metal foil of certain dimensions, photo-etched from a constantan alloy" [40] and was first reported by Paris and Hayden [41]. The KRAK-GAGE applies the principle of the DCPD method to an external body, which has significantly lower resistance than the sample itself, allowing higher direct current to be applied and a higher output voltage to be obtained.

The crack opening displacement (COD) method[5] can be used to determine crack length not only in static testing [42], but also in fatigue crack growth rate (FCGR) testing [43]. Displacement is typically measured by clip gauges or linear voltage displacement gauges, positioned between two points on the loading axis of the specimen, or on the front face in the case of bending[6], WOL, or CT specimens [38]. In the latter case, the notched arms of the clip gauges fit over the knife edges manufactured into the specimen [43]. The crack length is then derived based on established dependencies.

All these techniques, including VIM as presented in the Introduction, are recommended in the fatigue testing standard [44]. Some are also recommended in another fatigue testing standard [19] as well as in fracture toughness standards [45], [46].

[4] meaning the face opposite the notch.
[5] or the crack-mouth-opening-displacement method, depending on the measurement location.
[6] such as single-edge notched bending (SENB).

Next, other methods noted in the literature include: The ultrasonic method [47] uses high-frequency sound, with the reflected amount influenced by the length of the crack. The acoustic emission method [42] converts the elastic energy released during crack movement into electrical signals. Infrared thermography [48] detects thermoelastic stresses at the crack tip.

Among optical methods, Electronic speckle pattern interferometry [49] utilizes laser beams, while caustics [50] analyze light reflected by out-of-plane deformation near the crack tip. Moiré interferometry [51] is based on the interference of reference and deformed gratings. Reflection photoelasticity [52] employs birefringent coatings on the sample, creating fringe patterns when loaded. Holographic interferometry [53] relies on the interference of coherent light split into two beams. Lastly, DIC–based approaches, detailed in section 2.2, represent another important non-contact group of methods.

2.2 DIC-Based Approaches

Regarding DIC-based techniques, Mathieu et al. [54] use full-field 2D DIC measurement, where the displacement fields obtained in the anticipated crack propagation area are fitted into the Williams series [55], using only the terms relevant for small-scale yielding[7]. The results of the optimization provide the crack length and SIF. This method is quite computationally demanding, as the calculation of sixty image series takes 3-5 hours. Abanto-Bueno and Lambros [56] employ a similar approach but utilize a different function to describe the deformation around the crack tip, which is specific to their study. Yates et al. [57] also use the full-field displacement field and the Williams series but include more terms in the series (up to 15).

Réthoré et al. [58] integrate the shape functions used in X-FEM[8] into the DIC algorithm, enabling a more accurate description of discontinuities in the 2D DIC displacement field caused by the presence of a crack and facilitating crack tip localization. Roux et al. used a similar approach [59] to study 3D cracks using digital volume correlation (DVC) on images obtained by magnetic resonance imaging. Fagerholt et al. [60] employ a similar FEM-based method along with a node-splitting technique along the crack path, so that the original mesh opens in conjunction with the crack opening.

Carroll et al. [61] use the accumulated plastic strain values determined by 2D DIC ex situ[9], along with visual investigation under an optical microscope, to determine the crack length. The crack tips are marked in the images, but the exact method for their determination is not described.

In the works of Mündecke and Mechtcherine [62] and Ruocci et al. [63], cement-based materials reinforced by steel bars are investigated. The crack tip is determined based on the strain field obtained from 2D DIC in the direction perpendicular to the expected crack growth path using a strain threshold value. Specifically, the location is marked as the crack when its strain exceeds a certain value, which is set with respect to elastic strains and noise to prevent false detections. Gehri et al. [64] incorporate a similar strain thresholding approach but consider any direction of crack growth.

Dong et al. [65] apply a series of parallel lines in 2D DIC, calculating their length changes to obtain COD values. The crack tip is identified where the COD value reaches zero. The experiment uses an

[7] meaning the first, second, and third terms, where the first term relates to rigid-body translations, the second to the stress-intensity factor (SIF), and the third to T-stress.
[8] denotes extended finite element method. It allows crack growth to be modeled without remeshing by incorporating discontinuous fields and near-tip asymptotic fields [154].
[9] with the specimen removed from the testing machine.

SENB specimen, composed of concrete on one half and rock on the other half, with a notch in the middle at the material interface. Alam et al. [66] and Omondi et al. [67] conduct a study using an equivalent method to determine the crack tip and crack length.

López-Crespo et al. [68] apply the Sobel-Feldman operator[10] to the 2D DIC displacement field in the direction perpendicular to the crack path. This leads to the calculation of the gradient field, which is used as an edge-point detector. The detected edge is declared a crack, and the location of its tip depends on the gradient threshold value. Edge detection on the 2D DIC displacement field is also utilized by Vanlanduit et al. [69].

Rezaie et al. [70] employ two approaches. In the first, they identify the crack using the 2D DIC Strain threshold method described above. In the second approach, unrelated to DIC, they identify cracks through VIM, which then serves as training material for deep learning.

Vasco-Olmo et al. [71] base their approach on full-field displacement evaluation using 2D DIC on a CT specimen. Let y_{VO} denote the direction perpendicular to the crack faces (vertical), with v_{VO} as the displacement in this direction; let x_{VO} denote the direction along the crack path (horizontal). Around the assumed location of the crack tip, the values of v_{VO}, calculated along a series of vertical lines, are plotted into a single graph. From their intersection, the coordinate of the crack tip $y_{VO,t}$ and the displacement value $v_{VO,t}$ are determined. Then, along the horizontal line at the location $y_{VO,t}$, the values of v_{VO} are plotted. The x_{VO}-coordinate that corresponds to the value $v_{VO,t}$ is declared the horizontal location of the crack tip $x_{VO,t}$. Thus, the location of the crack tip and the crack length are evaluated.

Durif et al. [72] utilize full-field 2D DIC measurements in their work. From these measurements, a simplified displacement field is calculated using a discontinuous shape function found in X-FEM, which has a value of ±1 on opposite sides of the crack. The COD profile is then calculated along the discontinuity, and the crack tip is estimated by linear interpolation of this profile.

O'Connor et al. [73] apply 2D DIC to images taken with a scanning electron microscope to study displacement fields around the crack tip. However, they do not use DIC itself to locate the crack tip, as it can often be very precisely located optically due to the high magnification of the images. This method, though, is not very practical for standard laboratory measurements, as it requires a complicated experimental setup and takes a long time to produce an image (approximately 10 seconds).

In many works, such as [51], [74], [75], [76], 2D DIC is used to study crack closure via virtual extensometers (VEs) that measure COD behind the crack tip. These measurements are either calculated in post-processing from full-field data or obtained directly by tracking selected points.

2.3 Evaluation of the Literature

The review has shown that some studies employ advanced techniques such as 3D DIC [77] or DVC [59], which require significant investments in hardware and software when using commercial solutions. Additionally, the latter method is quite impractical for real-time measurements. However, most of the referenced works utilize only 2D DIC, which seems adequate for fatigue testing involving planar surfaces and minimal out-of-plane[11] deformation.

[10] is an isotropic 3×3 gradient operator [155]
[11] meaning the direction parallel to the camera's optical axis.

Selecting the appropriate density for the DIC mesh on which displacements or strains are calculated is essential when utilizing 2D full-field measurements. This requires balancing accuracy and computational complexity, which can lead to significant solution times, especially when additional operations like fitting the Williams series are involved. A widespread practice to achieve reasonable accuracy, temporal, and spatial resolution in DIC full-field evaluations is to perform calculations in post-processing on the recorded images.

However, a major advantage of this method is its ability to capture crack propagation in any direction and to extract additional parameters such as crack tip opening displacement (CTOD) [71], SIF [54], or to investigate related phenomena like crack closure [76] or the plastic zone [78]. In summary, employing 2D DIC full-field measurements proves to be a flexible and comprehensive approach for fatigue testing analysis, with notable relevance in other areas of fracture mechanics as well, although it is not well suited for real-time applications.

The standard for testing FCGR mandates that the crack must propagate in a straight line, and any significant deviation from this path renders the test invalid [19]. Therefore, it is possible to simplify the 2D full-field measurement into the so-called 1D approach or 1D DIC, which the author termed in [79]. This technique focuses exclusively on extracting deformations along the anticipated crack path, thereby reducing the number of points where DIC calculations are performed. Consequently, computational time is reduced, enhancing usability for real-time applications. Real-time system response is essential for enabling the potential automation and control of cyclic tests using DIC.

The 1D DIC approach for extracting the COD curve has been used in noticeably fewer articles. Although this technique significantly reduces computational demands, the "crack tip cannot be easily located from the opening profile COD_{DIC} (…) as the crack tip blunting and the large plasticity induce large COD_{DIC} values" [80]. It is often stated that the crack tip location corresponds to the coordinate where the COD reaches zero or a certain threshold value. The zero approach, in contrast to the threshold technique, "gives an effective length of the crack which includes not only the macrocrack length but also the length of the microcracking zone" [66]. Additionally, measurements conducted in this thesis indicate that the transition of the COD to zero is gradual and noisy, making it challenging to determine the exact zero-value point.

In general, most approaches in either 2D DIC full-field or 1D DIC use a threshold value to determine the presence of a crack and its tip, whether based on displacement, strain, or grayscale gradient. When deformation is used as the threshold quantity, the author refers to this as the deformation threshold method (DTM) [79], which is schematically illustrated in Fig. 1. The 1D DIC utilizing the DTM can also be found in commercial DIC systems, such as those by Imetrum [81] or X-Sight [82].

This phenomenological method is quite easy to implement, which supports its wide usage. However, the primary difficulty in its practical application in material testing is determining the threshold value, which can vary depending on factors such as material properties, sample size, sample type, and the level of applied load. This variability may necessitate the development of a threshold value database customized for specific use cases. The load level (LL) dependence is particularly problematic, as the load is not only changed between tests but also within a single test to evaluate FCGR at different SIFs and to identify SIF threshold value when the crack does not grow. The author considers this limitation significant, motivating the proposal of an innovative approach that better reflects the nature of the measured phenomenon.

2.4 Inflection Point Principle

The discussed phenomenon is clarified by the works of Barenblatt [83] and Dugdale [84], who pioneered the concept of molecular cohesive forces ahead of the crack tip. In their model, opposing crack faces attract strongly at small separations, and this attraction weakens as separation increases, leading to the cusp-like shape formed by the gradually approaching crack faces. This contrasts with the "unnaturally rounded" [83] shape considered in earlier approaches. The area where cohesive forces are predominant is known as the fracture process zone[12] (FPZ), while the region behind the crack tip is considered stress-free. When the crack shape is represented (e.g., via COD), the transition between these two regions is marked by an inflection point (IP), as illustrated in Fig. 1. According to sources that account for cohesive forces, such as [85], the crack tip is situated at the boundary of these two regions and is used to determine the crack length.

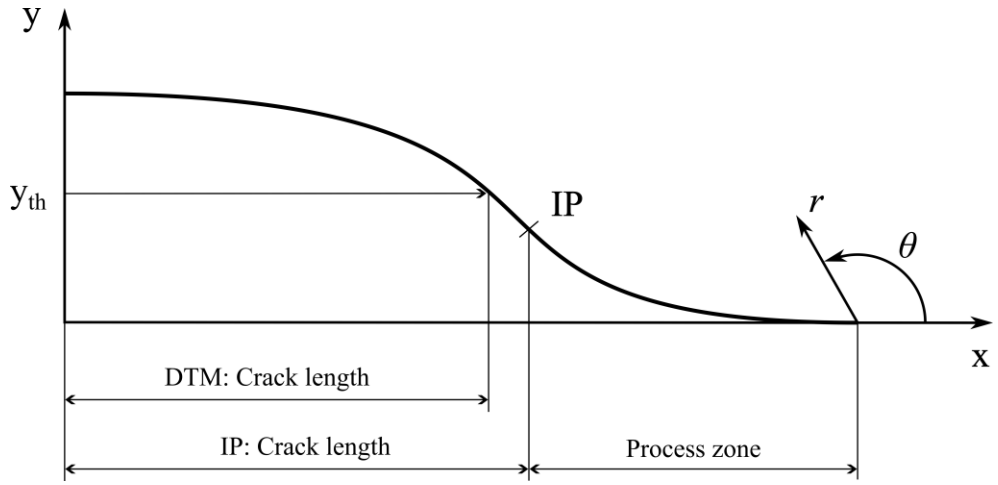

Fig. 1: The configuration of the open crack, where the x-axis denotes the distance from the notch tip, and the y-axis indicates the displacement (e.g. COD), highlighting the inflection point. The crack's shape is symmetric relative to the x-axis, with only one side depicted. On the right, the radial coordinate system (r, θ) used for deformation calculations [89] is presented, while the concept of the deformation threshold method is shown on the left, with y_{th} signifying the threshold value [79]

Recently, numerous studies on the FPZ have used nonlocal elasticity[13], specifically gradient elasticity theory [86]. For instance, Sciarra and Vidoli [87] demonstrated for isotropic materials that "strain gradient elasticity can provide the same asymptotic COD of Barenblatt cohesive model". This asymptotic behavior scales as $r^{\frac{3}{2}}$, where r is a coordinate on the crack path axis, with zero at the crack tip and the positive semiaxis pointing toward the crack mouth.

Skalka et al. [88] compare a discrete finite element model of a ceramic foam-like structure with a homogenized model that uses strain gradient elasticity theory to calculate the COD profile, showing good agreement. They also state that the IP marks the location where the cusp-like closure zone with cohesive-like behavior, scaling asymptotically as $(r^{\frac{3}{2}}, \theta = \pi\, rad)$, transitions to the far-field COD shape $(r^{\frac{1}{2}}, \theta = \pi\, rad)$, as predicted by classical elasticity solutions. Here, r and θ denote polar

[12] is a region with a disordered internal structure and nonlinear material behavior that evolves at the tip of a propagating crack [156], where microcracking occurs and the macrocrack is formed.
[13] assumes that the nonlocal stress at a reference point depends not only on the strain at that location, but also on the strains at all other locations within a given domain[157].

coordinates with origin at the crack tip (see, e.g., [89]. The coordinate system is also illustrated in Fig. 1. Kotoul et al. [90] present a comparison between results obtained from an atomistic approach using ab-initio density functional theory calculations and those from strain gradient elasticity theory, showing a good match for both isotropic and anisotropic solids. In their work, the CTOD is evaluated at the IP, suggesting its association with the crack tip.

In terms of applying this principle to practical fatigue crack length determination using DIC, only one study [91] has been found that identifies the IP on the COD curve. The study, which focuses on the fatigue testing of polymers, suggests a correlation between the crack tip location and the position of the IP in the DIC-measured data on the CT sample. However, its reliability appears limited due to the methodology used. It is based on a comparison of the crack length measured by VIM using a traveling microscope positioned on the side opposite to the camera for DIC measurement. The results from both sides may differ due to uneven crack growth through the sample thickness. This issue is acknowledged in the paper, which recommends making comparisons on the same specimen side. Additionally, the paper does not provide details about the DIC algorithm settings, or the methods used to extract the IP.

2.5 Problem Statement and Objectives

Considering the outcomes of the literature review and the inflection point principle, which together summarize the current state of knowledge and research gaps in DIC crack length measurement, the following **problem** is formulated:

Development of a DIC-based methodology for real-time fatigue crack length measurement of metals.

The methodology will incorporate a novel method for crack length assessment from 1D DIC data, which is physics-based, unlike the currently used DTM, and does not require a threshold value. This will enhance the versatility and applicability of DIC in the crack length measurement of metallic materials. It can replace the VIM widely used in fatigue testing, enabling measurement and quick assessment of results without stopping the cycling. This will make testing more efficient and create opportunities for future automation and control of the tests.

To successfully address the identified research gaps, the following **objectives** must be fulfilled:

- *Creation of a methodology for determining fatigue crack length using digital image correlation (DIC).*
- *Validation of the created methodology using a currently utilized non-DIC approach for determining fatigue crack length. The validation will include various metallic materials, sample sizes, and load levels.*
- *Comparison of the created methodology with another currently used DIC-based approach.*
- *Investigation of the methodology's response to changes in input parameters.*

3 Theoretical Background

In this chapter, a brief theoretical background is provided for areas related to the problem solution. Additionally, it covers the essential concepts needed to understand and use the proposed methodology, which users should be aware of.

3.1 Digital Image Correlation

DIC was introduced in Chapter 1, including its applications; this section briefly summarizes and clarifies aspects not explicitly explained there.

As mentioned, DIC is an optical method for assessing surface deformation by comparing the image of a deformed entity with the image of an undeformed entity, which serves as a reference. When in-plane deformations are measured on the planar surface of a body using one camera, this is referred to as 2D DIC. Note that 1D DIC refers to the fact that the measured phenomena occur in one direction, and the data processing and evaluation are appropriately adapted for computational efficiency. To measure out-of-plane deformations on an arbitrarily shaped surface of a body, two or more cameras must be used, and this is called 3D DIC.

For completeness, another related method that operates on similar principles, though it is not the focus of this treatise, is DVC [92]. It is used to measure subsurface deformations by tracking inherent features within the material, for example, using X-ray tomography.

All subsections of this section (3.1) relate to 2D DIC unless otherwise stated, as it is the primary focus of this thesis.

3.1.1 Equipment

3.1.1.1 Camera

The basic component in the DIC setup is a monochrome CCD (Charge-Coupled Device) or CMOS (Complementary Metal-Oxide Semiconductor) digital machine vision camera (Fig. 2). The camera should have the following characteristics [93]:

- The lowest possible noise: Noise is caused by the presence of dark current and is expressed by the signal-to-noise ratio (SNR). Low noise is important for the accuracy of measurements.
- The highest possible dynamic range: This is the range of light intensities that can be captured by the sensor. A high dynamic range is important for capturing more details in both the bright and dark areas of the image.
- The highest possible quantum efficiency: This is the ability of the chip to use the maximum amount of present light in terms of converting it into information (electrical signal). High quantum efficiency leads to better image quality, especially in low-light conditions.

Low-light conditions do not necessarily mean an improperly lit scene; they can also refer to situations involving fast events that require shorter exposure times (higher shutter speeds) to prevent image blurring, thereby reducing the amount of light reaching the sensor. Machine vision cameras also offer gain adjustment, but it is usually avoided because increasing the gain amplifies the present noise. Instead, proper lighting is preferred to enhance contrast in the image.

Fig. 2: CMOS digital camera for machine vision [153]

Other important parameters of a digital camera that users should consider, as found in the datasheet, include:

- Number of pixels (n_{px}): Typically given in megapixels. It is related to imaging system resolution, which will be discussed in more detail in subsection 3.1.2.
- Maximum standard frame rate: Expressed as frames per second (FPS). It should be considered in relation to the rate of measured deformation.
- Sensor size: Used to select compatible lenses and to determine the field of view (FoV).
- Pixel size (s_{px}): Essential for calculating the camera resolution, which will be further discussed in subsection 3.1.2.
- Sensor shutter type: Refers to the method used for reading the collected data in pixels. There are two basic types: global shutter, where all pixels are read out simultaneously, and rolling shutter, where data is read sequentially by rapidly "scanning" the chip during exposure. Rolling shutter cameras are cheaper but are not suitable for recording moving objects, as they create the so-called rolling shutter effect (Fig. 3). Therefore, global shutter cameras are more frequently used in DIC deformation measurement.

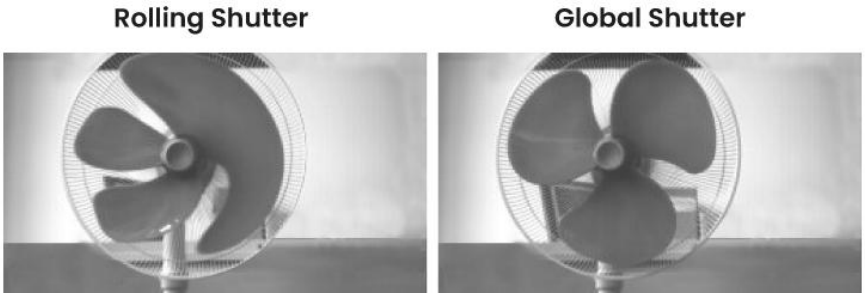

Fig. 3: Rolling shutter effect on a moving object [159]

3.1.1.2 Lenses

An equally important piece of equipment is the lens. The standard lenses used are called entocentric lenses (Fig. 4 (left)). Among their important parameters for the user to consider, which are usually stated in the data sheets, are:

- Focal length (f): Affects magnification m_{opt}, depth of field (DoF), and FoV. In machine vision, wide-angle lenses with low f are often used (Fig. 4 left). It can be either fixed (providing better optical properties) or variable (the so-called zoom lenses).
- F-number ($f/\#$): Determines the lens speed, indicating the light-gathering ability of the lens. It depends on the size of the aperture, which can be adjusted by the iris (except in cases with a fixed iris). A more open iris increases the amount of light transmitted to the camera, improving

image quality (discussed in a separate subsection), but it also reduces the DoF and results in a lower $\not f/\#$, and vice versa [94].

- Operational range of focus: Determines the possible working distances (WDs) of the optical system. It usually includes the minimum object distance parameter at the lower bound of the focus range.
- Maximum sensor size: Ensures compatibility with the selected camera or aids in camera selection.
- Distortion: Discussed in subsection 3.1.3.

Fig. 4: Wide-angle entocentric lens (left) [160], and telecentric lens (right) [161] for machine vision

Although entocentric lenses are widely used and suitable for a wide range of applications, certain recommendations must be adhered to when used for 2D DIC measurement. For example, the optical axis of the system should be perpendicular to the measured planar surface, and deformations should occur only in this plane [93]. Failure to meet these conditions results in inaccuracies in the measurement due to parallax (perspective) error. This situation is illustrated in Fig. 5. The rays coming from the object converge to a single point, forming a conical FoV. Thus, when using a single camera, halving the distance of the object from the lens and doubling its dimensions in its original plane cannot be distinguished from each other [95].

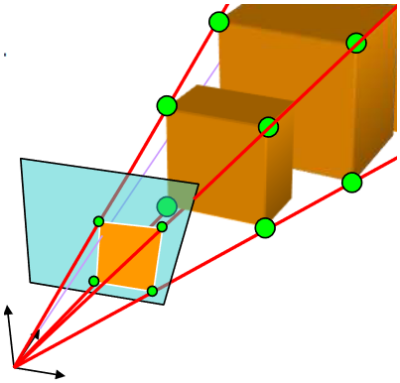

Fig. 5: Illustration of the parallax (perspective) error [95]

A way to minimize parallax error and achieve repeatable high-accuracy measurements is by using a telecentric lens (TL) [93] (usually object-space telecentric, unless explicitly defined as bi-telecentric[14]), as depicted in Fig. 4 (right). In contrast to entocentric lenses, which have an angular FoV, a TL has a constant, non-angular FoV [96], as shown in the scheme in Fig. 6. This is achieved by working only with parallel rays entering the optical system [97].

TLs have a fixed $\not f$, DoF, m_{opt}, $\not f/\#$, and WD. The FoV can vary only based on the sensor size of the

[14] or double telecentric lenses are telecentric in both object space and image space. This configuration enables the most accurate measurements [96], but incurs higher cost. In this case, the rays are parallel to the optical axis when both entering and leaving the lens.

paired camera, with the maximum compatible sensor size usually specified. TLs also feature minimal lens distortion [98] reducing the need for additional distortion corrections. Therefore, only the calibration of the 2D DIC with known dimensions is necessary (see subsection 3.1.4). Additionally, telecentricity is quantified, for example, as the maximum angle between the chief ray[15] and the optical axis.

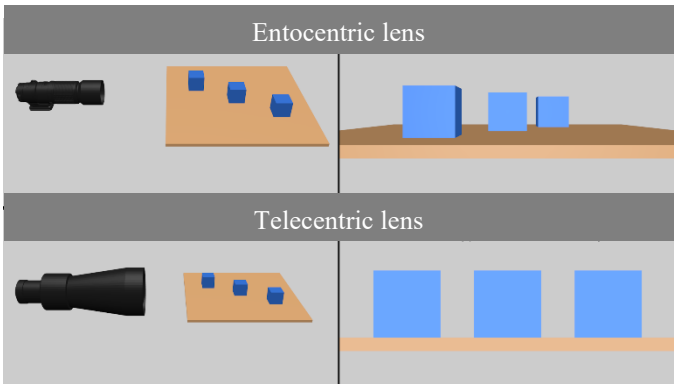

Fig. 6: Demonstration of entocentric vs. telecentric imaging results [99]

The design of a TL causes the FoV to be related to the front optic diameter. Smaller TLs (in diameter) usually have higher m_{opt} and a higher $f/\#$, which results in a lower lens speed. When a larger FoV is needed, it requires using a lens with a larger front diameter [99], which results in lower m_{opt}. Additionally, TLs with higher lens speed (smaller $f/\#$) tend to be noticeably larger in size [100], which increases the purchase price.

3.1.1.3 Illumination

The last essential piece of equipment is lighting. It is important that the lights produce as little heat as possible to avoid affecting the measurement, such as causing thermal expansion of the camera and lenses or increasing sensor noise. Therefore, halogen lamps are not suitable. LED (light-emitting diode) lamps are most often used for DIC. In situations where the shutter speed is high and/or lens speed is low, and a light source that generates significant heat must be used, it is recommended to use flashes of light instead of continuous lighting.

The resulting illumination should be evenly distributed over the measured area and should not be too intense to avoid pixel saturation during measurement, which would complicate the numerical processing of the acquired image. Additionally, the lighting should remain consistent throughout the measurement.

3.1.2 Resolution and Contrast

Resolution is important in terms of using the optical system for measurements. It quantifies the system's ability to reproduce an object's detail in the resulting image. Its basic principle is illustrated in Fig. 7, where two squares (points/lines) can be distinguished in the image only when they are distant enough from each other. This minimum distance is determined s_{px}. Thus, the resolution is effectively given by two pixels or one line pair (lp). It relates to the Nyquist frequency and is often given as the frequency in the unit of *lp per mm*. The maximum number of resolvable line pairs then represents the resolution of

[15] is the ray from an off-axis object point that passes through the aperture stop [158] (lens focal point). For a telecentric lens, chief rays are theoretically parallel to the optical axis.

the sensor (also referred to as the Nyquist limit) [101]:

$$\xi_{sensor} = \xi_{image} = \frac{1}{2s_{px}} \left[\frac{lp}{mm}\right] \quad (1)$$

where s_{px} is used in millimeters.

Practically, users are more interested in the smallest resolvable spot on the object in a length unit rather than in frequency. To determine this, the system magnification must first be calculated [101]:

$$m_{opt} = \frac{h_{sensor}(s_{px}, n_{px})}{h_{FoV}(WD, \not{f}, \not{f}/\#)} \; [-] \quad (2)$$

where h_{sensor} is height of sensor and h_{FoV} is corresponding height of FoV. Then, the resulting object resolution is calculated as follows [101]:

$$\xi_{object} = \frac{s_{px}}{m_{opt}} [mm] \quad (3)$$

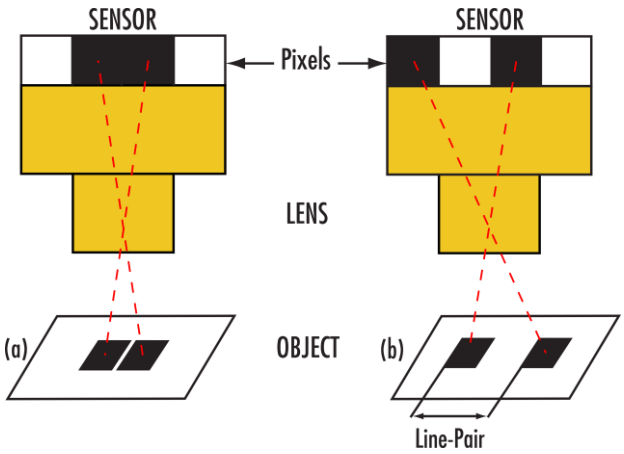

Fig. 7: Scheme of two squares imaging (a) distance between squares is too small, (b) minimum distance to resolve them [101].

Object resolution is directly affected by n_{px}, as the size of the sensor is determined by both n_{px} and s_{px}. It is important to note that doubling n_{px} does not result in twice the resolution, as the increase in the n_{px} affects both dimensions of the sensor area.

So far, an ideal transfer of the object into the image has been assumed. In reality, this is not the case, as this transfer is affected by the diffraction of light in the imaging system, which occurs, for instance, at the edges of lenses or the iris. Each object point is then projected into the image as a blurred spot called an Airy disk [102], illustrated in Fig. 8. It appears as a central maximum of light intensity I_{opt} surrounded by dark and bright rings of decreasing I_{opt}. Two such points on the object can be resolved through the imaging system when their image centers are separated by at least the minimal gap, which equals the distance from the center of the Airy disk to its first minimum, as stated by the Rayleigh limit in air [102][16]:

[16] The equation is adjusted by substituting the effective f-number for the numerical aperture.

$$d_{Rayleigh,img} = 1.22\lambda(f/\#)(1 + m_{opt}) \tag{4}$$

where $d_{Rayleigh,img}$ is expressed in the same length units as the wavelength λ. This value represents the theoretical diffraction resolution limit. In the object (measured) plane, the corresponding minimum separation is:

$$d_{Rayleigh,obj} = \frac{d_{Raileigh,img}}{m_{opt}} \tag{5}$$

Then, if the optics can resolve the points, the sensor must have small enough pixels to image them correctly; by the Nyquist criterion this requires $s_{px,max} = d_{Rayleigh,img}/2$.

$$s_{px,max} \leq \frac{1}{2} d_{Rayleigh,img} \tag{6}$$

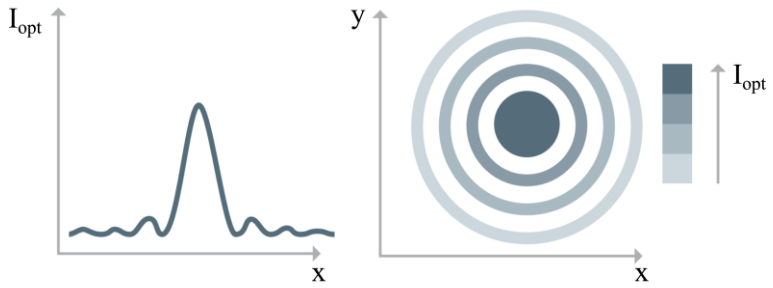

Fig. 8: Due to the diffraction of light, every object point is imaged as a blurred spot, creating an Airy disk. The graphs show the Airy disk as a spot surrounded by rings of decreasing light intensities (right) and the intensity distribution in a cross-section through the middle of the disk (left) [102].

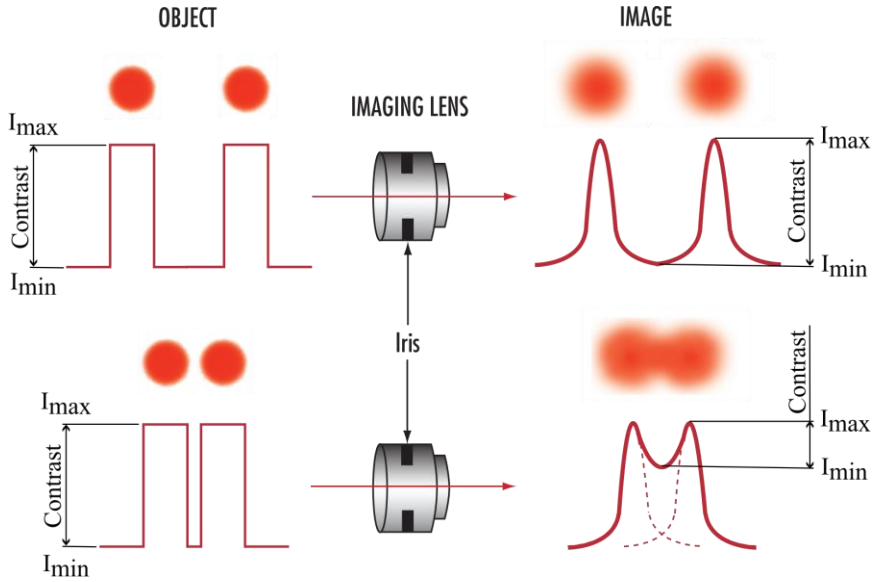

Fig. 9: Difference in contrast using the same lens for the imaging the same two points, that are positioned with low spatial frequency (top) and high spatial frequency (bottom) [103]. $Contrast = \mathbb{C}$

If the pixels are larger, the points, although resolved by optics, get merged in the image; conversely, if we have small enough pixels, but the points are closer together than the Rayleigh limit, they get blurred.

In that case, smaller pixels would not provide greater detail in the image; they would only show a blurred spot distributed over more pixels. This is important to consider when selecting the imaging system, as equipment with greater resolution and smaller pixels is more costly. Therefore, for example, it is enough to have a pixel size of $s_{px,max}$.

Another important concept related to the preceding discussion is contrast. It indicates how well black and white can be distinguished from each other at a given resolution [103]. The different contrast between two points is caused by the constructive interference of the Airy disks projected onto the sensor when they are situated close to each other, as illustrated in Fig. 9. It can be quantified as [103]:

$$\mathbb{C} = 100\left(\frac{I_{opt,max} - I_{opt,min}}{I_{opt,max} + I_{opt,min}}\right)\ [\%] \tag{7}$$

It is evident that resolution and contrast are closely related, and it is meaningless to specify one without the other. The higher resolution of the imaging system can be achieved at lower contrast and vice versa. Thus, when resolution is specified in datasheets, it might state, for instance $70\ lp/mm$ @ 50 %. This relationship can also be described by the entire contrast-to-spatial-frequency (resolution) dependence, which is called the modulation transfer function [104].

3.1.3 Lens Distortion

Lens distortion is an optical aberration that does not preserve the geometric fidelity of the object in the image. The distortions can be divided into radial and tangential. For many applications, it is not necessary to consider tangential distortion, as it is negligible compared to radial [105]. Radial distortion causes either negative point displacement (inward) called *barrel distortion* or positive radial displacement (outward) called *pincushion distortion* [106], as illustrated in Fig. 10. Their potential combination forms a more complex distortion called "moustache distortion" [107]. The figure also shows characteristic distances: predicted distance PD (which would be without distortion) and the actual distance AD (which is with distortion), which are then used to quantify the lens distortion [108]:

$$D_{opt} = 100\left(\frac{AD - PD}{PD}\right)\ [\%] \tag{8}$$

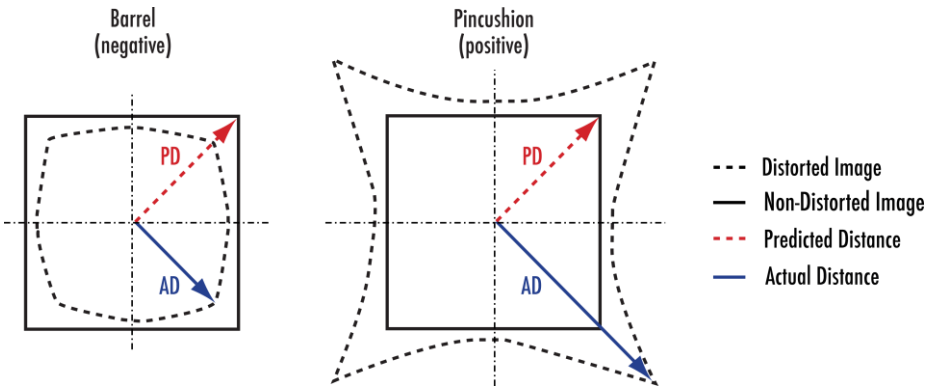

Fig. 10: Effects of radial distortion: barrel (left) and pincushion (right) [108]

depends on the radial distance (y) from the image center and λ. Thus, if specified in the datasheet, it

should be accompanied by these two values, for instance 2 % ($y = 4.5, \lambda = 520$)[17].

The second, older approach to specifying lens distortion, which can still be found when selecting machine vision lenses, is TV distortion. This is obtained by evaluating the height distortion at the image's top edge of the FoV. In the case of barrel distortion, this is measured when the center of the distorted rectangular object is at the edge of the FoV. For pincushion distortion, it is measured when the corners of the distorted object are at the edge of the FoV. This is illustrated in Fig. 11 along with the quantities that enter the following equation to quantify TV distortion[18] [109]:

$$D_{TV} = 100\frac{DH}{H}\ [\%] \tag{9}$$

The sign convention is the same as for D_{opt}, positive value means pincushion and negative value barrel distortion. Since the distortion dependence is not always monotonic, it is better to graph the entire $D_{opt}(y)$ instead of using a single D_{opt} or, even worse, a single D_{TV} value. This graph usually contains three curves: for red, green, and blue light. It is typically obtained from imaging a grid with regularly spaced points [108].

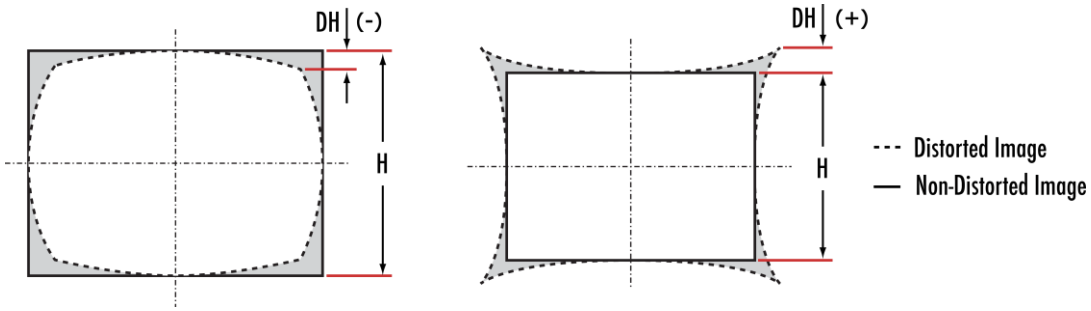

Fig. 11: TV distortion for both barrel (left) and pincushion (right) distortion type [108]

3.1.4 2D DIC Calibration

A 2D DIC calibration performed before measurement assigns physical scale to pixels by establishing the mapping between a length unit (e.g., millimeters) and image pixels. This can be done either by referencing a known dimension in the scene or—preferably—by imaging a calibration grid with precisely spaced points. Using a grid also enables lens-distortion correction and automatic definition of the coordinate system: the grid should include three fiducial points larger than the others to mark the origin and the x- and y-axis directions, and these fiducials must be non-equally spaced to unambiguously distinguish the axes.

[17] To maintain consistency with the datasheet, the radial distance is denoted by y in this subsection (3.1.3) only.
[18] where TV stands for television

3.1.5 2D DIC Principles

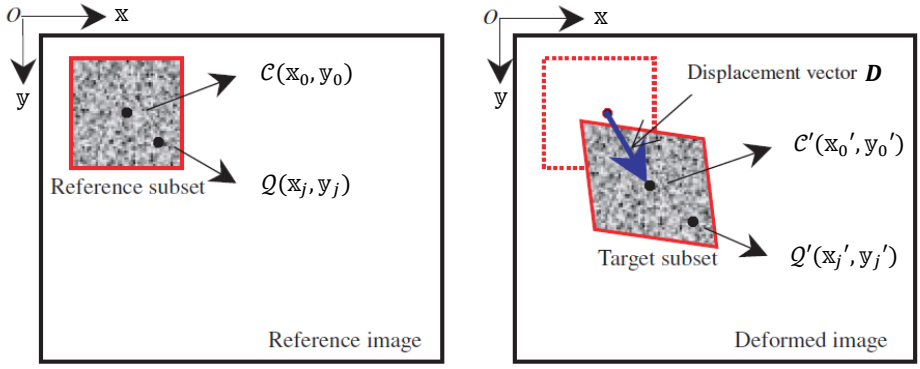

Fig. 12: Principle of 2D DIC [110].

The explanation of the basic principle of 2D DIC, presented in the following text, builds on the illustration in Fig. 12. The first (reference) image is usually taken of the surface of the undeformed body and serves as a baseline for displacement calculations in subsequent images, which are acquired during or after deformation (deformed images). In the reference image, an area of dimensions $(w_{sub}, h_{sub})\ px$ is selected, where w_{sub} represents its width and h_{sub} its height. This area, called the subset (facet or template), serves as a unique signature of the point $C(\mathrm{x}_0, \mathrm{y}_0)$, which is at the center of the subset [110]. From the center of the most similar subset in the deformed image $C'(\mathrm{x}_0', \mathrm{y}_0')$, the displacement vector is then calculated [110]:

$$\boldsymbol{D}(\mathrm{u}, \mathrm{v}) = C'(\mathrm{x}_0', \mathrm{y}_0') - C(\mathrm{x}_0, \mathrm{y}_0) \tag{10}$$

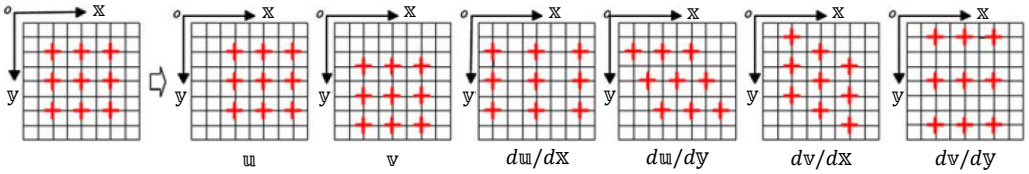

Fig. 13: Six different linear transformations used in the first-order shape function [22].

In the selection of the most similar subset, its linear transformations using shape functions are applied. Using the zero-order shape function, only the displacement vector would be obtained. However, it is assumed that the size and shape of the subset change due to deformation. Thus, at least a first-order shape function is usually implemented. In the case of the first-order shape function, each searched subset in the deformed image contains a vector of unknown parameters (illustrated in Fig. 13) denoted as $\boldsymbol{\hbar}$, which are optimized in search of the new subset position [22]:

$$\boldsymbol{\hbar} = \left(\mathrm{u}, \mathrm{v}, \frac{\partial \mathrm{u}}{\partial \mathrm{x}}, \frac{\partial \mathrm{u}}{\partial \mathrm{y}}, \frac{\partial \mathrm{v}}{\partial \mathrm{x}}, \frac{\partial \mathrm{v}}{\partial \mathrm{y}}\right) \tag{11}$$

Then, the deformation of the subset can be described in the following manner. When an arbitrary point $Q(\mathrm{x}_j, \mathrm{y}_j)$ is selected in the undeformed subset, its position $Q'(\mathrm{x}_j', \mathrm{y}_j')$ in the deformed one can be expressed using the parameters in $\boldsymbol{\hbar}$ as follows [22]:

$$\mathbb{x}'_j = \mathbb{x}_j + \mathbb{u} + \frac{\partial \mathbb{u}}{\partial \mathbb{x}}\Delta\mathbb{x} + \frac{\partial \mathbb{u}}{\partial \mathbb{y}}\Delta\mathbb{y} \tag{12}$$

$$\mathbb{y}'_j = \mathbb{y}_j + \mathbb{v} + \frac{\partial \mathbb{v}}{\partial \mathbb{x}}\Delta\mathbb{x} + \frac{\partial \mathbb{v}}{\partial \mathbb{y}}\Delta\mathbb{y} \tag{13}$$

where $\Delta\mathbb{x} = \mathbb{x}_j - \mathbb{x}_0$ and $\Delta\mathbb{y} = \mathbb{y}_j - \mathbb{y}_0$. Higher-order shape functions might also be used for the description of more complex deformation fields [111].

The similarity of the subset between the deformed and undeformed images is assessed using correlation functions or criteria, which can be divided into two main groups: cross-correlation (CC) and sum of squared differences (SSD). These can be formulated as follows [110]:

$$C_{CC}(\boldsymbol{h}) = \sum_{j=0}^{w_{sub}} \sum_{k=0}^{h_{sub}} \left[f_{GL}(\mathbb{x}_j, \mathbb{y}_k) g_{GL}(\mathbb{x}'_j, \mathbb{y}'_k) \right] \tag{14}$$

$$C_{SSD}(\boldsymbol{h}) = \sum_{j=0}^{w_{sub}} \sum_{k=0}^{h_{sub}} \left[f_{GL}(\mathbb{x}_j, \mathbb{y}_k) - g_{GL}(\mathbb{x}'_j, \mathbb{y}'_k) \right]^2 \tag{15}$$

where $f_{GL}(\mathbb{x}_j, \mathbb{y}_k)$ and $g_{GL}(\mathbb{x}'_j, \mathbb{y}'_k)$ denote the corresponding gray level values in the reference and deformed images, respectively. Equations (14) and (15) can also be modified to be independent of the linear scaling of the illumination between the reference image and the deformed image. Then it is called NCC and NSSD, where N stands for normalized. Alternatively, they can be modified to be independent of linear scaling and offset in illumination. This is called ZNCC and ZNSSD, where ZN stands for zero-normalized, which is the most robust approach [110].

3.1.5.1 Subpixel Accuracy

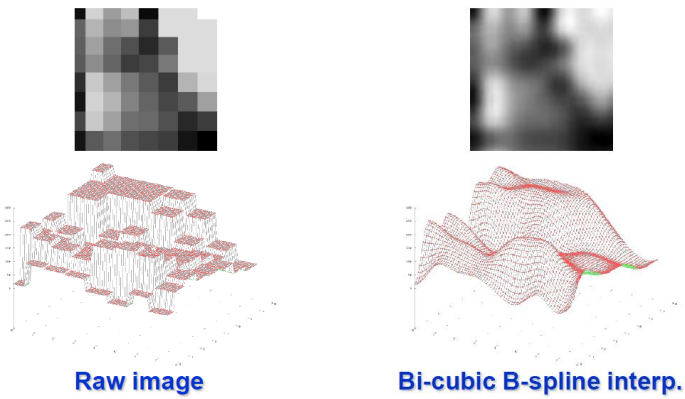

Fig. 14: Comparison of the raw image subset (left) and the interpolated subset (right) [95].

The locations of the points $C(\mathbb{x}_0, \mathbb{y}_0)$ and $C'(\mathbb{x}'_0, \mathbb{y}'_0)$ do not necessarily correspond to the center of a pixel, and assuming that would be very limiting for measurements. Therefore, an interpolation scheme is introduced before the similarity assessment to provide subpixel locations and grayscale levels. For this purpose, bi-cubic B-spline interpolation (Fig. 14) or other advanced interpolation methods, such as bilinear or cubic convolution interpolation, are commonly utilized [95]. As a result, the 2D DIC can

measure “displacements with accuracy on the order of ±0.01 pixels” [24].

3.1.5.2 Subset Size Selection

Selecting the subset size for DIC is crucial for measurement accuracy. This process involves balancing several conflicting factors, resulting in an application-specific trade-off between the influence of random errors (small subset) and systematic errors (large subset) [112]. Random errors are caused by image noise, which is more effectively smoothed by subpixel interpolation with larger subsets. However, larger subsets may incorrectly approximate underlying deformation due to the applied shape functions [112].

A larger subset is also needed to capture enough distinctive pattern features to be clearly distinguishable from other subsets [113]. Conversely, a smaller subset can better approximate deformation with first- or second-order shape functions [113], particularly in heterogeneous deformation fields with high gradients. Thus, smaller subsets enhance the spatial resolution of measured displacements [93]. Additionally, larger subsets increase processing time and memory usage.

3.1.6 Specimen Preparation and Speckle Pattern

For accurate measurement, the sample should have an isotropic, non-repeating, high-contrast pattern on its surface, known as a speckle pattern (Fig. 15) [95]. This pattern enables each subset to serve as the unique signature of the tracked point. The recommended density of the speckles covering the surface is approximately 50%, and their size should be at least three-by-three pixels to avoid aliasing but not higher than seven-by-seven pixels to achieve the recommended density [114]. Thus, the actual speckle size in mm depends on the character of the measured deformation, FoV, and number n_{px}, as exemplified in the following equation [93]:

$$12\ mm\ /\ 2048\ px\ *\ (3\ to\ 7\ px\ per\ speckle)\ =\ 18\ to\ 41\ \mu m\ per\ speckle \tag{16}$$

Spraying black paint on a white background is a common way to create the pattern; it suppresses glare from often glossy substrates and provides the recommended high contrast [24]. However, when using this technique, controlling speckle size can be challenging. Ideally, the gray-scale levels histogram should resemble a bimodal Gaussian distribution (GD). The speckles should be as uniform in size as possible, and the entire pattern should deform with the sample and remain stable during testing, as some patterns may decay or darken under heating [93].

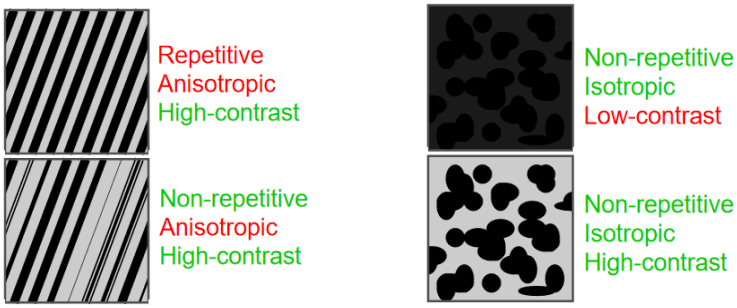

Fig. 15: Example of speckle patterns with appropriate (green) and inappropriate (red) aspects [95]

Artificially created patterns tend to separate from the sample surface, particularly when the underlying surface is smooth. In the best-case scenario, the separated paint falls off the pattern and only worsens the correlation. In the worst-case scenario, the paint layer deforms differently from the sample surface beneath it. This leads to measured deformations that do not correspond to reality, and it is often difficult

to detect this discrepancy.

The natural surface of the sample can also be used for correlation, but it must be noted that the more the surface texture deviates from the requirements, the more it will affect the accuracy of the results. In some types of material testing, such as tensile tests, measurements are conducted directly on natural surfaces or on surfaces marked with drawn crosses or stickers, which provide sufficient accuracy.

3.1.8 Error Sources in 2D DIC

Some of the effects were already discussed in more detail in subsections 3.1.2 – 3.1.6, therefore the following serves as a summary and completion. According to Zhao et al. [22], the main sources of errors for 2D DIC can be divided into those caused by the DIC algorithm and those caused by the image acquisition process.

Errors caused by the DIC algorithm include [22]:

- **Subset size**, whose appropriate selection is discussed in subsection 3.1.5.2.
- **Shape function order,** which should be selected regarding the character of the measured deformation to minimize systematic errors.
- **Correlation criterion** and **interpolation scheme**, which should be appropriately chosen regarding accuracy and computational time. Although computational time is an important parameter, with the affordability of significant computational power today, the emphasis is mostly on accuracy.

Errors caused by the image acquisition process include [22]:

- **Speckle pattern quality,** which was elaborated on in subsection 3.1.6.
- **Influence of the experimental environment,** which causes various kinds of noise, such as noise due to illumination fluctuations or readout noise. Their influence can be reduced by time averaging, spatial low-pass filtering, or using higher-quality hardware. Additionally, ambient vibrations can introduce significant errors in the measurement, especially with a compliant camera fixture.
- **Effect of out-of-plane motion of the sample surface**, which is a significant problem for entocentric lenses. Sutton et al. [115] quantified the strain error to be $1250\ \mu\varepsilon/mm$ for entocentric lenses, compared to $25\ \mu\varepsilon/mm$ for TLs, showing a significant reduction.
- **Effects caused by the camera itself**, such as:
    - **self-heating,** which is an unavoidable phenomenon with a running camera that can cause noticeable measurement error. Increasing camera temperature not only brings higher dark current and thus increases noise but also causes thermal expansion of camera components, resulting in sensor movement and expansion. Ma et al. [116] demonstrated the strain error rate to be approximately $8 - 20\ \mu\varepsilon°\mathrm{C}^{-1}$, with a maximum total strain error of up to $230\ \mu\varepsilon$, which is considerable. For precise measurements, preheating of the system under measurement conditions for about 1 to 2 hours is recommended to ensure that internal camera temperatures reach a steady state. Calibration and measurement should be performed afterward.
    - **lens distortions**, which are discussed in detail in subsection 3.1.3.

3.2 Deformation Threshold Method for DIC Crack Length Assessment

This section briefly summarizes the principle of DTM, which is widely used in DIC approaches in fracture mechanics. It can be subdivided into two categories: the first uses displacements as the threshold values, and the second uses strains. This strain-based variant is referred to as the Strain threshold method (STM) [79].

For full-field measurements, STM is used exclusively. The fatigue test evaluation example in Fig. 16 helps clarify the principle of using the STM. Directional strains perpendicular to the crack path, i.e., along the loading direction, are calculated. The area where the strain surpasses the defined threshold value (shown in deep red in Fig. 16) is considered to be the crack. The location in this area that is furthest from the notch is considered the crack tip.

This approach is highly versatile and can be used for a wide range of tests, samples, and material types. It is especially useful in cases where the crack growth does not follow a straight path and changes significantly during the test or even branches. However, it can be computationally demanding, as the complexity increases with the number of calculated points. The calculation time increases with the size of the monitored area and the mesh density.

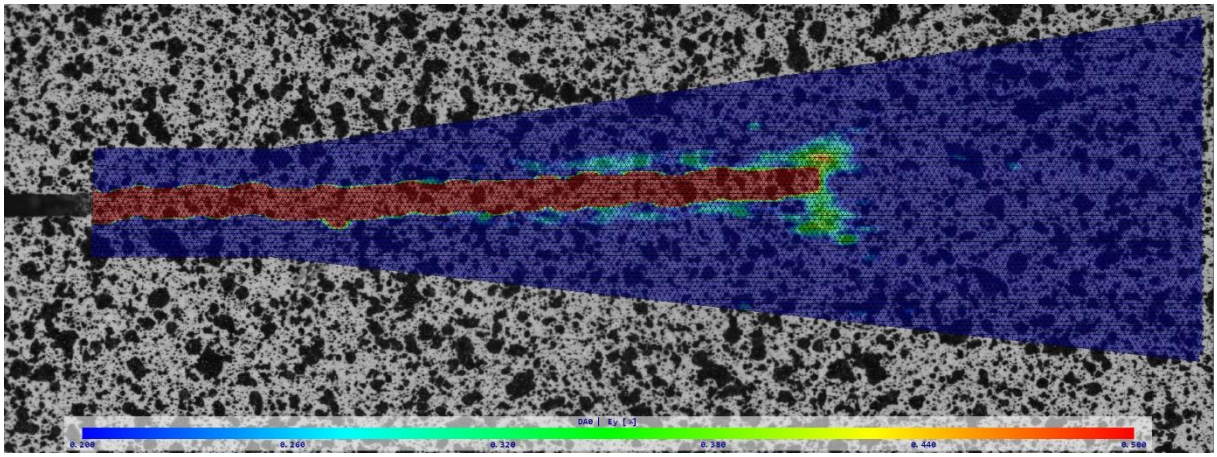

Fig. 16: An example of the DIC full-field evaluation of the fatigue test, which is suitable for the application of the STM (Strain threshold method); directional strains in the direction perpendicular to the crack path are evaluated.

The 1D approach is much more suitable for standard fatigue tests, where straight crack growth is required. In this case, data are extracted from pairs of points placed along the expected crack growth path. During loading, the change in the position of these points is evaluated, and the pairs of opposite points act as VEs, as shown in Fig. 17.

From VEs, both absolute and relative deformations can be extracted and used as inputs to the thresholding approach. Relative deformations, or STM, are more commonly used because they are less affected by the initial distance between the tracked points that form each VE.

The principle of crack tip determination is similar to the full-field case. Locations where the strain is higher than the specified threshold value are considered cracked, and the crack tip is the cracked location furthest from the notch. To ensure that the spatial resolution of the STM is not limited by the distance between the VEs, interpolation methods are commonly applied to cover the regions between the discrete data points.

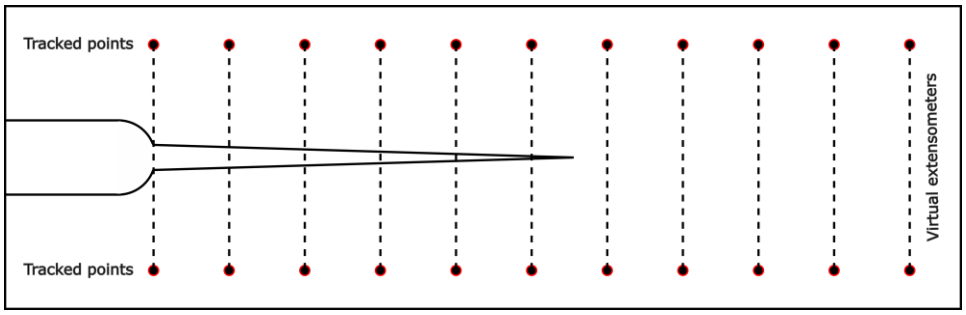

Fig. 17: Schematic illustration of VEs (virtual extensometers) placement along the crack path

3.3 Gaussian Process Regression

Gaussian process regression (GPR) is a sophisticated machine learning method that falls under the category of kernel-based, nonparametric, probabilistic approaches [117]. It models data using a Gaussian process (GP), which can be thought of as an extension of the multivariate GD to an infinite number of dimensions. Instead of specifying a probability distribution for a finite set of points as in traditional multivariate Gaussian distributions, a GP specifies a probability distribution over an infinite number of possible functions that could explain the observed data [118].

The GP is defined by two main components [117]: the mean function and the covariance (kernel) function. The mean function of a GP is derived from all the possible functions and is used for regression, while the kernel function determines the similarity between different input points [118].

The GPR implementation in the scikit-learn library [119], which is utilized in this work, adheres to the algorithm outlined in Algorithm 2.1 by Rasmussen and Williams [117].

3.3.1 GPR Example

To illustrate the GPR principle, consider a simple example, which clarifies the fundamental concept of GPR. Fig. 18 shows an example of typical GPR application. This example examines a function with a single real input s and one real output t:

$$t = s\sin s \tag{17}$$

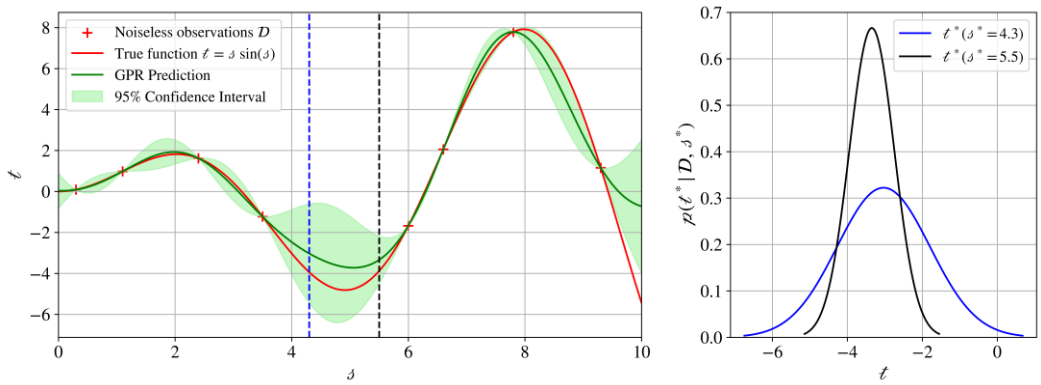

Fig. 18: Example of Gaussian process regression for noiseless observations of defined function (left) and resulting probability distributions p for predicted points (right) [79]

This function is shown in Fig. 18 (left), along with the dataset of noiseless observations $\mathcal{D}$ obtained from

this function:

$$\mathcal{D} = \left\{\left(\mathcal{S}_j, \mathcal{T}_j\right), \mathrm{j} \in \{1, \ldots, \mathrm{M}\}\right\} \tag{18}$$

where $\mathcal{S}$ represents the set of points at which the observations were made, $\mathcal{T}$ denotes the observed values, and M is the size of the dataset. These observations are then used to train the GPR model.

The proper selection of the kernel function according to the characteristics of the observed data is crucial prior to training the model, as it determines the properties of the functions generated by the Gaussian process, including their smoothness and variability.

The radial basis function (RBF) kernel is a widely used option for GPR [120] due to its adaptability, smoothness, and the infinitely differentiable functions it produces. When dealing with noisy data, as in the context of this study, it is common to include a white-noise kernel to account for independent, normally distributed noise in all observations. The combined kernel function, here denoted $\mathcal{k}$, merges the RBF kernel with the white kernel ($\mathcal{k}_w$):

$$\mathcal{k}(\varsigma, \varsigma') = \sigma_f^2 \exp\left[-\frac{1}{2\ell^2}(\varsigma - \varsigma')^2\right] + \mathcal{k}_w(\varsigma, \varsigma'),\ \mathcal{k}_w(\varsigma, \varsigma') \begin{cases} \sigma_n^2 \text{ for } \varsigma = \varsigma' \\ 0 \text{ for } \varsigma \neq \varsigma' \end{cases} \tag{19}$$

Here, ℓ is a hyperparameter called the length scale, which controls the expected similarity between nearby points and sets the maximum first derivative magnitude of the functions generated by the kernel. The hyperparameter σ_n^2, known as the noise level, indicates the variance of the noise present. The factor σ_f^2 is the hyperparameter called the kernel amplitude (signal variance).

Training consists of computing the covariance matrix defined as [118]:

$$\boldsymbol{\mathcal{K}} = \left[\, \mathcal{k}\left(\mathcal{s}_j, \mathcal{s}_k\right)\right], \mathrm{j}, \mathrm{k} \in \{1, \ldots, \mathrm{M}\} \tag{20}$$

and fitting the hyperparameters to best explain the observed data. This is achieved by optimizing the hyperparameters using the L-BFGS-B algorithm, a constrained variant of Broyden–Fletcher–Goldfarb–Shanno algorithm [121], while maximizing the log marginal likelihood [122]. The observed values in $\mathcal{T}$ are centered and scaled to obtain a zero-mean GP. In addition, the kernel amplitude is fixed so that $\sigma_f^2 = 1$ because, after this normalization, the kernel amplitude becomes largely redundant with the overall output scale and can trade off with the noise variance on noisy datasets. Fixing it removes this redundancy, reduces the number of free hyperparameters, and improves optimizer stability.

Since the GP is conceptualized as an infinite series of conditional GDs, each defined by a mean and variance that vary smoothly across $\mathcal{s}$, predictions can be made at arbitrary points (green curve), along with their 95% confidence intervals (green area).

In the regression step, the previously unseen points $\mathcal{s}_m^*$ are selected and used to calculate a new cross-covariance matrix [118]:

$$\boldsymbol{\mathcal{K}}_* = \left[\, \mathcal{k}\left(\mathcal{s}_j, \mathcal{s}_m^*\right)\right], \mathrm{j} \in \{1, \ldots, \mathrm{M}\}, \mathrm{m} \in \{1, \ldots, \mathrm{M}^*\} \tag{21}$$

where M^* is the number of previously unseen points. Then, the predictions $\boldsymbol{t}^*$ for the inputs $\mathcal{s}_m^*$, given the dataset $\mathcal{D}$, are determined (inferred) as [118]:

$$\boldsymbol{t}^{*} = \boldsymbol{\mathcal{K}}_{*}^{\mathrm{T}}\boldsymbol{\mathcal{K}}^{-1}\boldsymbol{\mathcal{T}} \tag{22}$$

where the superscript $(\cdot)^{T}$ denotes transpose, $(\cdot)^{-1}$ denotes matrix inversion, and $\boldsymbol{\mathcal{T}}$ stacks the observed values as a vector. In the same step, a GD for every new input point is obtained; Fig. 18 (right) displays two examples, highlighting the probabilistic nature of the method.

3.4 Kalman Filter

The Kalman filter (KF) is a recursive algorithm designed for optimal state estimation in linear dynamic systems subject to noise and uncertainty. Originally developed by R. E. Kalman in 1960, the filter provides an efficient computational means for estimating the internal state of a process by minimizing the mean squared estimation error [123].

The operation of the Kalman filter consists of two alternating steps: **prediction** and **correction** (also called the update step).

- In the **prediction step**, the filter uses a mathematical model of the system to forecast the next state based on the previous estimate and any known control inputs.
- In the **correction step**, this prediction is updated using the latest measurement, with the filter weighing the reliability of the model and the measurement according to their respective uncertainties.

By repeatedly cycling through these two steps, the Kalman filter continuously refines its state estimates, providing accurate and timely information even in the presence of noise. Its recursive structure requires only the most recent state estimate and measurement, making it highly efficient for real-time processing [124].

The following overview is intended to present the basic principles, parameters, and their interrelationships, rather than a complete mathematical treatment of the Kalman filter.

3.4.1 System model

The Kalman filter is applied to discrete-time controlled processes described by the following equations [125]

$$\boldsymbol{x}_{j} = \boldsymbol{\mathcal{A}}\boldsymbol{x}_{j-1} + \boldsymbol{\mathcal{G}}\boldsymbol{u}_{j-1} + \boldsymbol{\omega}_{j-1} \tag{23}$$

$$\boldsymbol{z}_{j} = \boldsymbol{\mathcal{H}}\boldsymbol{x}_{j} + \boldsymbol{\psi}_{j} \tag{24}$$

where

- $\boldsymbol{x}_{j}$: state vector for the current iteration
- $\boldsymbol{x}_{j-1}$: state vector at the previous iteration
- $\boldsymbol{z}_{j}$: measurement (observation) vector at current iteration
- $\boldsymbol{\mathcal{A}}$**:** state transition matrix (system model)
- $\boldsymbol{\mathcal{G}}$: control input matrix
- $\boldsymbol{u}_{j-1}$: control input vector applied at the previous step
- $\boldsymbol{\mathcal{H}}$: observation matrix relating the current state to the measurement

- $\boldsymbol{\omega}_{j-1}$: process noise vector
- $\boldsymbol{\psi}_j$: measurement noise vector

The process and measurement noises ($\boldsymbol{\omega}_j$ and $\boldsymbol{\psi}_j$) are assumed to be mutually independent, normally distributed random variables with zero mean and covariances $\boldsymbol{Q}$ and $\boldsymbol{\mathcal{R}}$, respectively [125]:

$$p(\boldsymbol{\omega}) \sim \mathcal{N}(0, \boldsymbol{Q}) \tag{25}$$

$$p(\boldsymbol{\psi}) \sim \mathcal{N}(0, \boldsymbol{\mathcal{R}}) \tag{26}$$

In practice, the specific realizations of these noise vectors are not directly used; instead, the process and measurement uncertainties are incorporated via the covariance matrices $\boldsymbol{Q}$ (process error/noise) and $\boldsymbol{\mathcal{R}}$ (measurement error/noise).

3.4.2 Algorithm Overview

The Kalman filter operates in two main phases at each iteration.

In the first (prediction) phase, the Kalman filter computes the *a priori* state and its associated error covariance [125]:

$$\hat{\boldsymbol{x}}_j^- = \boldsymbol{\mathcal{A}}\hat{\boldsymbol{x}}_{j-1} + \boldsymbol{\mathcal{G}}\boldsymbol{u}_{j-1} \tag{27}$$

$$\boldsymbol{\mathcal{P}}_j^- = \boldsymbol{\mathcal{A}}\boldsymbol{\mathcal{P}}_{j-1}\boldsymbol{\mathcal{A}}^T + \boldsymbol{Q} \tag{28}$$

where

- $\boldsymbol{\mathcal{P}_j^-}$: predicted (*a priori*) error covariance matrix for the current iteration
- $\boldsymbol{\mathcal{P}_j}$: updated (a posteriori) error covariance from the previous iteration; the term *a posteriori* refers to the result after the correction step (this will be discussed further below)
- $\hat{\boldsymbol{x}}_j^-$: predicted (*a priori*) state vector estimate for the current iteration
- $\hat{\boldsymbol{x}}_{j-1}$: updated (*a posteriori*) state vector estimate from the previous iteration; the term *a posteriori* refers to the result after the correction step (this will be discussed further below)

Then, in the second (correction) phase, the first step is to compute the Kalman gain matrix [125]:

$$\boldsymbol{\kappa_j} = \boldsymbol{\mathcal{P}}_j^- \boldsymbol{\mathcal{H}}^T (\boldsymbol{\mathcal{H}}\boldsymbol{\mathcal{P}}_j^- \boldsymbol{\mathcal{H}}^T + \boldsymbol{\mathcal{R}})^{-1} \tag{29}$$

This form of the resulting Kalman gain minimizes the *a posteriori* estimation error covariance $\boldsymbol{\mathcal{P}_j}$ [125] and thus represents the Kalman-optimal result [124]. The Kalman gain then acts as a weighting factor in the correction step, determining how much the filter relies on the prediction versus the new measurement:

- When the measurement error covariance $\boldsymbol{\mathcal{R}}$ is low and the *a priori* estimate error covariance $\boldsymbol{\mathcal{P}}_j^-$ (which increases with higher process error covariance $\boldsymbol{Q}$) is high, the Kalman gain is large. The filter thus places greater trust in the measurement and makes a stronger correction to the predicted state $\hat{\boldsymbol{x}}_j^-$.
- Conversely, if $\boldsymbol{\mathcal{P}}_j^-$ is low (due to low process noise $\boldsymbol{Q}$) and measurement noise $\boldsymbol{\mathcal{R}}$ is high, the

Kalman gain is small, and the filter relies more on its prediction $\hat{\boldsymbol{x}}_j^-$.

The updated state estimate is then computed as [125]:

$$\hat{\boldsymbol{x}}_{\boldsymbol{j}} = \hat{\boldsymbol{x}}_j^- + \boldsymbol{\kappa_j}(\boldsymbol{z}_j - \boldsymbol{\mathcal{H}}\hat{\boldsymbol{x}}_j^-) \tag{30}$$

This correction is applied after acquiring the measurement $\boldsymbol{z}_j$. Here, the difference $(\boldsymbol{z}_j - \boldsymbol{\mathcal{H}}\hat{\boldsymbol{x}}_j^-)$ is known as *innovation*.

Finally, the *a posteriori* error covariance is updated [125]:

$$\boldsymbol{\mathcal{P}_j} = (\boldsymbol{I} - \boldsymbol{\kappa_j}\boldsymbol{\mathcal{H}})\boldsymbol{\mathcal{P}}_j^- \tag{31}$$

This new value, which is generally lower (or, in the limiting case, equal) to $\boldsymbol{\mathcal{P}}_j^-$, reflects the filter's increased confidence in its predictions as a result of incorporating the new measurement, and defines how much certainty the filter has about its state estimate for the next step.

3.5 Fatigue Crack Growth Rate Assessment

Fatigue crack propagation is one of the key areas in fracture mechanics, focusing on the behavior of materials under cyclic loading. Accurate crack length measurement is essential in this context, as it provides the basis for calculating the FCGR—an important parameter for evaluating fatigue-related material properties.

The discussion below introduces the fundamental terms, variables, and relationships used in FCGR analysis. It provides a concise overview rather than a comprehensive treatment of fracture mechanics.

3.5.1 Key Terms and Variables

The following variables are central to evaluating fatigue crack growth [89]:

- Crack size/length – a geometric measure of a crack in a material. Standard terminology uses the terms crack size, crack length, crack depth, and estimated crack size interchangeably*[126]*. In this thesis, from this point onward, a strict distinction is made between:
    - $\mathbb{a}$: Crack size, which, aligned with the definition in standard *[126],* corresponds to the measure taken:
        - for the CT specimen from the line connecting the loading points to the crack tip.
        - for the middle tension (MT) specimen from the center line to the crack tip, typically referred to as the half-crack size. The total crack size is therefore $2\mathbb{a}$.
    - a: Crack length, which here corresponds to the measure taken from the notch tip to the crack tip. It can be defined following the standardized terms *[126]:*

$$a = \mathbb{a} - \mathbb{a}_n \tag{32}$$

      where $\mathbb{a}_n$ is the notch length. This convention is used for convenience, as it matches the direct output of the presented methodology, helps differentiate between values that come directly from the proposed methodology and those used in subsequent evaluations, and reminds the reader to add the notch length to the results.

- $\frac{da}{dN} = \frac{d\mathbb{a}}{dN}$: FCGR – increment of crack size/length per load cycle. When calculating FCGR from either crack sizes or crack lengths, the result is the same, because the constant notch length cancels out when calculating $d\mathbb{a}$ or $\Delta\mathbb{a}$ in FCGR. Hence, $d\mathbb{a} = da$, $\Delta\mathbb{a} = \Delta a$, regardless of whether crack size or crack length is used.
- K: SIF – quantifies the combined influence of load, crack size, and geometry on the stress state at a crack tip. Only Mode I (opening mode) is considered here. The unit is $MPa\sqrt{m}$. Since crack size is often measured in millimeters, convert it to meters before any calculations that involve SIF. After those calculations, it is assumed in this thesis that the resulting quantities (except those related to SIF) are then converted from meters to millimeters – e.g., the FCGR.
  Note: for SIF-related calculations, it is essential to use the crack size strictly.
- K_{max}, K_{min}: Maximum and minimum SIFs during a load cycle.
- R: Stress ratio – defined as:

$$R = \frac{\sigma_{min}}{\sigma_{max}} = \frac{P_{min}}{P_{max}} = \frac{K_{min}}{K_{max}} \tag{33}$$

  where σ is the nominal far-field stress and P is the applied load. The typical values are $-1 \leq R < 1$.
- $\Delta P = P_{max} - P_{min}$: Load range during one cycle.
- $\Delta K = K_{max} - K_{min}$: SIF range per cycle. This may also be expressed as

$$\Delta K = (1 - R)K_{max} \tag{34}$$

- $\Delta K_{eff} = K_{max} - K_{op}$: Effective SIF range, accounting for crack closure via the opening SIF K_{op}. This represents the effective driving force for fatigue crack growth, based on the assumption that only the open portion of the load cycle contributes to material damage.
- ΔK_{th}: Threshold SIF range, below which fatigue crack growth does not occur. Although sometimes treated as a material property, it depends on the R ratio.
- K_c: Critical SIF – the value of K at which unstable fracture occurs. It depends on specimen thickness, since thickness influences the level of crack-tip constraint[19]. Under plane-strain conditions, K_c reaches a lower limiting value, denoted K_{IC} (fracture toughness), which is considered a material property.

3.5.1.1 Practical Calculations

For practical calculations, ΔK can be expressed for [19]:

- CT specimen:

$$\Delta K_{CT} = \frac{\Delta P}{B\sqrt{W}} Y_{CT}(\alpha), \alpha = \frac{\mathbb{a}}{W}, 0.2 < \alpha < 1 \tag{35}$$

  where B is specimen thickness, W is specimen width (measured from the loading axis), and

[19] refers to the degree to which plastic deformation at a crack tip is restricted by the surrounding material. High constraint (such as in thick specimens under plane-strain conditions) leads to higher triaxial stresses and promotes brittle fracture behavior. Low constraint (such as in thin specimens under plane-stress conditions) allows greater plastic deformation and reduces crack-tip triaxiality, promoting more ductile behavior [89].

$Y(\alpha)$ is the geometry correction function that accounts for finite specimen dimensions:

$$Y_{CT}(\alpha) = \frac{(2+\alpha)}{(1-\alpha)^{\frac{3}{2}}}(0.886 + 4.64\alpha - 13.32\alpha^2 + 14.72\alpha^3 - 5.6\alpha^4) \quad (36)$$

- MT specimen:

$$\Delta K_{MT} = \frac{\Delta P}{BW}\sqrt{\pi a \sec(\pi\alpha)}, \alpha = \frac{a}{W}, 0 < 2\alpha < 0.95 \quad (37)$$

3.5.2 Modeling of Fatigue Crack Growth

The fatigue crack growth behavior of metals typically follows a characteristic sigmoidal curve, as schematically illustrated in Fig. 19. This curve can be divided into three regions. In the near-threshold regime, or Region I, the FCGR approaches zero as ΔK approaches the threshold value ΔK_{th}.

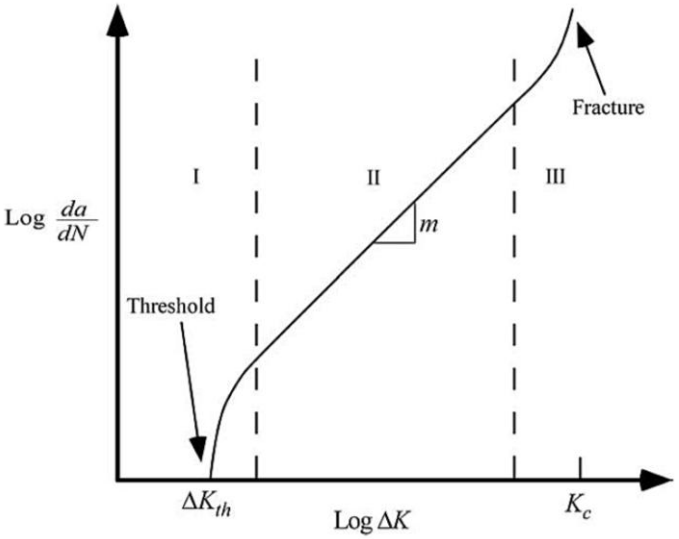

Fig. 19: Typical fatigue crack growth behavior in metals [89]

The intermediate portion of the curve, Region II, exhibits a nearly linear relationship between the FCGR and ΔK when plotted on log–log coordinates. This regime is comparatively insensitive to microstructural factors such as grain size and flow properties[20], in contrast to Regions I and III where such influences are more pronounced. Finally, Region III corresponds to the stage of rapid crack growth, where the crack propagation rate accelerates sharply until final fracture occurs as K_{max} approaches the critical value K_c [89].

3.5.2.1 Empirical and Analytical Models

In Region II, the relationship between FCGR and ΔK is often described by the Paris Law [89]:

$$\left(\frac{da}{dN}\right)_{PL} = C_{PL}\Delta K^{m_{PL}} \quad (38)$$

[20] describe a material's resistance to plastic deformation once yielding has begun. They are usually obtained from the uniaxial stress–strain curve measured in a tensile test and include parameters such as the yield strength, ultimate tensile strength, and strain-hardening behavior.

where C_{PL} and m_{PL} are material constants.

When the effect of crack closure is included, a modified form is obtained, which has been widely used to correlate fatigue crack growth data at various R ratios [89]:

$$\left(\frac{d\mathbb{a}}{dN}\right)_{PL,mod} = C_{PL}\Delta K_{eff}^{m_{PL}} \tag{39}$$

Many researchers have developed equations to model all or part of the sigmoidal FCGR behavior. Among these, the most widely used expression for describing crack growth across all three regions was developed at NASA [89]. It can be written as [127]:

$$\left(\frac{d\mathbb{a}}{dN}\right)_{NG} = C_{PL}\Delta K_{eff}^{m_{PL}}\left[1-\frac{\Delta K_{th}}{\Delta K}\right]^{p_{NG}}\left[1-\frac{K_{max}}{K_c}\right]^{-q_{NG}} \tag{40}$$

where p_{NG} and q_{NG} are material constants.

It is often called the NASGRO crack growth equation/model, coming from the connection of NASa and GROwth [128]. This model captures the transitions between the three regimes: in the near-threshold region, the ΔK_{th} term governs; in Region III, behavior is dominated by the K_c term; while in the intermediate regime, the equation effectively reduces to the Paris Law form (equation (39)) [89].

The effective SIF range, ΔK_{eff}, is expressed as [127]:

$$\Delta K_{eff} = \frac{1-f_{NG}(R)}{1-R}\Delta K, R \in \langle -1, 1) \tag{41}$$

where $f_{NG}(R)$ is a crack opening function empirically formulated by Newman [129]:

for $1 > R \geq 0$:

$$f_{NG}(R) = \frac{K_{op}}{K_{max}} = A_0 + A_1 R + A_2 R^2 + A_3 R^3 \tag{42}$$

and for $-1 \leq R < 0$:

$$f_{NG}(R) = \frac{K_{op}}{K_{max}} = A_0 + A_1 R \tag{43}$$

The coefficients A_0 to A_3 depend on the maximum stress level ratio σ_{max}/σ_o and the constraint factor β ($\beta = 1$ for plane stress, $\beta = 3$ for plane strain). The flow stress σ_o is taken as the average of yield (σ_y) and ultimate (σ_u) strengths. The coefficients are given by [129]:

$$A_0 = (0.825 - 0.34\beta + 0.05\beta^2)\left[cos\left(\frac{\pi\sigma_{max}}{2\sigma_o}\right)\right]^{\frac{1}{\beta}} \tag{44}$$

$$A_1 = (0.415 - 0.71\beta)\frac{\sigma_{max}}{\sigma_o} \tag{45}$$

$$A_2 = 1 - A_0 - A_1 - A_3 \tag{46}$$

$$A_3 = 2A_0 + A_1 - 1 \tag{47}$$

For the MT specimen, the maximum stress is obtained directly as:

$$\sigma_{max,MT} = \frac{P_{max}}{A_{MT,nom}} = \frac{P_{max}}{BW} \tag{48}$$

where $A_{MT,nom}$ is the nominal cross-sectional area. In the CT specimen, however, the far-field stress is non-uniform due to eccentric pin-loading. In this case, σ_{max} is calculated as:

$$\sigma_{max,CT} = \frac{K_{max}}{Y(\alpha)\sqrt{\pi a}} \tag{49}$$

4 Cornerstone of the Proposed Methodology

The cornerstone of the methodology for crack length determination is a novel approach to crack length assessment using DIC and artificial intelligence, named the Inflection point method (IPM) [79]. The content of this chapter—though somewhat condensed—was presented in the article *Inflection point principle combined with digital image correlation and machine learning for crack length measurement in fatigue tests* published in *Theoretical and Applied Fracture Mechanics* [79].

The IPM is based on the inflection point principle, which has not yet been thoroughly validated for use with DIC data from fatigue tests of metallic materials. Therefore, this Chapter validates the IPM and its underlying principle for accuracy, robustness, and feasibility under uninterrupted testing.

The VIM serves as the baseline (reference) method for assessing the accuracy of the IPM, as it is primarily intended to be replaced by the IPM. The feasibility of continuous (uninterrupted) application is evaluated by collecting data during ongoing tests and assessing the accuracy of those results. Additionally, the STM is applied as a benchmark, representing a commonly used DIC-based approach, to provide a comprehensive comparison with the IPM.

4.1 Experimental Program for IPM Development

The initial experimental program was designed with the final methodology in mind but includes adjustments to obtain high-quality data for validating the IPM and comparing it with a different DIC-based approach. Specific details of these adjustments are provided in the following subsections.

To ensure robust validation, the program considers the effects of different metals, sample thicknesses, and LLs. Special attention is given to LL changes, as the STM is extremely sensitive to this factor, which can vary not only between tests but also in a single test. For example, when determining the threshold value of SIF for unlimited fatigue life, the applied load is typically reduced in steps during the test.

4.1.1 Materials, Geometry, and Preparation

Standard CT samples according to the ASTM E647 [19] were used. The selected materials represent a range of commonly inspected metallic materials at the testing facility of the Institute of Physics of Materials of the Czech Academy of Sciences (hereafter *Facility*): low alloy steel 38MnVS6, stainless steel 1.4306, and aluminum alloy EN AW-7075. For stainless steel, three samples with different thicknesses (B) were available. For the other materials, two samples, each of the same thickness, were prepared. All samples had the same width (W), machined notch length ($\mathbb{a}_n$), and notch type. Tab. 1 details the specific dimensions and materials for each sample used in the experiment.

To enhance crack tip visibility for VIM, the sample surfaces were ground with SiC paper and polished using diamond paste with abrasive particles as small as $0.25\ \mu m$, resulting in a mirror-like finish. The grinding and polishing were done perpendicular to the expected crack path to avoid confusion between surface treatment marks and the crack itself. A polished band, $0.8\ to\ 1.2\ mm$ wide[21], was maintained

[21] which was chosen to be as narrow as practicable, allowing deformation measurements close to the advancing crack while remaining wide enough to reduce the risk of unusable tests—specifically, cases in which the crack could propagate beyond the polished band and become hidden by the speckle-pattern paint, thereby compromising the reliability of visual inspection. Where conditions such as material heterogeneity, anisotropy, asymmetric loading, or setup misalignment may cause crack-path deviation, a wider polished band may be necessary to maintain visibility throughout the test.

along the expected crack growth path, while the remaining area was coated with matte white paint and then partly covered with black paint. This created a random, anisotropic, and highly contrasting speckle pattern necessary for correct and precise DIC measurement. Fig. 20 shows the CT sample with the applied DIC speckle pattern and a detailed view of the polished band with visible surface treatment marks. This unprecedented sample preparation [79] allowed for the use of both VIM and DIC on the same side of the sample, effectively eliminating the influence of non-uniform crack growth across the sample thickness from the validation.

Tab. 1: Overview of standard CT samples for the experiment [79]

Material	*Pieces*	*W[a] [mm]*	*B[b] [W]*	*a_n[c] [W]*	*Notch type*
38MnVS6	2	50	0.2	0.25	Chevron
1.4306	1	50	0.1	0.25	Chevron
1.4306	1	50	0.2	0.25	Chevron
1.4306	1	50	0.3	0.25	Chevron
EN AW-7075	2	50	0.2	0.25	Chevron

[a] width, [b] thickness, [c] notch length

The mirror-like finish and preservation of the unspeckled band on the polished surface were implemented solely to facilitate validation and benchmark comparison; they are not required in the final methodology, which is designed to operate with a speckle pattern covering the entire region of interest (ROI). The preparation of the speckled surface can be done quite quickly, especially since samples can be prepared in batches (optimally 4–6 pieces). Preparing a speckle pattern on a batch of samples takes about 30 minutes. Therefore, the required surface preparation will not be more demanding or time-consuming than the polishing procedure used for samples intended solely for VIM measurements.

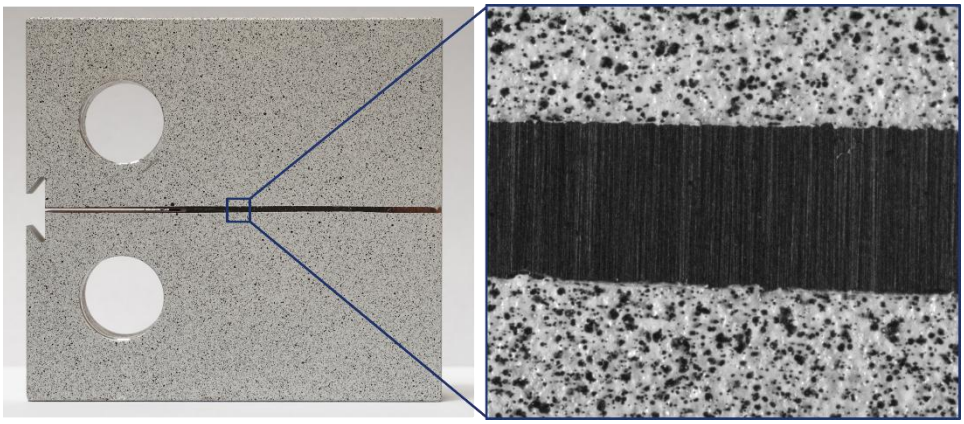

Fig. 20: CT sample with applied DIC speckle pattern (left) and the detail of the polished band and the speckles (right) [79]

4.1.2 Experimental Setup

The fatigue tests were carried out using an Amsler 20 HFP 5100 resonant pulsator machine. Images were captured with a FLIR 8.9-megapixel global shutter camera, equipped with a TC3MHR016-C telecentric lens at $m_{opt} = 0.85$ providing a viewing area of approximately $16.7 \times 8.8\ mm$. The global

shutter was crucial due to the high-speed movements during the experiment, as a rolling shutter camera would result in motion-induced image distortion. TL was selected for its advantages, as described in subsection 3.1.1.2, particularly its elimination of perspective errors and minimization of image distortion.

To compensate for the low lens speed and due to the short exposure time (0.5 ms), used to prevent motion blur, two 50 W LED lights were positioned close to the sample to provide adequate illumination. The camera was mounted on a slider for precise focus adjustment, given that TLs have a fixed $f\!\!\!/$ and shallow DoF. The experimental setup, including the arrangement of the optical system, is shown in Fig. 21.

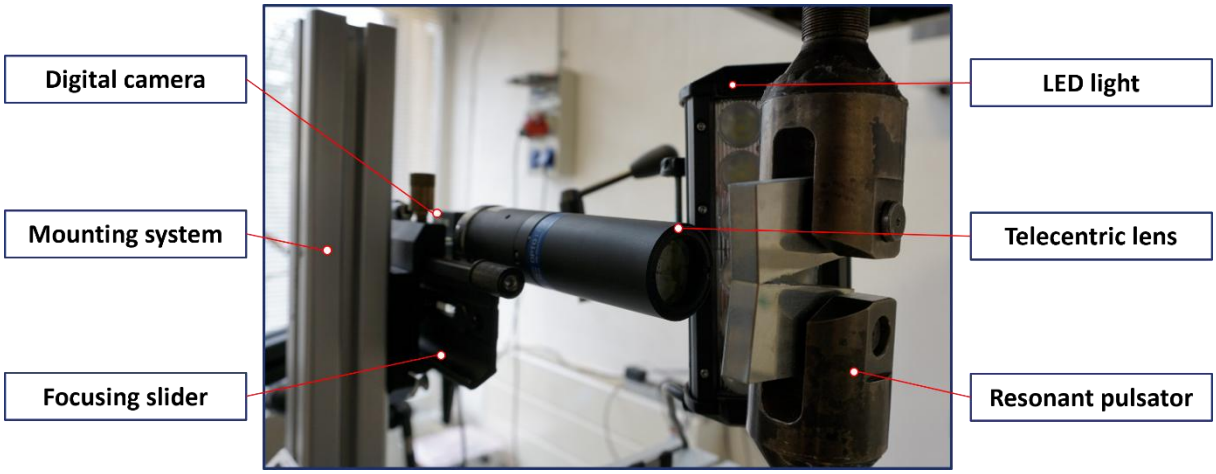

Fig. 21: Detail of the optical system in front of the testing machine [79]

4.1.3 Testing Procedure

Each test began with the calibration of the DIC using an object of known dimensions to determine the pixel-to-millimeter conversion ratio. Additionally, before the cycling started, an image of the undeformed sample was captured to serve as a reference for DIC deformation calculations.

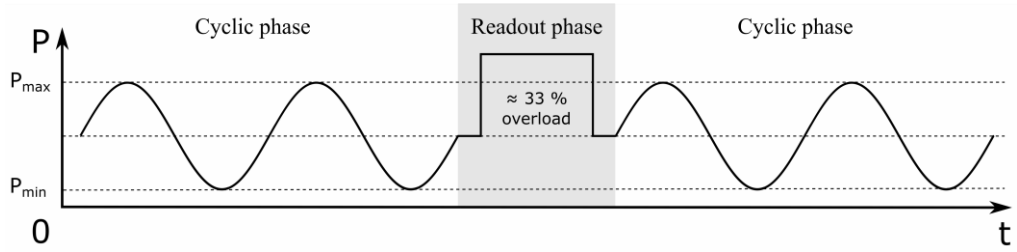

Fig. 22: Scheme of the testing procedure, including periodic halting (readout) between cyclic phases and application of overload during the readout [79]

Throughout the experiment, the test was periodically halted (referred to as readout) at various crack lengths to gather high-quality images for the VIM. These images also formed the static dataset for the IPM and DTM. The stopping intervals were based on previous crack length increments (CLIs) in an attempt to achieve the most uniform distribution of crack lengths. To enhance the visibility of the crack tip, an overload of approximately 33% (assessed empirically) above the maximum cyclic load (P_{max}) was applied during the readout. This approach was required to ensure a level of crack visibility similar to what is provided by a standard traveling microscope, which usually targets a small region close to the crack tip. In contrast, the experimental setup in this study was designed to image a much broader area,

enabling observation of the complete crack growth trajectory during the test and removing the need for any camera repositioning.

Since the objective was to compare measured crack lengths between methods rather than to investigate FCGR, this overload did not adversely affect the results. The testing procedure, including periodic halting and the application of overload, is shown in Fig. 22. The readout phase is not part of the proposed methodology and was introduced only for purposes of IPM development and validation.

The test frequency was determined by machine–sample dynamics and could not be manually adjusted. For this experiment, the cycle frequency typically started around 90 Hz and gradually decreased to approximately 60 Hz as the growing crack reduced the stiffness of the sample.

4.1.4 Load Levels

The cycle parameters were set for a stress ratio $R = 0.1$, representing the pulsating tension cycle commonly used for such tests at the Facility. Higher forces were applied initially for crack initiation up to approximately 1 mm in length. Subsequently, the LL corresponding to P_{max} was set, as detailed in Table 2. For the materials with two identical CT samples, P_{max} slightly differed to introduce additional variations regarding LLs for the validation. Overall, the P_{max} was assessed using the known crack growth properties, as the selected materials were previously tested at the Facility, aiming to achieve adequate crack growth during one working day due to limited availability of the testing machine.

Tab. 2: Overview of applied loads (P_{max}) for cycling after crack initiation [79]

Material	*Piece No.*	P_{max} *[kN]*
38MnVS6	1	6.5
38MnVS6	2	5.5
1.4306	1	10.8
1.4306	2	7.2
1.4306	3	3.7
EN AW-7075	1	3.6
EN AW-7075	2	2.7

In the case of the EN AW-7075 No. 1 sample, the selected load was excessively high, causing the crack to deviate from the plane of symmetry early in the test (approximately 2 mm from the notch), and the crack tip became hidden under a layer of paint. Therefore, VIM was not applicable, and the dataset obtained from this sample is excluded from further analysis due to the missing validation data. The test of the EN AW-7075 No. 2 sample was consequently conducted with a lower load. Although the crack also deviated from the polished band for VIM, as the load was still too high, it did not occur until the crack reached a length of 8.5 mm. Thus, this dataset is considered usable for further processing as sufficient data was collected.

The proposed methodology does not involve applying such high LLs, so no complications regarding crack deviation from the straight direction are expected.

4.1.5 Data Acquisition during Ongoing Tests

Part of the validation procedure was to assess the feasibility of data collection during the ongoing test and to evaluate the performance of the proposed method on images captured without stopping the experiment. This is another cornerstone of the proposed methodology and is also recommended by ASTM E647 [24]. This was achieved using a synchronization device that monitored the force readings from the testing machine [79]. The device sent a triggering impulse to the camera at the moment of maximum force (when the crack was most open) to capture an image after skipping n_{sync} cycles, as is later schematically depicted in Fig. 45. For this experimental program, n_{sync} was set to 100.

Subsequently, this approach was used to identify the first image after the ramp-up phase of the test following each readout. These images were used to construct the dynamic dataset, ensuring a representative comparison to the baseline. This is based on the assumption that the crack did not grow—or grew only negligibly—during the ramp-up phase. The dynamic dataset was then used to assess the performance of the IPM during the ongoing experiment.

4.2 Application and Selection of Methods

To clarify the implementation of the methods, the direction perpendicular to the expected crack path is denoted *y* (vertical), while the direction along the crack path is denoted *x* (horizontal). The positive x-direction coincides with crack growth. The origin is at the notch tip, so the x-coordinate equals the distance from the notch tip. Thus, the crack length is the x-coordinate of the crack tip. This coordinate system is shown in Fig. 24 and applies throughout Chapters 4 – 7 unless indicated otherwise.

4.2.1 Visual Inspection Baseline

To avoid confirmation bias, the VIM was applied at the very beginning of the data processing phase, before examining the results from the IPM and DTM.

The crack initiation point at the notch tip, labeled as A_c, was identified manually once for each dataset (test), and its location was subsequently tracked in all images using DIC, with each image representing one readout from the experiment. A single evaluator then assessed the coordinates of the crack tips to ensure consistency, and all images within each dataset were evaluated collectively without unnecessary delays. Fig. 23 shows examples of the area around the crack tip (red) for each material.

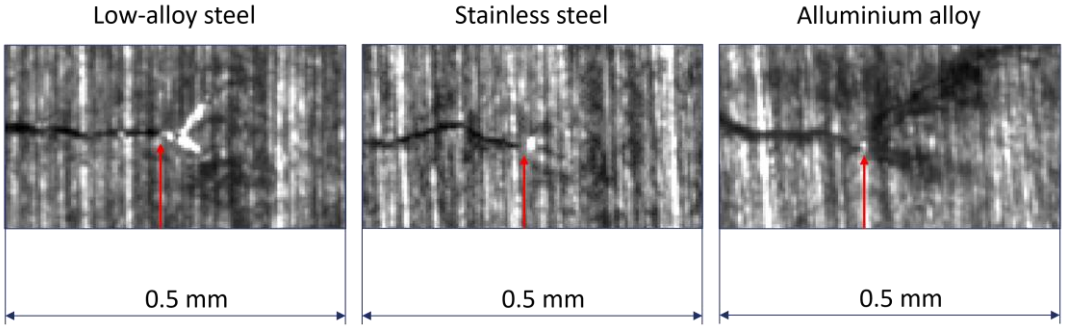

Fig. 23: Examples of the area around the crack tip (red mark) for each material [79]

When analyzing images to determine the crack tip position, it was taken into consideration that the resolution of the imaging system is inherently limited by light diffraction and imperfections in the

imaging system, resulting in some degree of blurring of the crack tip. Additionally, various bright and dark vertical marks from grinding and polishing in the background made accurate determination of the crack tip's position more challenging due to reduced contrast in dimmer areas. To address these factors, a readout error interval for the crack tip's x-coordinates was introduced.

This interval is based on two particular points along the x-direction in the area around the crack tip: the first point, B_{cL}, is where the crack tip is reliably visible, while the second point, B_{cR}, is where the crack is no longer reliably visible. The length l_{ct} of the crack tip readout error interval is defined as the difference between their x-coordinates. A new point, B_c, is then established at the midpoint between B_{cL} and B_{cR}. The baseline crack length, a_b, is calculated using the equation [79]:

$$a_b = \left(x_{B_c} - x_{A_c}\right) \pm \frac{l_{ct}}{2} = a_{bm} \pm \delta_{cl} \tag{50}$$

where δ_{cl} represents the crack length assessment error. The middle baseline crack length, a_{bm}, is determined using the midpoint of the estimated readout error interval. The schematic representation in Fig. 24 shows the points and variables applied in the determination of baseline crack lengths.

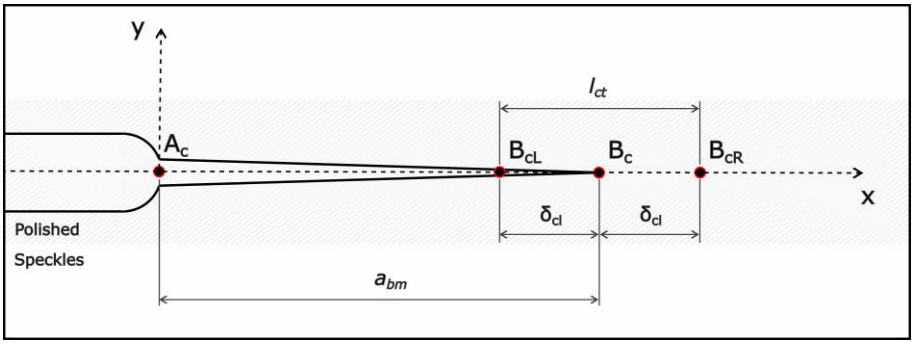

Fig. 24: Schematic representation of the points and variables applied in the determination of baseline crack lengths [79]

The error distribution was positively skewed, and no general dependence of its value on the crack length was observed. Tab. 3 provides a statistical summary of the crack length assessment errors, including the maximum, minimum, mean, and standard deviation values, all rounded to the nearest half micrometer.

Tab. 3: Statistical summary of crack length assessment errors (δ_{cl}) – for readability converted from mm to µm [79]

Material	*Piece No.*	*min* δ_{cl} [μm]	*mean* δ_{cl} [μm]	*std* δ_{cl} [μm]	*max* δ_{cl} [μm]
38MnVS6	1	5.5	14.5	6.0	29.0
38MnVS6	2	5.0	14.0	5.5	28.0
1.4306	1	4.0	14.5	5.5	22.5
1.4306	2	6.0	14.0	6.0	24.0
1.4306	3	8.5	16.5	5.0	24.0
EN AW-7075	2	8.5	16.5	4.5	21.5

4.2.2 Image Processing and Data Extraction

To implement the DTM and to continue with the development of the IPM, deformations were extracted from the available images using DIC. For this task, the commercial software Alpha DIC from X-Sight was utilized. Within the software, a series of line segments perpendicular to the crack path served as VEs. Their displacements between consecutive images were monitored by the DIC algorithm with subpixel resolution.

A total of one thousand equidistantly placed VEs ($n_{ve,d} = 1000$)[22] were used for development, spanning a width of $w_{ve,d} = 14.5\,mm$, with each VE having a length of $l_{ve,d} = 1.5\,mm$. Both variables are shown in Fig. 23. The choice of $l_{ve,d}$ was based on ensuring that the entire correlation subset (also referred to as the subset or template) was positioned on the speckle pattern as close to the polished band as possible. The center of each subset corresponds to the endpoint of the respective VE.

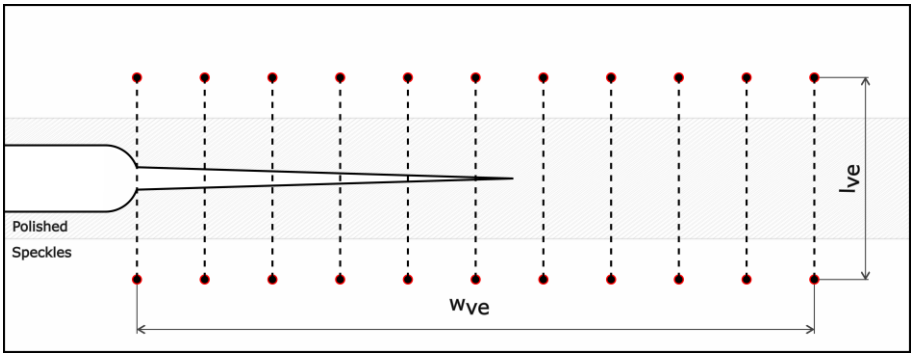

Fig. 25: Schematic illustration of the VEs (virtual extensometers) placement in the current experimental program, showing the defined variables used in the IPM (Inflection point method) [79]

The dimensions of the subset are a key factor in the quality of the obtained DIC results. Selecting the subset size requires balancing the benefits of a larger subset, which improves measurement precision by capturing a sufficient number of speckles for correlation and averaging out noise from the image acquisition process, against the advantages of a smaller subset, which provides higher spatial resolution with lower computational demands [113].

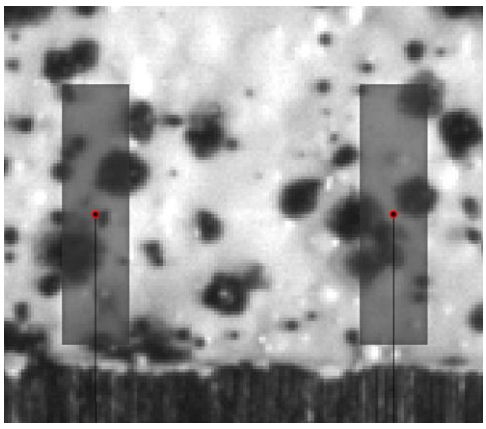

Fig. 26: Detailed view of the utilized speckle together with its positioning and underlying speckle pattern [79]

Consequently, a rectangular subset with a smaller width $w_{sub,d} = 21\,px$ in the x-direction, ensuring

[22] where the subscript *d* indicates a value used during method development and not necessarily the final value in the IPM. The same convention applies to other parameters below.

good spatial resolution for crack tip localization, and a larger height $h_{sub,d} = 81\ px$ in the y-direction, capturing enough distinctive features, was chosen for the IPM development to combine the advantages of both large and small subsets. A detailed view of the subset together with the underlying speckle pattern is shown in Fig. 26.

Finally, Tab. 4 provides a comprehensive overview of the experimental DIC settings and performance according to the [20].

Tab. 4: Experimental DIC settings and performance (Alpha DIC software by X-Sight) [79]

Technique used	2D digital image correlation
Subset size	21 x 81 px
Maximal shift of the point[a]	68 px (84% of the subset size)
Shape function	Affine and Perspective
Interpolation function	Yes (type not shared by developers)
Correlation criterion	Zero mean normalized sum of squared differences (ZNSSD)
Pre-smoothing applied to the images	None
Camera	12-bit, 4096 x 2160 px
Field of view	16.6 mm x 8.8 mm
Displacement resolution [b]	± 0.04 µm or 0.01 px
Strain resolution [c]	± 2.67×10^{-5}

[a] at the location: End points of the virtual extensometers (VEs) at the notch tip; Time point: Last in the dataset; [b] according to [130]; [c] for l_{ve}= 1.5 mm, which is the smallest length of VE

4.2.3 Strain Threshold Method as the Benchmark

Building upon the deformation data extracted from DIC, the DTM was implemented to serve as the benchmark representing the currently used 1D DIC evaluation approach for the comparison with the proposed IPM, specifically its variant using strains (STM).

Strains were obtained directly from the VE results by dividing their elongation by the initial length. The spatial resolution of the method was enhanced by linearly interpolating the discrete deformation points.

The primary difficulty in applying the STM lies in accurately determining the threshold value ε_{th} . Since investigating the correct ε_{th} determination is beyond the scope of this work, it was chosen based on results obtained from VIM, ensuring optimal STM performance for each dataset. The selection was based on minimizing the sum of the least-squares differences between the crack lengths predicted by STM (a_{STM}) and a_{bm}, which is referred to as the adjacency criterion. Tab. 5 summarizes the ε_{th} values that satisfy the adjacency criterion for each dataset (sample) and which are used for further analysis.

Tab. 5: Overview of strain threshold values (ε_{th}) that meet the adjacency criterion [79]

Material	Piece No.	ε_{th} [%]
38MnVS6	1	1.10
38MnVS6	2	0.90
1.4306	1	0.60
1.4306	2	0.65
1.4306	3	1.15
EN AW-7075	2	0.75

In the process of selecting these values, a significant limitation of the method was identified: a constant threshold value cannot accurately estimate crack lengths across a wider range. This limitation is illustrated in Fig. 27, which shows the results from applying three different threshold values.

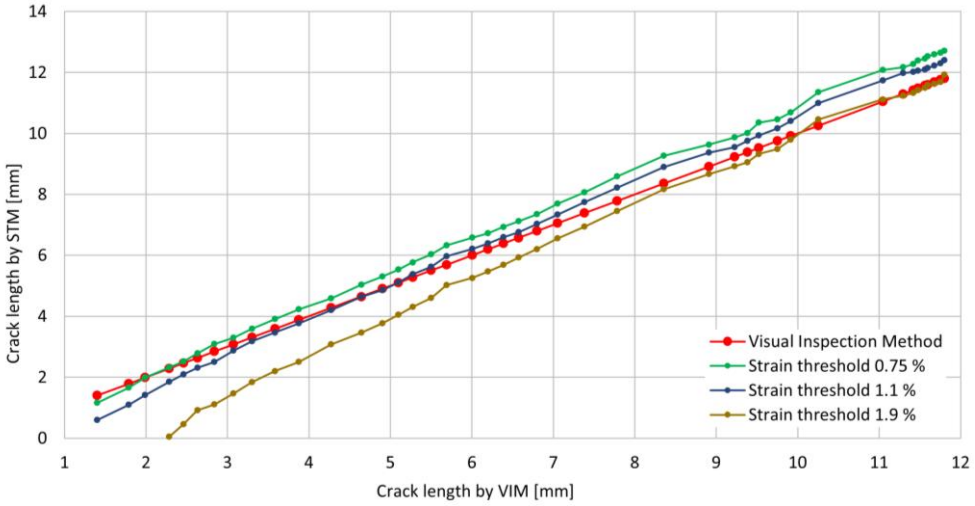

Fig. 27: STM (Strain threshold method) results for three different threshold values compared with VIM (Visual inspection method) results for low-alloy steel sample No. 1

The threshold value $\varepsilon_{th} = 0.75$ % aligns well with the VIM results at the beginning of the experiment, while the threshold of $\varepsilon_{th} = 1.9$ % only matches well at the end. Finally, the threshold value of $\varepsilon_{th} = 1.1$ % produces results that satisfy the adjacency criterion.

4.2.4 Regression for IPM

The datasets generated by DIC, which are used as inputs to the IPM, are referred to as COD projection (CODP) curves. To create the CODP curve, the change in the length of each VE was plotted as a function of its distance from the notch. Formally, it could be defined as

$$CODP\left(x_{l_{ve,k}}\right) = \Delta l_{ve,k}, k \in \{0, \dots, n_{ve} - 1\} \tag{51}$$

where $x_{l_{ve,k}}$ denotes the distance of the k^{th} VE from the notch tip. Additionally, primarily for plotting purposes (this has no effect on the crack-length results), the corresponding mean value within the crack ligament was subtracted from each point of the respective CODP curve. These curves qualitatively

represent the crack opening displacement along the crack faces, though they are not quantitatively identical, particularly near the IP location, where they should follow the dependencies described in 2.4 ($r^{\frac{3}{2}}, \theta = \pi\ rad$, and $r^{\frac{1}{2}}, \theta = \pi\ rad$). The shape of the CODP curve is affected by, for instance, the material, LL, l_{ve}, w_{sub}, h_{sub}, camera resolution, and optical noise/distortion.

A regression technique was required to convert the data points from CODP curve into a form that could be used to identify the IP location. For the reasons discussed in this subsection (4.2.4), methods requiring an explicit fitting formula were not used; polynomial regression was also avoided because its results depend strongly on the selected polynomial degree. Instead, the focus was placed on a regression method with a minimal number of parameters, no explicit formula, smooth derivatives of the CODP curve, robustness to noise, and support for locating the IP at any point along the crack path.

Three potential regression methods were selected for further evaluation: Savitzky-Golay filtering (SGF), support vector regression (SVR), and GPR. SGF, which utilizes local least-squares fitting of the data through polynomials, is a widely used technique for smoothing data and estimating derivatives from noisy data [131]. However, SGF's results are confined to the existing data points in CODP curve, meaning that to improve spatial resolution, either more VE must be added, or an additional interpolation procedure is required. This drawback makes SGF less favorable compared to SVR and GPR.

In contrast, both SVR and GPR allow for generating new data points between existing ones without the need for a separate interpolation method. Comparisons of SVR and GPR [132], [133] demonstrated that GPR performs better, making it the preferred option. Notably, GPR produced the most promising results when applied and compared to the other two methods on the actual data used in this study. While neural networks were also considered, they were ruled out due to GPR's significantly lower number of required *hyperparameters*[23] (hpars) to perform the equivalent task, which makes it easier to implement, analyze, and fine-tune [120].

4.3. Inflection Point Method

The development began with the design of a basic framework on artificially generated data, which formed the foundations of Phase 1. Subsequent progress was guided by qualitative analysis during the implementation of the evolving IPM on a static dataset. This involved detailed examination of the resulting curves and their first and second derivatives to assess conformity with the expectations established for the inflection point principle, as described in the preceding sections, particularly in section 2.4.

The final IPM algorithm comprises three phases. The details of each phase, along with various conditions, corrections, parameters, and hyperparameters, and their sequence and interrelationships are discussed in the following subsections.

4.3.1 IPM Phase 1

In the first phase (P1), referred to as GPR global, regression is performed on the entire CODP curve. For the initial CODP curve in a measurement sequence, the optimization is run with ten random restarts to ensure thorough exploration of the design space—this is denoted as “Global hpars optimization” in Fig. 30. For subsequent CODP curves, the optimization runs only once, initialized from the optimal

[23] control the learning process of a machine-learning model.

hyperparameters obtained in the previous GPR global step. This is referred to as "Local hpars optimization" in Fig. 30, both in P1 and in other phases where hyperparameter optimization is performed only once. This technique assumes that consecutive CODP curves will not differ significantly, leading to only minor adjustments in hyperparameters and improving the efficiency of the optimization process.

4.3.1.1 Hyperparameter Optimization Bounds

A study using the final IPM was conducted to determine the intervals of hyperparameters within which optimization is performed (further referred to as *Study of hyperparameters*). For each GPR regression phase of the IPM, optimization is carried out with 20 restarts, each using random initialization of parameters. In this investigation, very broad intervals, as defined by equations (52) and (53), were chosen for the initialization and optimization of the hyperparameters, in order to thoroughly explore a wide range of possible combinations.

$$\ell_{study} \in (0.05, 10)\ mm \tag{52}$$

$$\sigma^2_{n,study} \in \left(10^{-10}, 10^{0}\right)\ mm^2 \tag{53}$$

The final design space for the hyperparameters was then established based on the results from this study on both static and dynamic datasets, which are collectively presented in Fig. 28. A safety margin was added to the highest and lowest values obtained, resulting in the lower (subscript *l)* and upper (subscript *u)* bounds for length scale ℓ and noise level $\sigma^2_{n,}$, as defined by equations (54) and (55) [79]. Also, the boundaries in Fig. 26 correspond to these resulting bounds:

$$\ell_f \in \left(\ell_{l,f}, \ell_{u,f}\right) = (0.3, 3)\ mm \tag{54}$$

$$\sigma^2_{n,f} \in \left(\sigma^2_{n,l,f}, \sigma^2_{n,u,f}\right) = \left(10^{-6}, 10^{-1}\right)\ mm^2 \tag{55}$$

where the subscript *f* means that the value belongs to the final IPM setup. The same rule also applies to other parameters.

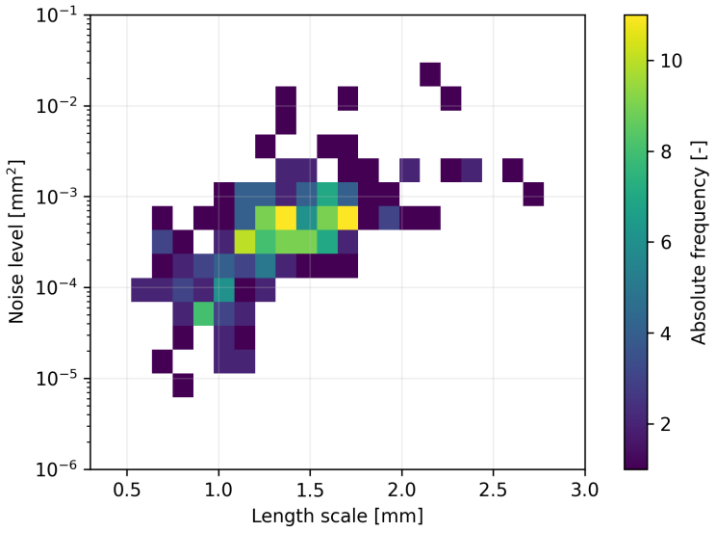

Fig. 28: Values of Gaussian process regression hyperparameters from the static and dynamic datasets [79]

During the development of the method, when many parameters and subprocesses were changing

dynamically, an approach equivalent to that described in the study of hyperparameters was employed.

4.3.1.2 Reducing Computational Demands

Conducting GPR on a CODP curve derived from a thousand VE was found to be very time-consuming, so efforts were made to determine an optimal number of points to use. Based on an analysis of GPR prediction results and computation times, it was decided to use every $n_d{}^{\text{th}}$ point from the original CODP curve, with this parameter, called the global data decimation level for the development, set to 10. This approach significantly reduced computational time while maintaining the accuracy of the method. The choice of $n_d = 10$ is further discussed in the sensitivity study in section 4.4.

4.3.2 IPM Phase 2

To improve the accuracy of the IPM, additional phases were introduced to address challenges encountered during the P1 regressions. Specifically, close examination of the CODP curves and GPR global results revealed that the GPR global sometimes failed to accurately capture the inflection point (IP) due to sharp transitions between convex and concave regions of the CODP curve, as demonstrated in Fig. 29. This shortcoming led to the development of phase 2 (P2), known as GPR localization, where regression is applied only to the data within the localization interval [79]:

$$\mathcal{I}_{(r,d),i} = < x_{ip1,i} - 0.2w_{ve,(r,d)}, x_{ip1,i} + 0.2w_{ve,(r,d)} > \tag{56}$$

Here, $x_{ip1,i}$ represents the predicted IP location from P1, the value 0.2 is the localization interval factor ($F_{li,f}$), and i denotes the ordinal number of the current IPM iteration. Generally, i is also used as the ordinal number of the iteration for the IPM modifications presented in Chapters 5 and 6. Additionally, the local data decimation level ($m_d = 6$) for development was selected in the same manner as n_d in P1.

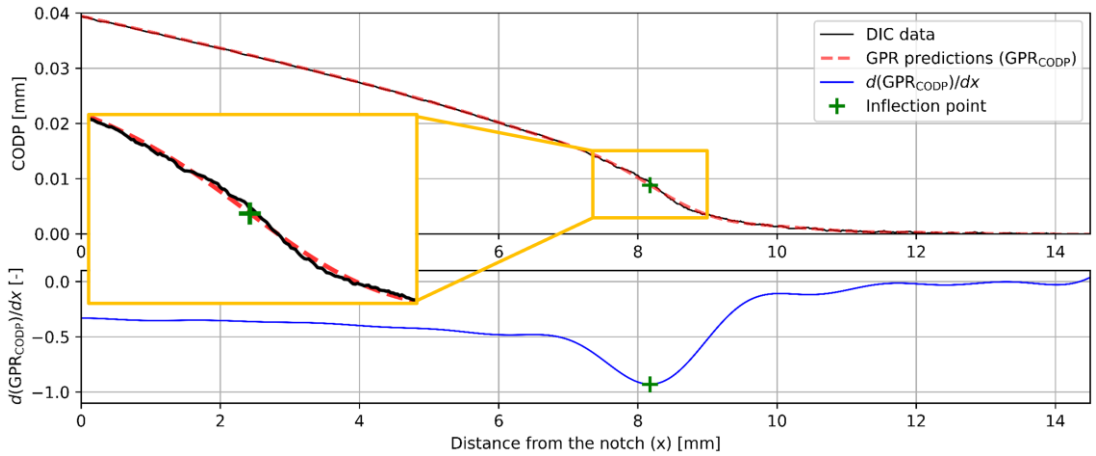

Fig. 29: Example of training data from DIC and Gaussian process regression (GPR) global predictions; localization of the IP (inflection point) using the first derivative of GPR (bottom); detail of the sharp transition around the IP (left), which is not properly captured by the GPR global; for EN AW-7075 No. 2 sample [79]

This localized approach, in which $x_{ip2,i}$ denotes the predicted IP location from this phase, yielded better results overall compared to the GPR global. However, the outcomes were still not fully satisfactory, particularly for shorter cracks up to around 2.5 mm. This was due to the low values in CODP curve, and the impact of higher loads used for crack initiation. In some of these cases, the most prominent IP was detected close to the notch tip, yielding a crack length below 0.5 mm.

4.3.2.1 Corrections for Short Cracks

Corrective actions were implemented for cases that meet Condition 1, defined as [79]:

$$x_{ip1,i} < 1\,mm \tag{57}$$

The correction differed in the following two scenarios. For the first $CODP_{i=0}$ processed by the algorithm, Correction 1 (C1) involved increasing the $F_{li,f}$ by 0.1 in this specific iteration [79]:

$$\mathcal{I}_{C1,(r,d),i} = < x_{ip1,i} - 0.3w_{ve,(r,d)}, x_{ip1,i} + 0.3w_{ve,(r,d)} > \tag{58}$$

Correction 2 (C2) was then implemented for all subsequent iterations, with the adjusted interval for GPR localization defined as [79]:

$$\mathcal{I}_{C2,(r,d),i} = < a_{IPM,i-1} - 0.2w_{ve,(r,d)}, a_{IPM,i-1} + 0.2w_{ve,(r,d)} > \tag{59}$$

where $a_{IPM,i-1}$ is the final crack length from the preceding iteration.

4.3.3 IPM Phase 3

A thorough examination of the GPR localization results revealed that, in some cases, the P2 region contained two clearly distinct IPs. This contradicted the expected shape of the CODP curve based on the inflection point principle, and such cases are considered outliers in IPM results. To address these situations, an additional phase 3 (P3), termed GPR smoothing, was introduced and is activated when Condition 2 is not satisfied. Condition 2 has two components. The first component checks for the absence of another IP in front of the most prominent one by using the second derivative of the P2 GPR. The second component serves two purposes: it prevents over-smoothing and favors the results of P2, or possibly P3, results over those from P1. This component of Condition 2 can be expressed as [79]:

$$0.75\,\frac{dCODP_{P1,i}}{dx}\left(x_{ip1,i}\right) > \left[\frac{dCODP_{P2,i}}{dx}\left(x_{ip2,i}\right)\ or\ \frac{dCODP_{P3,i}}{dx}\left(x_{ip3,i}\right)\right] \tag{60}$$

where the value of 0.75 is referred to as the derivative distinction factor ($F_{dd,f}$), $x_{ip3,i}$ denotes the predicted IP location from this phase, and $CODP_{P1,i}$, $CODP_{P2,i}$, and $CODP_{P3,i}$ denote the reconstructed CODP curve (or its segment) from the GPR regression in phases 1 – 3 of IPM, respectively.

Regarding the P3 process itself, the only difference from P2 is the lower bound for ℓ, which is defined as [79]:

$$\ell_{l,i}^{P3} = \frac{\ell_{opt,i}^{P2} + \ell_{opt,i}^{P1}}{2} \tag{61}$$

where $\ell_{opt,i}^{P2}$ and $\ell_{opt,i}^{P1}$ represent the optimal length scale values obtained from P2 and P1, respectively. This adjustment prevents the GPR from fitting too closely to the underlying data, ensuring the desired smoothing effect. Only a single smoothing pass is permitted ($n_{s,f} = 1$). For hyperparameter optimization, both P2 and P3 use the optimal values from P1 as the initial guess.

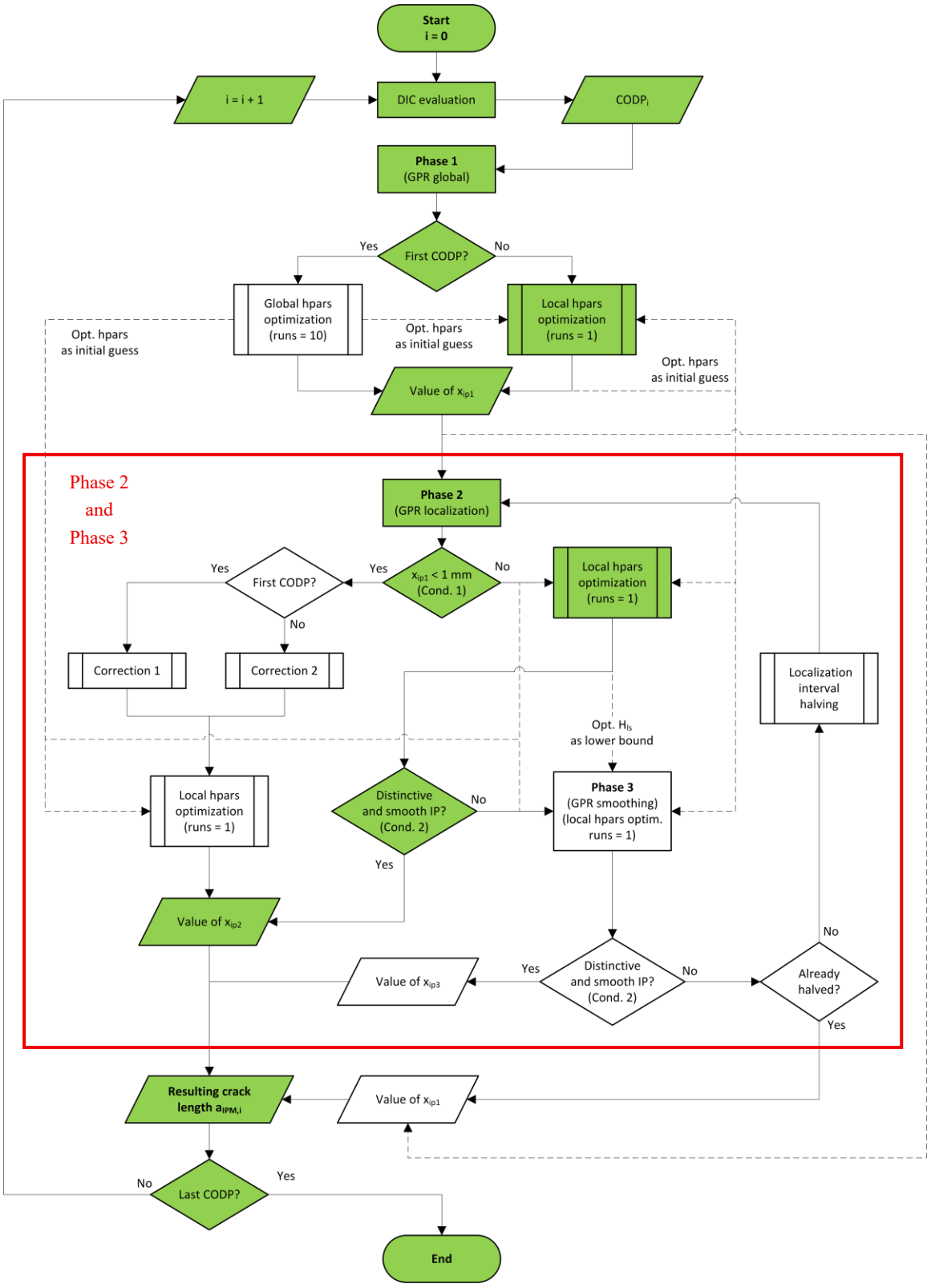

Fig. 30: IPM (Inflection point method) flowchart, showing individual sub-processes, decision points (conditions), corrections, and the flow of key values (especially hyperparameters) which are illustrated in the dashed lines and which perform the update of the receiving blocks immediately as the source block is finished. The most frequent path is highlighted in green. The red outline indicates encapsulation for the flowchart in Fig. 43. Legend: Rectangle – process/operation; Rectangle with double vertical lines on the sides – subprocess/module/function; Diamond – decision; Parallelogram – values of input/output variables; Rounded rectangle – start/end of the entire algorithm [79]

4.3.4 Repeating Phases 2 and 3

If the results after smoothing still do not satisfy Condition 2, the interval used for GPR localization is reduced by half using the interval decrement factor ($F_{id,f} = 2$). Then, P2 and possibly P3 are repeated—this is referred to as *Second* P2/P3. In this manner, the previously performed P2 and P3 will be referred to as *First* P2/P3. The rationale behind this step is to allow these phases to address the qualitatively incorrect phenomena for which they were introduced. When such issues occurred, it was observed that reducing the localization interval often helped to resolve them.

The algorithm permits only one halving to avoid having too little data for regression. If Condition 2 remains unmet after the Second P2/P3, their results are considered incorrect, and GPR global is assumed to be correct, although possibly less precise. In this case, the $x_{ip1,i}$ serves as the final crack length for the current iteration, denoted as $a_{IPM,i}$, which is also referred to as resulting crack length in Fig. 30, sections 4.4 – 4.6 and Chapters 5 – 6.

4.3.5 Overview of the IPM

An overview of the proposed IPM is presented in the flowchart shown in Fig. 30. This figure illustrates the main processes, sub-processes, decision points, and the flow of key values and their interrelationships, as described in the previous subsections.

4.4. Sensitivity Analysis

This section examines how various parameters influence the performance and robustness of the IPM, which serves as the cornerstone of the entire methodology. The analysis is organized into three parts: variables related to image processing, parameters within the IPM algorithm, and test variables—of which only the LLs are addressed in this chapter. The other two test variables, material and sample width, are discussed in the following subsections. The analysis begins with the metrics.

4.4.1 Metrics and Definition

To assess the errors in the sensitivity analysis and compare the overall performance of the IPM and STM, three commonly used metrics from the field of machine learning regression were used [134]: Mean Absolute Error (MAE), Root Mean Square Error (RMSE), and Mean Absolute Percentage Error (MAPE). The definitions for MAE and RMSE are as follows [135]:

$$MAE = \frac{1}{N_{tp}} \sum_{i=1}^{N_{tp}} \left| a_{IPM,i} - g_i \right| \tag{62}$$

$$RMSE = \sqrt{\frac{1}{N_{tp}} \sum_{i=1}^{N_{tp}} \left(a_{IPM,i} - g_i \right)^2} \tag{63}$$

where N_{tp} represents the number of time points in the dataset, and g_i is the readout error-corrected baseline value at a given time point:

$$g_i = \underset{\varpi \in \{a_{bm,i}+\delta_{cl,i}, a_{bm,i}-\delta_{cl,i}\}}{\operatorname{argmin}} \left| a_{IPM,i} - \varpi \right| \tag{64}$$

MAPE is defined in an analogous way:

$$MAPE = \frac{1}{N_{tp}} \sum_{i=1}^{N_{tp}} \left| \frac{a_{IPM,i} - g_i}{g_i} \right| \tag{65}$$

For comparison purposes, a combined metric, referred to as the Loss function ($\mathcal{L}$), was introduced, incorporating the three metrics mentioned above. RMSE was included alongside MAE due to its sensitivity to outliers, while MAPE was added to account for relative errors, given that the proposed method covers a broad range of crack lengths. The Loss function is defined as [79]:

$$\begin{aligned} \mathcal{L} &= \frac{1}{3} MAE_{norm} + \frac{1}{3} RMSE_{norm} + \frac{1}{3} MAPE_{norm} \\ &= \frac{1}{3} \frac{MAE}{MAE_{IPMs}} + \frac{1}{3} \frac{RMSE}{RMSE_{IPMs}} + \frac{1}{3} \frac{MAPE}{MAPE_{IPMs}} \end{aligned} \tag{66}$$

where the subscript "norm" indicates that the metrics are normalized to their corresponding values obtained from the IPM applied to the static dataset (IPMs) using the parameter settings described in previous sections. The resulting metrics cover the entire static dataset unless specified otherwise.

4.4.2 DIC-Related Parameters

The parameters related to the image correlation aspect of the process, specifically l_{ve} and the size of the correlation subset, were evaluated. Fig. 31 shows the effect of varying l_{ve} from 1.5 to 2.5 mm on the normalized metrics ($\mathcal{L}, MAE_{norm}, RMSE_{norm}, MAPE_{norm}$). The trends indicate that increasing l_{ve} initially results in a rise in the number of outliers, as reflected by higher $RMSE_{norm}$ values compared to MAE_{norm}. This effect is evident up to $l_{ve} = 1.8\,mm$, beyond which overall accuracy decreases. This finding highlights l_{ve} as a highly influential parameter.

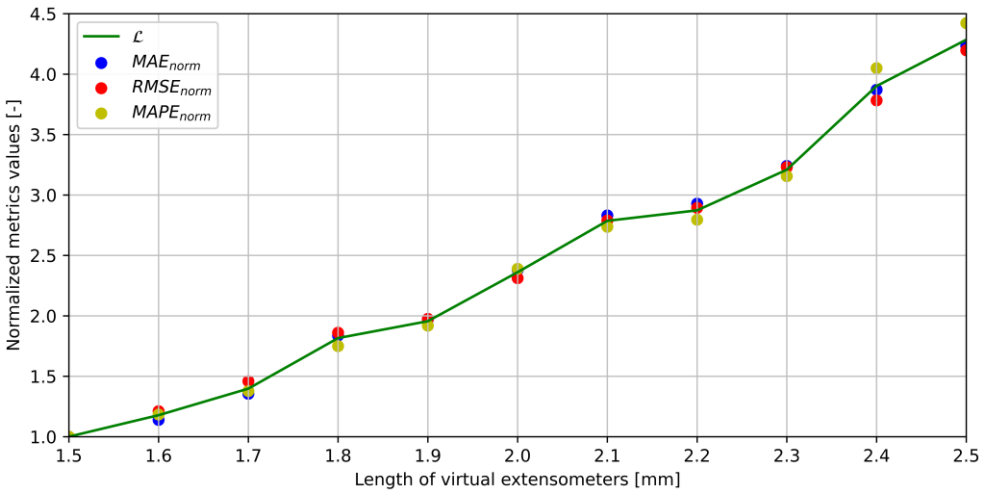

Fig. 31: Relationship between normalized metrics values and length of virtual extensometers (l_{ve}) for all static datasets [79]

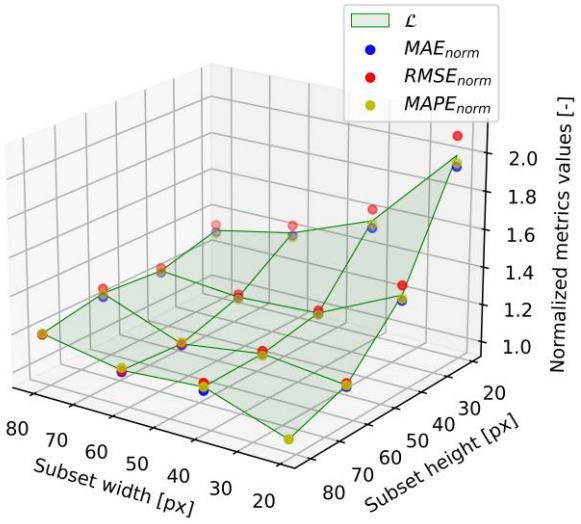

Fig. 32: Relationship between normalized metrics values and dimensions of the subset (w_{sub}, h_{sub}) *[79]*

The impact of the correlation subset size, particularly its width (w_{sub}) and height (h_{sub}), on the normalized metrics is illustrated in Fig. 32. The results show that extremely small subsets perform poorly due to an insufficient number of features captured. As the subset area grows, performance improves noticeably, especially with an increase in h_{sub} compared to w_{sub}. This suggests that a taller, narrower rectangular subset enhances IPM performance by improving spatial resolution in the direction of crack growth. Further increases in the subset area do not significantly affect performance, as the $\mathcal{L}$ values stay below 1.25, but further increases raise computational time. Thus, the selected subset dimensions of $(w_{sub,f}, h_{sub,f}) = (21, 81)\, px$, as described in subsection 4.4.2, provide a good balance between accuracy and computational efficiency.

4.4.3 IPM-Related Parameters

The influence of the parameters introduced in the IPM algorithm was then examined. First, the effect of *n* and *m*, which are crucial for reducing computation time, was evaluated. Fig. 33 shows how these parameters affect the results of the proposed method. The method exhibits low sensitivity within the chosen parameter intervals, as $\mathcal{L}$ remains below 1.3, except when $m < 5$, where results decline sharply due to GPR overfitting. A slight deterioration in results is observed for parameter *n* above 10, attributed to an increase in the number of outliers caused by excessive data decimation. A similar effect is observed when *m* is increased beyond 7.

Next, the influence of F_{dd} along with n_s was investigated. For this analysis, the lower bound of ℓ used in P3 was derived utilizing the following generalization of equation (61) [79]:

$$\ell_{l,k,i}^{P3} = \ell_{opt,i}^{P1} + \frac{k(\ell_{opt,i}^{P1} - \ell_{opt,i}^{P2})}{n_s}, k = 1{:}\, n_s, n_s \in \mathbb{N} \tag{67}$$

Condition 2 was checked after each smoothing iteration to prevent additional smoothing if it was already satisfied. The tested interval also included $n_s = 0$, meaning that P3 did not run at all in this case. The results, presented in Fig. 34, indicate that n_s has minimal impact on the results when smoothing is applied in the IPM. Without smoothing $(n_s = 0)$, the number of outliers slightly increased, particularly for longer cracks.

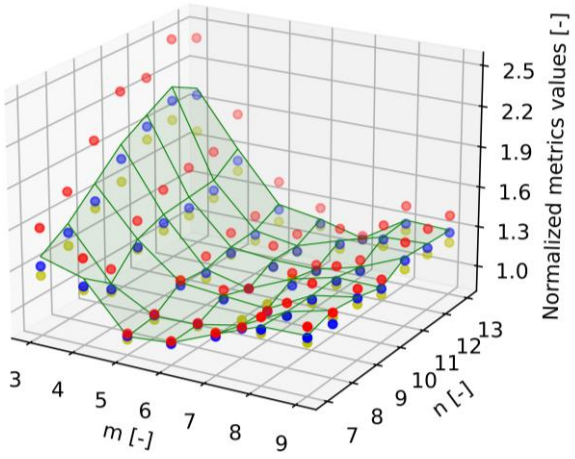

Fig. 33: Relationship between normalized metrics and the global and local data decimation levels (n, m) [79]

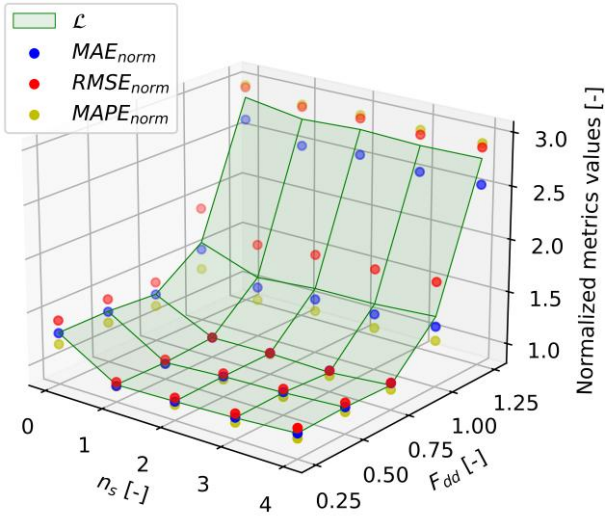

Fig. 34: Relationship between normalized metrics and the number of smoothings and derivative distinction factor (n_s, F_{dd}) [79]

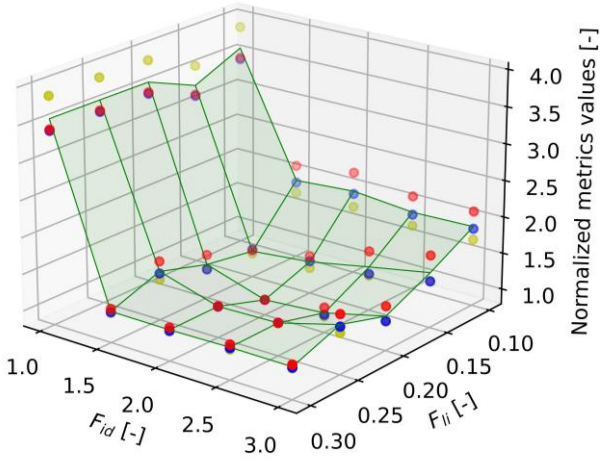

Fig. 35: Relationship between normalized metrics and the interval decrement factor and localization interval factor (F_{id}, F_{li}) [79]

Higher F_{dd} values, which prioritize phase P1 over P2, significantly raised the number of outliers. This effect was first observed in longer cracks, as indicated by a noticeable increase in RMSE values

compared to the other metrics, and eventually affected shorter cracks as well, reflected by comparably high values of RMSE and MAPE, both exceeding those of the other metrics.

Finally, the impact of F_{li} and F_{id}, which determine the length of $\mathcal{J}$ used for GPR in phases P2 and P3, was evaluated. Fig. 12 (right) shows that the method is nearly unaffected by changes in F_{id} between 1.5 and 3. However, when $F_{id} = 1$, which means that repeating P2 and P3 with a reduced GPR interval is not permitted, a noticeable decline in results occurs, particularly for short cracks. Likewise, a low value of F_{li} leads to poorer results due to an increase in the number of outliers, indicating that the localization interval becomes too short. No significant effect is observed within the rest of the tested range.

4.4.4 Load Level Dependence

To further evaluate the impact of the LL, in addition to the measures described in subsection 4.1.4, a supplementary procedure was included in the test of the EN AW-7075 No. 2 sample. During several readings, the static load was gradually increased in five consecutive steps up to 5 kN, as shown in Fig. 36. This approach created four sets of load dependencies at constant crack lengths. In these cases, the specified 33% static overload was intentionally exceeded to test the method's performance over a wider range of loads.

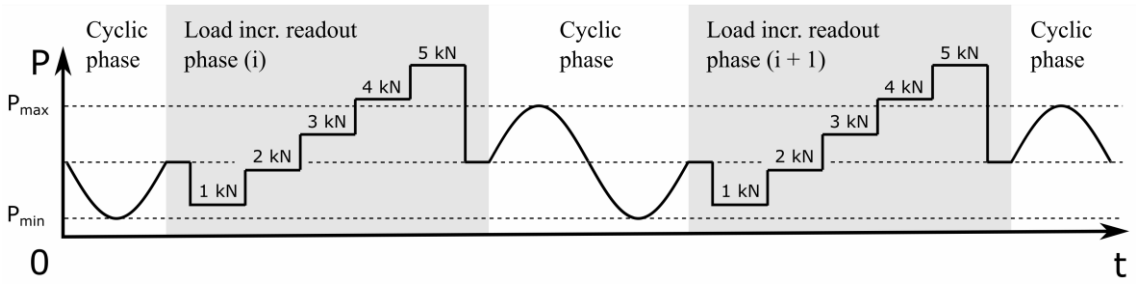

Fig. 36: Schematic illustration of the load increase during the load increment readout phases for the aluminum alloy No. 2 sample [79]

It was observed that, while the IPM results do show some dependence on the LL, this dependence is much less pronounced than that of the STM, as illustrated in Fig. 37. For example, at a crack length of 5.5 mm and an LL of 1 kN, the STM estimates no crack, whereas the IPM provides a value of 5.28 mm. This demonstrates the significantly greater robustness and versatility of the proposed method.

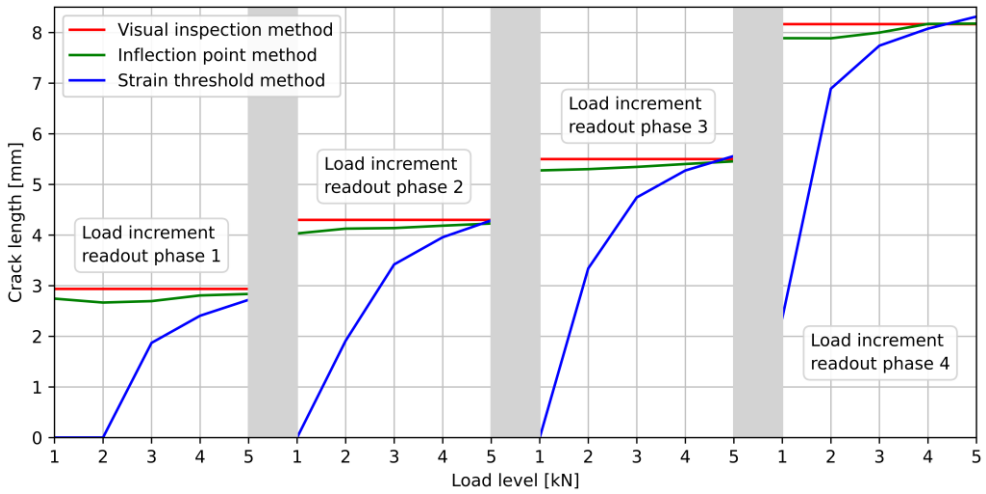

Fig. 37: Results of the methods comparison in terms of load dependency for the four different load increment readout phases during the aluminum alloy No. 2 sample testing [79]

4.5 Results – Validation and Comparison

The results in the method comparison presented in this chapter are expressed as deviations from the baseline crack lengths ($\Gamma_{bm,i}$, $\Gamma_{IPMs,i}$, $\Gamma_{IPMd,i}$, $\Gamma_{STM,i}$) as a function of the baseline crack length a_{bm} for each CT sample. These deviations correspond to the results obtained from the VIM, the IPMs, the IPM applied to the dynamic dataset (IPMd), and the STM applied to the static dataset, respectively. The values are defined as [79]:

$$\Gamma_{j,i} = a_{j,i} - a_{bm,i};\ j \in \{bm, IPMs, IPMd, STM\} \tag{68}$$

Additionally, the band $\pm\delta_{cl,i}$ is plotted along with the $\Gamma_{bm,i}$ values. For VIM, the index i is reused only for comparability since the VIM and IPM datasets are aligned one-to-one in count and order.

This plotting technique highlights the differences in results between the methods, which would be less apparent if the crack lengths were plotted directly on the y-axis. Regarding the x-axis, using the number of cycles would result in uneven point distribution, as there are more cycles between readouts for shorter cracks than for longer ones. Instead, by using the baseline crack length, the points are more evenly spaced, providing a clearer representation.

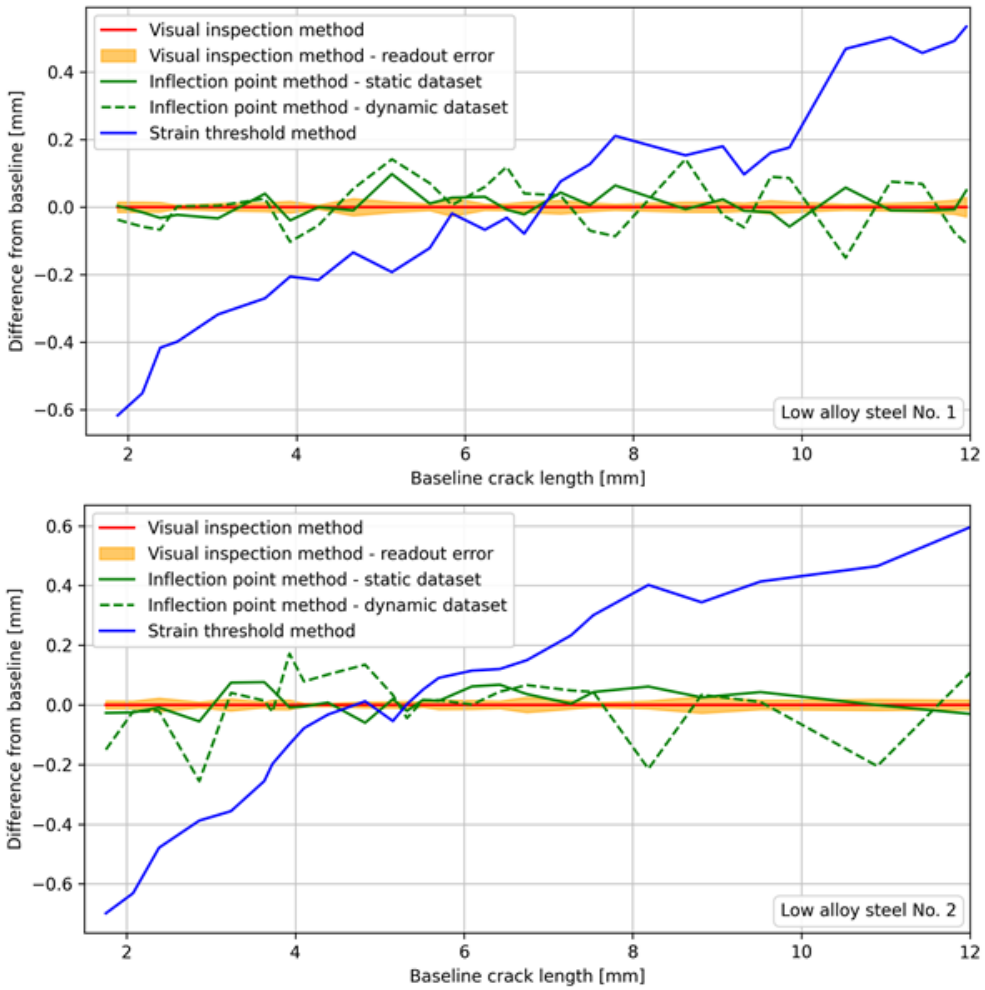

Fig. 38: Methods comparison in terms of their differences from the baseline as a function of baseline crack length for the low-alloy steel sample No.1 (top) and No.2 (bottom) [79]

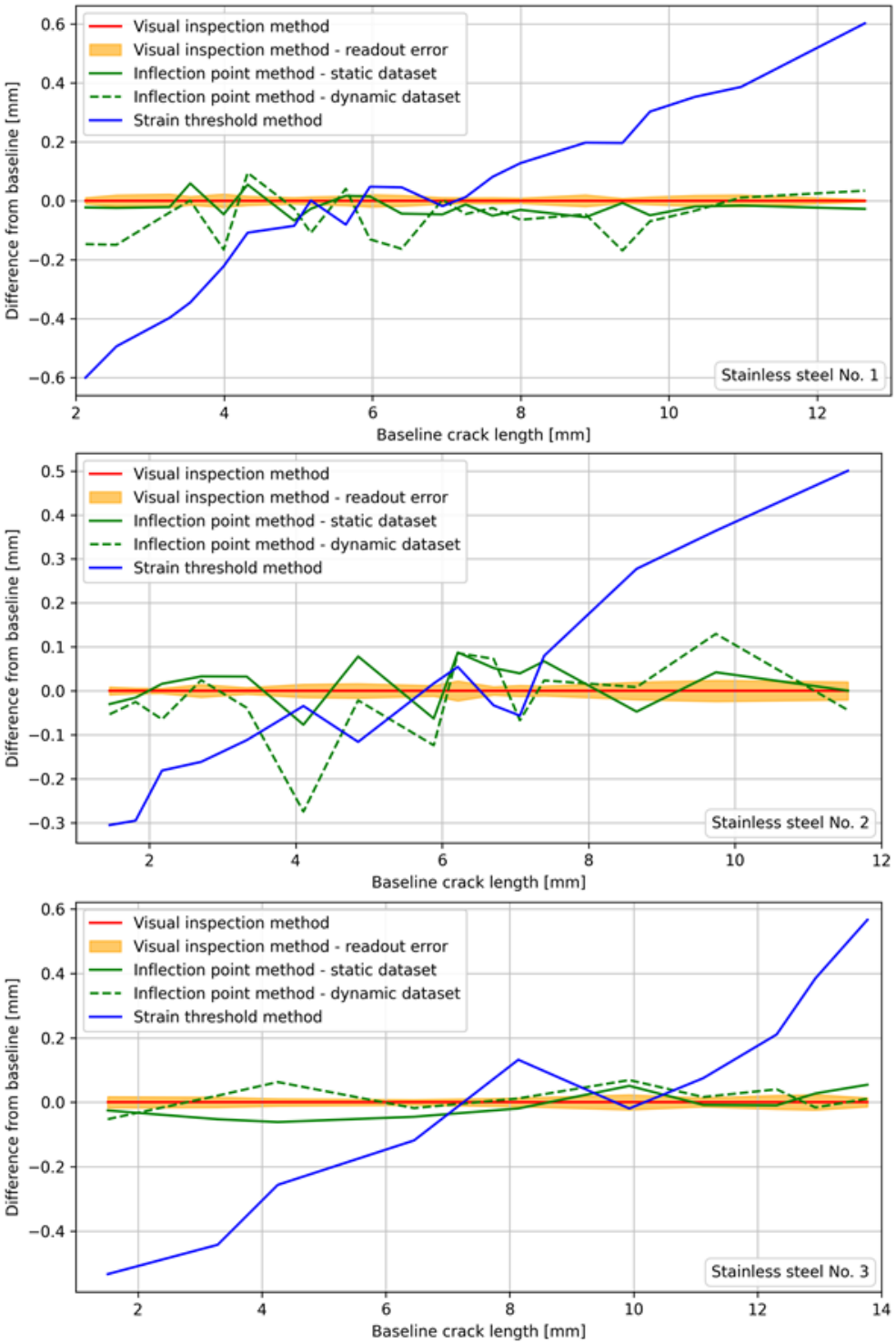

Fig. 39: Methods comparison in terms of their differences from the baseline as a function of baseline crack length for the stainless-steel sample No.1, No.2 and No.3 [79]

Fig. 38, Fig. 39 and Fig. 40 present a comparison of the methods for specific material groups: low-alloy steel, stainless steel, and aluminum alloy, respectively. In each of these figures, the most prominent are the curves for STM, which exhibit an approximately linear trend in deviation from the correct values. This reflects the crack length dependence of the STM results, which has been mentioned in subsection 4.2.3.

In contrast, the results of the proposed method do not systematically deviate from the baseline but

instead fluctuate around it. When the IPM is applied to the dynamic dataset, a higher number of outliers is observed; however, the overall results are still considered correct. This increase in outliers is also evident from the higher RMSE to MAE ratio (1.43) compared to the ratio calculated for the static dataset (1.29). These ratios were calculated from the RMSE and MAE values presented in Tab. 6, which summarizes the overall results of the different methods used in this study and highlights the key performance metrics.

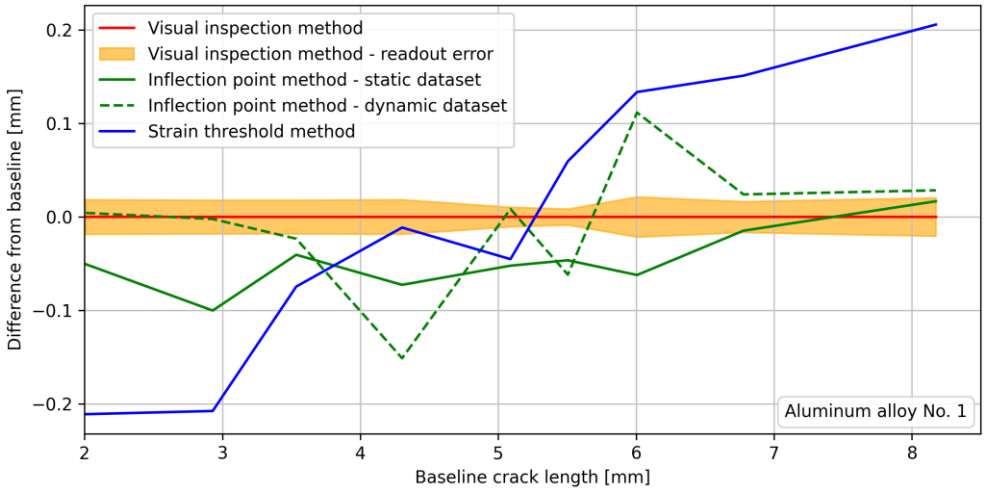

Fig. 40: Methods comparison in terms of their differences from the baseline as a function of baseline crack length for the aluminum alloy sample No.2 [79]

Regarding relative errors, they decrease with increasing crack length for the IPM. In contrast, this is not the case for the STM, where the absolute error grows as the crack length increases. Depending on how quickly the absolute error rises compared to the crack length, the relative error for STM, at best, decreases more slowly than for IPM, but in some cases also remains unchanged or even increases. In summary, the IPM yields results that closely match the baseline for both static and dynamic datasets, although its accuracy is about 2.3 times lower for the dynamic dataset than for the static one. In comparison, the accuracy of the STM for the static dataset is approximately 10.8 times worse than that of the IPM. Concerning the IPM's dependence on the chosen material and sample thickness, no notable qualitative or quantitative differences were observed in the results.

Tab. 6: Summary of overall results for particular methods [79]

	MAE^a $[\mu m]$	$RMSE^b$ $[\mu m]$	$MAPE^c$ [%]	$\mathcal{L}^d$ [-]
IPMs[e]	24	31	0.50	1.0
IPMd[f]	54	77	1.15	2.3
STM[g]	215	274	5.43	10.8

[a] mean absolute error; [b] root mean square error; [c] mean absolute percentage error; [d] loss function; [e] static dataset evaluated by Inflection point method (IPM); [f] dynamic dataset evaluated by IPM; [g] static dataset evaluated by Strain threshold method

4.6 Discussion and Recommendations

The IPM and the inflection point principle were successfully validated on a static dataset, as their results align reasonably well with the baseline. Furthermore, the practicality of measuring and implementing

the proposed method in a real-time experiment (dynamic dataset) was effectively shown. While the method demonstrates lower accuracy with the dynamic dataset, the outcomes are still valid.

The IPM has demonstrated robustness and adaptability concerning test variables, especially with changes in LLs. This is significant because adjusting LLs is a customary practice in standard tests to determine FCGR for different SIF values. The strength of the IPM becomes even more apparent when compared to the STM, as evidenced not only by the presented sensitivity analysis but also by the range of ε_{th} values (Tab. 5) utilized in the methods comparison.

No dependence was detected concerning different materials or sample thicknesses. It is reasonable to expect that the method will perform consistently across various metallic materials, sample sizes, or even sample types, as it utilizes a regression technique that can adapt to the specific characteristics of the data in each experiment. This adaptability is due to its continuous learning throughout the test, allowing adjustment to factors such as noise levels or the nature of the CODP curve near the inflection point without requiring user intervention.

At present, the IPM is recommended only for metallic materials, since the inflection point principle has not yet been validated for other materials such as composites or plastics—an area proposed for future research. The method's extensibility to another sample type is further demonstrated in Chapter 6, where tests on MT (middle tension) samples are presented.

Concerning the parameters associated with the DIC setup, the l_{ve} has a significant impact on the IPM results. The current findings indicate that shorter lengths are more favorable, though lengths smaller than 1.5 mm could not be tested due to the constraints of the validation experiment. Nonetheless, smaller values may potentially enhance the method's accuracy, provided that the propagating crack remains outside the areas covered by the correlation subsets for the entire duration of the experiment. This assumption is examined in the subsequent chapters.

The exact values of the subset size $(w_{sub,r}, h_{sub,r})$[24] will depend on the size and density of the speckles in the image, which are influenced by factors such as camera resolution, m_{opt}, and—most importantly—how the speckle pattern is applied to the specimen. It is therefore advisable to follow the general guidelines for subset selection described in subsection 4.2.2. However, as a practical recommendation, the smaller subset dimension should be oriented along the direction of crack propagation, while the larger dimension should be perpendicular to it. Maintaining an aspect ratio of approximately 4:1 (perpendicular:parallel) is suggested, as this configuration proved most effective during the development of the IPM.

The parameters directly related to the IPM were consistently chosen to balance the method's accuracy with computational time. Based on the sensitivity analysis of *n* and *m*, the final values are set to $n_f = 2$ and $m_f = 1$, which is why the value of the n_{ve} must be even. This configuration is equivalent to using $(n_d, m_d) = (10, 5)$ with $n_{ve,d} = 1000$, a combination that demonstrates very good results. To exactly match the development and testing condition, n_{ve} would need to be 200. However, this is not strictly necessary, as the sensitivity analysis shows that the IPM performs well across a range of (n_d, m_d) values.

[24] where the subscript *r* denotes the recommended value for users of IPM. The same convention applies to other parameters below.

Based on these findings, the following recommended intervals were formulated [79]:

$$w_{ve,r} \in \langle w_{ve,l,r}, w_{ve,u,r} \rangle = \langle 10.0, 14.5 \rangle \, mm \tag{69}$$

$$f_{ve,r} \in \langle f_{ve,l,r}, f_{ve,u,r} \rangle = \langle 11, 14 \rangle \, mm^{-1} \tag{70}$$

where f_{ve} represents the spatial frequency of VE. Then, the recommended number of VEs inside the CODP window ($w_{ve,r}$) is:

$$n_{ve,r} = w_{ve,r} f_{ve,r} \tag{71}$$

The upper bound $w_{ve,u,r}$ was set according to the value used during development and testing. The upper bound $f_{ve,u,r}$ was then selected so that multiplying it by $w_{ve,u,r}$ yields the number of points entering the GPR equivalent to the scenario in the sensitivity analysis where $n = 7$.

For the setting of lower bounds ($f_{ve,l,r}$ and $w_{ve,l,r}$), the case from sensitivity analysis where $n = 13$ was considered, resulting in $n_{ve,r} = 150$. Therefore, the only constraint for the lower bounds is that their product equals 150. The final selection was made to balance the width of the $w_{ve,r}$ interval with allowing for the use of a smaller number of VEs, potentially reducing computational time.

Additionally, the choice of these lower bounds was verified against the minimum number of points (VE) that would enter the Second P2/P3 using the final values, which is 30, calculated as:

$$\frac{2F_{li,f}}{F_{id,f}} \frac{w_{ve} f_{ve}}{m_f} \tag{72}$$

The worst-case scenario from the sensitivity analysis of F_{id} and F_{li} is $(F_{id}, F_{li}) = (3, 0.15)$, meaning the Second P2/P3 would be performed on 17 points:

$$\frac{2F_{li}}{F_{id}} \frac{n_{ve,d}}{m_d} \tag{73}$$

This provides a sufficient margin when using n_{ve} derived from any combination of values within the recommended intervals for $w_{ve,r}$ and $f_{ve,r}$. Moreover, it ensures that the user's settings remain aligned with those used during development and testing, while also allowing flexibility in the selection of TLs and machine vision cameras.

The applicability limits for real-time measurements were tested using $n_{ve} = 200$, corresponding to the $w_{ve,u,r}$ and a value close to the $f_{ve,l,r}$. This configuration resulted in $34 \, ms$ for image data extraction (DIC)[25] and $88 \, ms$ for the IPM computations[26]. Hardware operations, such as chip exposure and data reading, take about $15 \, ms$. Given that hardware operations and DIC for the current frame can run concurrently with IPM calculations for the previous frame (further referred to as the *processing sequence)*, this enables an acquisition speed up to $11.9 \, FPS$. With a sample loading frequency of $60 -$

[25] using parallelized computation on four cores of an AMD Ryzen 9 5950X at 4.2 GHz (chosen because such core counts are common on lab computers).
[26] utilizing serial computation on one core at 4.2 GHz; timing was measured with deterministic (i.e., non-random) initialization of GPR hyperparameters for the first image.

$90\ Hz$, this allows the processing of every 5th to 8th load cycle. Potential improvements in the computational time of the IPM, which currently constitutes the main bottleneck of the process, will be explored in Chapter 5.

For a hardware-matched comparison, an identical total pre-processing time of $49\ ms$ was assumed ($34\ ms$ data extraction + $15\ ms$ hardware operations). The computation needed to determine the crack length with STM takes just $1.4\ ms$. Following the same processing sequence as used for the IPM, this enables frame rates up to $20.4\ FPS$, making it possible to analyze every third to fifth load cycle at the sample loading frequencies discussed in subsection 4.1.3. This means that, overall, the process of crack length assessment is nearly twice as fast when using STM compared to the original software implementation of the IPM (before any code optimizations).

The speed comparison shown in Tab. 7 can be further supplemented by an estimated time for full-field DIC, assuming the same hardware conditions. If a region measuring $1.5\ mm \times 14.5\ mm$ (the same as used for IPM and STM) is covered by a uniform mesh of equilateral triangles, where each side equals the distance between neighboring VEs, the estimated time to perform DIC for data extraction is roughly $550\ ms$. With the same $15\ ms$ hardware operation time, the resulting maximum frame rate is about $1.8\ FPS$. The additional time required to extract crack length from the data will depend on the specific method selected by the user.

Tab. 7: Processing times and maximum frame rate overview for IPM (Inflection point method), STM (Strain threshold method), and full-field DIC [79]

	IPM	STM	Full-field DIC
Hardware operations [ms]	15	15	15
Data extraction from image (DIC) [ms]	34	34	550
Crack length evaluation [ms]	84	1.4	N/A
Max. achievable frame rate[a] [s^{-1}]	**11.9**	**20.4**	**1.8[b]**

[a] Considering the *processing sequence* described in the text (section 4.6), the frame rate is calculated as *1000 ms / max(Hardware operations + Data extraction from image (DIC), Crack length evaluation); unit is equivalent to FPS;*

[b] Assuming that *crack length evaluation < (Hardware operations + Data extraction from image (DIC))*

Also, certain challenges and limitations were identified. For crack lengths smaller than 1.5 mm, the IPM did not provide accurate results due to the low values of measured displacements influenced by noise in DIC, and the impact of higher forces present during crack initiation on the area around the notch tip. Using IPM is not recommended for cracks longer than $(w_{ve} - 0.5)\ mm$, as the method requires the presence of data on both sides of the inflection point.

5 Improving IPM Computational Efficiency

As previously mentioned (section 4.6), the primary bottleneck in implementing the IPM for real-time applications is its computational demand. Therefore, this chapter is dedicated to improving the computational efficiency of the IPM, with the goal of reducing calculation time without compromising the quality of the results obtained.

Initially, optimization efforts focused on the code itself, exploring opportunities for parallelization of certain computational steps, as well as eliminating redundancies and repeated calculations of variables. Next, the optimization was directed towards the process scheme of the method itself.

It should be noted that IPM was implemented in the Python programming language. Although it was previously mentioned that the GPR utilizes the scikit-learn library—a Python library—this is the first time the programming language itself is explicitly stated.

5.1 Code-Level Optimization

5.1.1 Profiling and Parallelization

Initially, basic elimination of redundancies and repeated calculations was implemented in the __main__[27] part of the IPM code, but the impact on reducing computational time was negligible.

Consequently, to gain a deeper understanding of the time consumption of various functions, the cProfile library was used to analyze the execution times of various parts of the code. The profiling results revealed that the most time-consuming component of the calculation kernel is the GPR regression itself. However, since the GPR regression utilizes an optimized implementation from the scikit-learn library, it was not the primary target for code-level optimization in this chapter—although an attempt at parallelization was introduced. The main efforts related to the GPR regression are discussed in the following section (5.2), with a focus on reducing the number of instances where the GPR regression is performed.

Findings from the execution time analyses, along with other significant time-consuming operations and the various cases tested to improve computational efficiency, are summarized in Tab. 8 and Tab. 9. The times presented for particular functions represent the cumulative time—that is, they include not only the time spent within the function itself, but also all the time spent on any sub-functions it calls, directly or indirectly.

Case 1 corresponds to the final version of the IPM described in Chapter 4 and serves as the baseline for both accuracy and time consumption. For consistency, all timing measurements were performed without random initialization of the GPR hyperparameters for the first image, to eliminate randomness from the time calculation results, and using the same processor.

Efforts were then focused on reducing the time required for calculating the GPR derivatives. The approach in Case 2 (Tab. 8) involved parallelizing the computation of the first and second derivatives so that each would be performed simultaneously on separate cores. However, this did not reduce the overall calculation time. The overhead associated with creating and managing separate threads, as well

[27] which is the block executed when a script is run directly but not when it is imported into another script, e.g., to reuse its functions.

as the need for synchronization, outweighed any potential benefits gained from parallel execution.

Tab. 8: The most time-consuming operations for various cases together with the average time consumption per processed image, where text highlighted in red represents a worsening in absolute values compared to the baseline. Each case is considered separately, with changes always implemented into the baseline code.

Cases:	1: From the Chapter 4 (baseline)	2: Parallelized GPR[a] deriv. (2 cores)	3: GPR[a] P2 and P3[b] in parallel (2 cores)
Function	Time per image = 88 ms operation [%]	Time per image = 90 ms operation [%]	Time per image = 113 ms operation [%]
GPR[a] regression	86.5	84.1	89.2
GPR[a] derivatives	5.3	7.2	3.9
GPR[a] values extraction	4.1	4.0	3.1

[a] Gaussian process regression; [b] phase 2 and phase 3 of the Inflection point method

Independently of the changes made in Cases 2, a significant refactoring of the code was also performed to parallelize the computation of the GPR regression for both P2 and P3 phases. Parallelization was not extended to P1, as both P2 and P3 require outputs from P1. This modification is presented as Case 3 in Tab. 8, where a substantial increase in computational time per image is observed—specifically, a 28% increase.

5.1.2 Derivative & Extraction Optimizations

After the unsuccessful parallelization attempt, the computation was reverted to a serial approach. Instead of calculating the first and second derivatives separately, the code was refactored to compute both within a single function, reusing common terms present in both calculations. Additionally, the number of cases requiring second derivative computation was reduced, as the second derivative is not needed in Phase 1 of the IPM and was therefore omitted in that phase. This is presented as Case 4 in Tab. 9. These changes resulted in a 40% reduction in the time required for GPR derivative calculations and decreased the total time needed to perform the IPM on a single image on average by $2\ ms$.

Attention was also directed to the function responsible for extracting values from the GPR at specific points, while retaining the previous optimizations that reduced computation time. This function operates by taking the starting and ending coordinates of the interval used for GPR regression in a given phase of the IPM. Between these endpoints, N_e points (further referred to as *Number of extraction points*) are distributed evenly, and the GPR model is used to predict values at each of these points. Thus, $CODP_{P(1/2/3)}(x)$ is created. These CODP curve reconstructions are subsequently used to compute derivatives and to determine the inflection point, effectively defining the granularity of the x-coordinate that can be assigned to the inflection point. In the version of IPM presented in Chapter 4, $N_e = 1000$ points are used.

An investigation carried out on the static dataset determined whether such a high number of extraction points was necessary. The results, presented in Fig. 41, suggest that reducing the number of extraction

points down to $N_e = 400$ does not significantly affect the accuracy of the method, while computational cost decreases linearly with N_e. To provide a safety margin, the value of $N_{e,f} = 500$ was selected for use in the IPM algorithm.

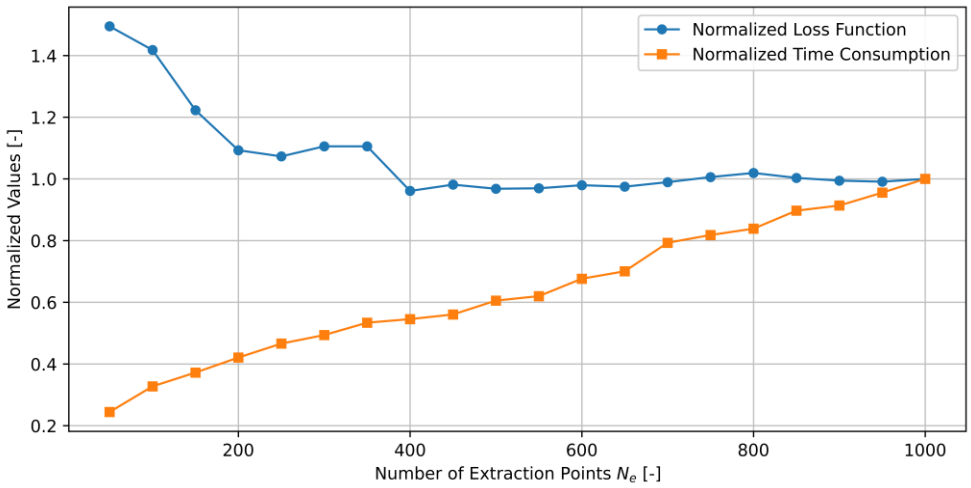

Fig. 41: Influence of the number of extraction points N_e on IPM (Inflection point method) accuracy (Loss function) and computational time of the (GPR (Gaussian process regression) derivatives + GPR values extraction) for static dataset

This change was implemented in Case 4 and is presented in Tab. 9 as Case 5, where it proved to reduce the time required for both GPR value extraction and GPR derivative calculations. The optimization resulted in an additional improvement of 3 ms per image compared to Case 4 and 5 ms compared to the baseline (a 5.7% relative improvement), which is not negligible.

Tab. 9: The most time-consuming operations for various cases with the average time consumption per processed image, where text highlighted in green represents an improvement compared to the baseline. The cases are treated consecutively, with each subsequent case incorporating all the improvements from the preceding case.

Cases:	1: From the Chapter 4 (baseline)	4: Optim. and reduced deriv. calc.	5: Reduction of the extraction points
Function/operation	Time per image = 88 ms operation [%]	Time per image = 86 ms operation [%]	Time per image = 83 ms operation [%]
GPR[a] regression	86.5	88.4	90.4
GPR[a] derivatives	5.3	3.2	1.8
GPR[a] values extraction	4.1	4.2	2.9

[a] Gaussian process regression

5.2 Processing Scheme Optimization

As shown in the previous section (5.1), the most time-consuming operation is the GPR regression, whose computational cost increases with the number of input points. Therefore, the aim of this chapter is to modify—or, in other words, optimize—the process scheme of the IPM in order to achieve the greatest

possible reduction in these operations while minimizing any negative impact on the accuracy of the proposed method.

5.2.1 Motivation and Overview

The key assumption behind this optimization is that the crack propagates gradually and relatively slowly in the context of acquisition speed, so there is no significant change between two consecutive images. To support this approach, data from the measurements described in the subsequent chapter were used, as these specifically involved the continuous recording of crack growth.

This version of the IPM, referred to here as "fast IPM" (fIPM), is illustrated in the flowchart shown in Fig. 43 at the end of this chapter. This flowchart builds upon that of the previous IPM version (Fig. 30), which is referenced in the following text simply as IPM. Like its predecessor, it shows the flow of key values, the sequence of processes, and relevant decision-making conditions.

The most significant change is the substantial reduction in the use of Phase 1 (P1). P1 previously involved the largest number of points in the GPR regression and thus contributed most to slowing down the process. Nevertheless, P1 still plays a vital role, as will become clear from the following description.

5.2.2 Workflow Outline

At the start of the fIPM, the first CODP curve ($i = 0$) still follows the same path as in the IPM. However, instead of producing the final crack length $a_{IPM,i}$ (here replaced by $a_{fIPM,i}$) directly, the result is now considered a preliminary crack length $a_{P,i}$. For the following n_{CODP} cases, P1 is skipped, and the algorithm continues directly to Phases 2 and 3, taking the initial guess for the hyperparameters from the storage variable **OH**. This variable is updated with the optimal hyperparameters from the P2 optimization in First P2/P3 step as soon as $a_{fIPM,i}$ is obtained, provided updating is permitted (ie., when the "update initial guess" flag is set to "yes", as shown in Fig. 43 as *update initial guess = yes*, which will be used as reference hereafter).

In these steps, $x_{ip1,i}$ is also required as input to equation (56), which defines the interval from the CODP curve used in the GPR localization. In the IPM, $x_{ip1,i}$ always originated from the GPR regression in P1. However, when P1 is skipped, $x_{ip1,i}$ is taken from the storage variable $x_{ip1,inp}$, which is updated with $a_{fIPM,i}$ as soon as it is obtained, provided that updating is permitted (ie., when the "update values" flag is set to "yes", as shown in Fig. 43 as *update values = yes*, which will be used as reference hereafter).

Serving as a correction mechanism, this phase must be retained at regular intervals. Specifically, at a frequency set by the parameter n_{CODP}, it interrupts the hyperparameter propagation cycle within P2 and P3 and proactively resets the input parameters for the next n_{CODP} cycles. Formally, P1 is not skipped when:

$$i \bmod n_{CODP} = 0 \tag{74}$$

5.2.3 Phase Scheduling & decision Logic

P1 is also performed if Condition 2 determines that the result from P1 ($x_{ip1,i}$) should be used but has not yet been calculated. For this, the second component of Condition 2, expressed by equation (60), was modified to make results from P2 or P3 even more favorable compared to those of P1:

$$0.5\ \frac{dCODP_{P1,i}}{dx}\left(x_{ip1,i}\right) > \left[\frac{dCODP_{P2,i}}{dx}\left(x_{ip2,i}\right)\ or\ \frac{dCODP_{P3,i}}{dx}\left(x_{ip3,i}\right)\right] \tag{75}$$

This adjustment was intended to limit the time-consuming P1 phase, which appeared more often in Chapter 6 than in Chapter 4, thus slowing down the algorithm. After implementing this change, small shifts in predicted crack length values were observed, but these were less significant than the overall oscillation (noise) in the crack length curve, which was mainly due to the accuracy of the synchronization device triggering the image acquisition during the phase of the loading cycle when the crack is most widely open. Furthermore, when evaluating the results in terms of FCGR, the impact of this change was negligible.

Finally, to account for sudden changes in the CODP curve (for example, due to unexpected external influences or occasional delays of the synchronization device), an additional Condition 3—referred to as "large difference" in Fig. 43—was introduced. This condition is also based on the fundamental assumption underlying the processing scheme optimization described in this chapter.

Specifically, a large difference is detected—and thus Condition 3 is met—if:

$$\left|a_{P,i} - a_C\right| > \ \mathrm{STD}_{crit} \wedge\ i > n_{adapt} \tag{76}$$

where a_C ("crack length criterion" in Fig. 43), is overwritten (updated) every permitted iteration in which (*update values = yes*), based on a linear regression performed on the last $n_{adapt} = 30$ data points. The regression model is given by:

$$a_{fIPM,j} = a_{reg} N_j + b_{reg} \tag{77}$$

where a_{reg} and b_{reg} are the regression coefficients determined by least-squares fit to the following values:

$$\left(a_{fIPM,j}, N_j\right), j \in \left\{i - n_{adapt} + 1, \dots, i\right\} \tag{78}$$

The crack length criterion is then calculated as:

$$a_C = a_{reg} N_i + b_{reg} \tag{79}$$

The threshold STD_{crit} ("STD criterion" in Fig. 43) is defined in equation (81) as three times the standard deviation of the crack length differences $d_{CL,j}$, calculated for the last $n_{adapt} = 30$ updates of crack length storage $a_{S,k}$ as follows:

$$d_{CL,j} = a_{S,k} - a_{S,k-1}, \text{ for } k \in \left\{J - n_{adapt}, \dots, J\right\} \text{ and } j = k - (J - n_{adapt}) \tag{80}$$

where the $a_{S,k}$ is updated by appending the new value of $a_{fIPM,i}$ as soon as it is obtained, provided updating is permitted (*update values = yes*), and J is the index of the last updated value of $a_{S,k}$.

The STD criterion is given by:

$$\mathrm{STD}_{crit} = 3\sqrt{\frac{1}{N-1}\sum_{j=0}^{N}\left(d_{CL,j} - \overline{d_{CL}}\right)^2} \tag{81}$$

Condition 3 is first applied when the current iteration reaches $i = 31$, ensuring that there are enough data points to calculate a meaningful value of STD_{crit}, which reflects the behavior (noise) of the resulting crack length curve and is used for evaluating outliers. Until this point, Condition 3 is not used; instead, the preliminary crack length is simply declared as the final crack length ($a_{fIPM,i} = a_{P,i}$). If this is not the last input from the DIC evaluation providing the CODP curves, the algorithm proceeds to the next iteration ($i + 1$), keeping both the *update initial guess* and *update values* flags set to *yes*, which is their default state at the start of the algorithm.

5.2.4 Robustness & Outlier Handling

Once Condition 3 is active**,** it checks for outliers in the CLIs by comparing the current increment to the previous $n_{adapt} = 30$ increments. The window size of 30 was chosen to keep this interval short, giving the STD criterion an adaptive nature. This allows it to accommodate the increasing FCGR as the crack length increases, which results in larger CLIs between individual measurement points. The adaptive STD criterion is illustrated in Fig. 42, which visualizes its values as lower and upper bounds around the resulting crack length values from fIPM.

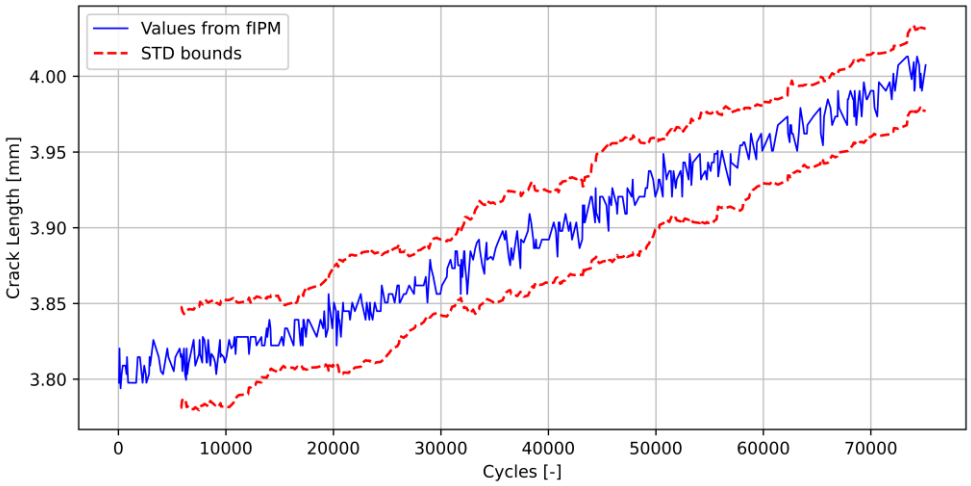

Fig. 42: Visualization of the STD criterion values as lower and upper bounds around the resulting crack length values $\boldsymbol{a_{fIPM}}$ *from fIPM (fast Inflection point method). The data shown correspond to dataset No.3 of the MT No.2 sample prior to adding the notch length. Virtual extensometers' length* $l_{ve} = 1.5\ mm$

If Condition 3 is satisfied (that is, an outlier is detected**),** the algorithm initiates corrective actions. It first checks whether P1 has been performed in the current iteration. If not, the algorithm returns to the beginning and recalculates the entire sequence for this iteration, including the GPR global (P1), which analyzes the entire CODP curve. This also resets the localization region for the GPR and updates the initial hyperparameter guess. After reaching $a_{P,i}$, Condition 3 is re-evaluated. If the condition is no longer met, the outlier has been corrected. This indicates that either the local optimization in P2 or P3 skipped to a different local minimum, or that a minor disturbance (such as synchronization inaccuracy) did not significantly disrupt the algorithm's robustness. With this implementation, it is no longer necessary to perform P1 as frequently and the $n_{CODP} = 100$ was tested to be sufficient, which helps

improve computational efficiency.

If the value remains an outlier, the algorithm checks again whether P1 has already been calculated in this iteration. If so, it further checks whether there have been five consecutive outliers. If this is not the case, both the *update values* and *update initial guess* flags are set to value *no* to prevent propagation of outlier values to the input variables (including initial guesses stored in OH, the STD criterion, crack length criterion, and the value of $x_{ip1,inp}$ used in P2 and P3 when P1 has not been performed).

At the same time, the final crack length $a_{IPM,i}$ is set equal $a_{P,i}$, which has just been updated from the preliminary crack length storage variable $a_{P,inp}$. The preliminary crack length storage variable is updated with $a_{fIPM,i}$ as soon as it is obtained, provided updating is permitted (*update values = yes*).

In other words, the final crack length for the current iteration will match the last accepted value from an iteration where no outlier was detected. This is consistent with the fundamental assumption that the crack length does not change significantly between consecutive iterations.

The *update values* flag is then reset to *yes* immediately before the next fIPM iteration begins. The *update initial guess* flag is reset the next time Condition 3 is not met (meaning, when no outlier is detected).

If the algorithm detects five consecutive outliers even after following the calculation path that includes P1, the user is notified with a warning indicating the number of cycles when this occurred. The final crack length is then updated using the last preliminary crack length that was evaluated as an outlier, and all storage and input variables are updated as previously described. This action effectively resets the algorithm and forces it to accept these previously flagged outlier values as correct. This serves as a safeguard to prevent the algorithm from entering an infinite loop, in which new values are repeatedly rejected, and the crack length fails to update. Such abrupt changes in FCGR can occur, for example, when the crack overcomes a microstructural barrier or interacts with an inclusion, pore, or other microstructural feature [89]. These events are well-known phenomena, and to avoid misclassifying them as outliers—which are intended to capture only non-material-related anomalies—the algorithm is designed to accept them after several failed correction attempts.

5.2.5 Benchmarking & Results

When evaluating the effects of processing scheme optimization on computation time, it became necessary to establish a new baseline. This was because a different dataset was used, which differed slightly in character from those in Chapter 4 and section 5.1. Specifically, the new data consisted of continuous, uninterrupted crack growth measurements for all datasets acquired from the MT No. 2 sample, which will be described in detail in Chapter 6.

For the new baseline (Case 6 in Tab. 10), P1 was performed in each iteration by setting the $n_{CODP} = 1$. Random initialization of GPR hyperparameters for the first image in each dataset was retained, as the average time per image was calculated over a dataset approximately 35 times larger than in previous cases, making this effect negligible. The baseline assessment was performed on a different computer, specifically with a 13th Gen Intel® Core™ i7-1360P running at 3.1 GHz. However, since both this new reference point and Case 7 (which is compared to it) were computed on the same hardware, the change in computer was not a significant issue for comparison. The resulting computation time was $70\ ms$ per image, compared to $83\ ms$ for Case 5.

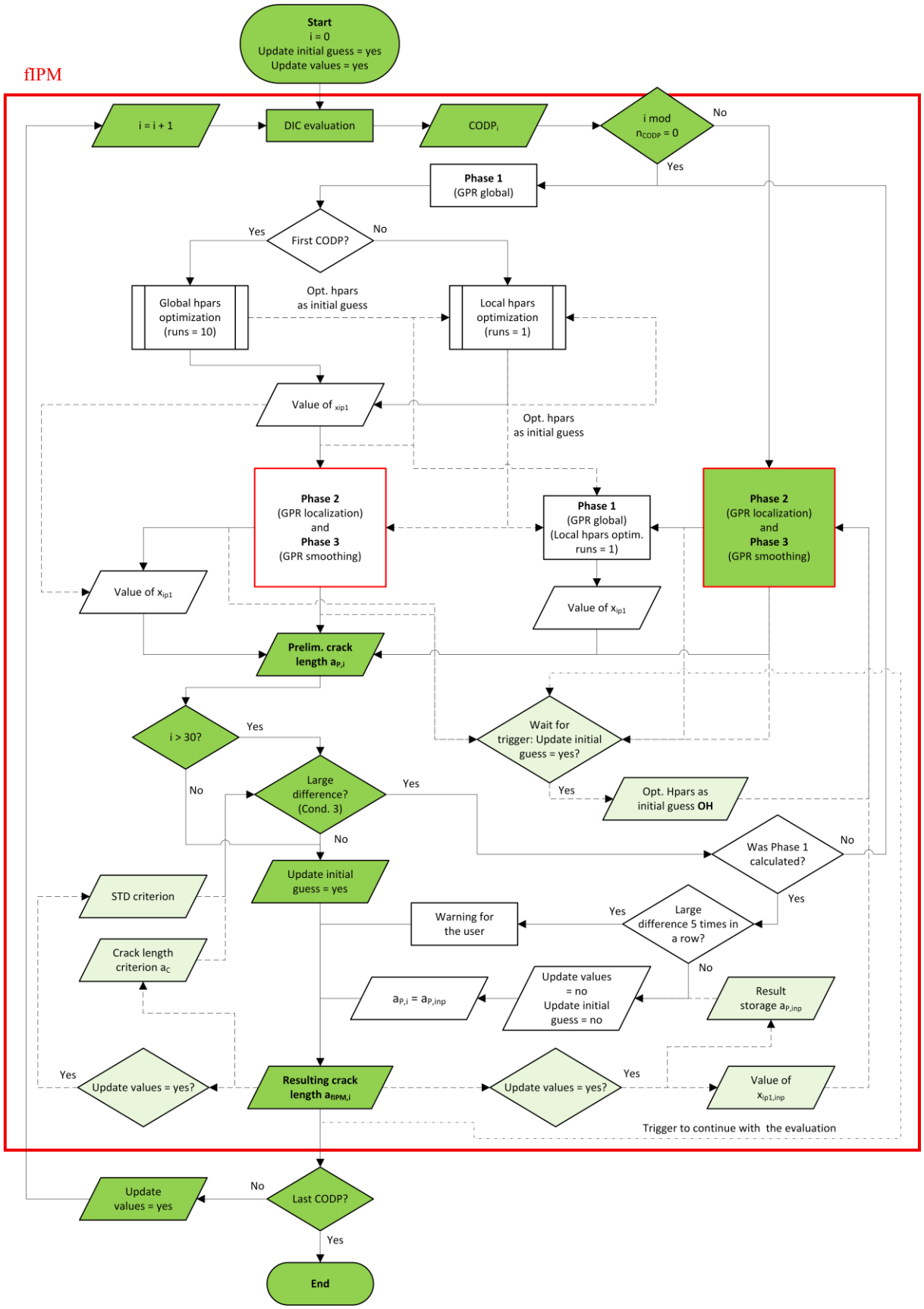

Fig. 43: Flowchart of fast IPM (Inflection point method). This builds upon the scheme in Fig. 30. The most frequent path is indicated in green, and the blocks outlined in red correspond to the encapsulation depicted in Fig. 30. The red outline around the majority of the diagram indicates the encapsulation used for the flowchart in Fig. 50.

There are two main reasons for this reduction. First, the sequence of CODP curves was highly consistent, enabling the hyperparameter optimization to converge more quickly since the optimal values were already close to the initial guess. Second, certain operations—although time-consuming per occurrence—are performed only once or a few times, and their contribution to the total computational time is spread over a much larger number of images. This is evident from the increased percentage share of the three most time-consuming components in the overall computation time, as presented in Tab. 10.

Tab. 10: The most time-consuming operations for the fIPM (fast Inflection point method) algorithm with the average time consumption per processed image, where text highlighted in green represents an improvement compared to the baseline.

Cases:	1: From the Chapter 4 (baseline)	6: fIPM with $n_{CODP} = 1$ (baseline for 7)	7: fIPM with $n_{CODP} = 100$
Function/ operation	Time per image = 88 ms operation [%]	Time per image = 70 ms operation [%]	Time per image = 32 ms operation [%]
GPR[a] regression	86.5	93.0	92.5
GPR[a] derivatives	5.3	2.0	2.0
GPR[a] values extraction	4.1	3.0	3.2

[a] Gaussian process regression

Finally, Case 7—the main objective of this subsection—was compared to this new baseline in Tab. 10 to assess the impact of further computational optimizations in the processing scheme. While the relative share of the three selected components remained almost unchanged, the computation time per image was more than halved, dropping to $32\ ms$ per image—a substantial improvement. This was achieved even with positive outlier detection occurring in 0.15% of cases.

Tab. 11: Updated Tab. 7, showing the IPM (Inflection point method) algorithm with improved computational efficiency (fIPM – fast Inflection point method) in comparison with the results of STM (Strain threshold method) and full-field DIC [79]

	fIPM	STM	Full-field DIC
Hardware operations [ms]	15	15	15
Data extraction from image (DIC) [ms]	34	34	550
Crack length evaluation [ms]	32	1.4	N/A
Max. achievable frame rate[a] [s^{-1}]	**20.4**	**20.4**	**1.8[b]**

[a] Considering the *processing sequence* described in the text (section 4.6), the frame rate is calculated as *1000 ms / max(Hardware operations + Data extraction from image (DIC), Crack length evaluation); unit is equivalent to FPS;*

[b] Assuming that *crack length evaluation < (Hardware operations + Data extraction from image (DIC))*

Although this optimized scheme significantly reduced computation time, it may result in longer computational times under extreme external conditions. Such scenarios include frequently changing

lighting conditions—potentially caused by fluorescent lights flickering—irregular heat waves between the sample and the camera, or improper mounting of the camera system, which can make it more susceptible to external vibrations. These are well-known factors that can negatively affect DIC measurements. Similar issues may also arise in the case of a poorly functioning synchronization device.

5.2.6 Throughput Summary

Finally, Tab. 7 is updated with the results for the IPM algorithm with improved computational efficiency, referred to here as fIPM. The updated results are presented in Tab. 11. Considering the *processing sequence*—where hardware operations and image data extraction (DIC) are performed for the current image while crack length evaluation is performed for the DIC results from the previous image—the implementation of fIPM enables the same maximum frame rate as the STM, which is $20.4\ FPS$.

6 Fatigue Crack Growth Rate Validation Analysis

To further assess the usefulness of IPM—specifically fIPMf—for its intended purpose, this chapter validates crack length estimates via FCGR during running fatigue tests.

Regarding the objective of comparing the proposed methodology with another DIC-based method, a head-to-head comparison with the strain-threshold method (STM) was completed in Chapter 4 (see subsections 4.2.3, 4.4.4, 4.5). There it was shown that STM requires dataset-specific threshold tuning, exhibits strong load dependence, and yields substantially higher errors than IPM, while offering similar throughput under matched hardware. Accordingly, Chapter 6 does not repeat STM comparisons; it instead focuses on validating fIPMf against the non-DIC baseline (VIM) and on quantifying crack-growth-rate accuracy under uninterrupted testing.

6.1 Experimental Program for Data Acquisition

The experimental program used to obtain data for this chapter (hereafter, *current EP)* is very similar to the *Experimental Program for IPM Development* (section 4.1) (hereafter, *previous EP*). In what follows, the previous EP is referenced to highlight the differences implemented in the current EP.

6.1.1 Materials, Geometry, and Preparation

Two MT samples, prepared in accordance with ASTM E647 [19], were used in this study. The samples are designated as MT No. 2 and MT No. 4, with the rationale for this designation explained in subsection 6.3.1. Both samples were made from the same material—standard non-alloy structural steel 1.0038 (S235JR)—and had identical dimensions $W = 60\ mm$ and $B = 6\ mm$. The slot notches, with lengths $a_{n,MT2} = 5.05\ mm$ and $a_{n,MT4} = 5.06\ mm$, were machined to emanate from a circular hole located at the center of each sample. For gripping, a clamping device was used instead of the traditional bolt arrangements. The speckle pattern was applied over the entire ROI, as shown in Fig. 44.

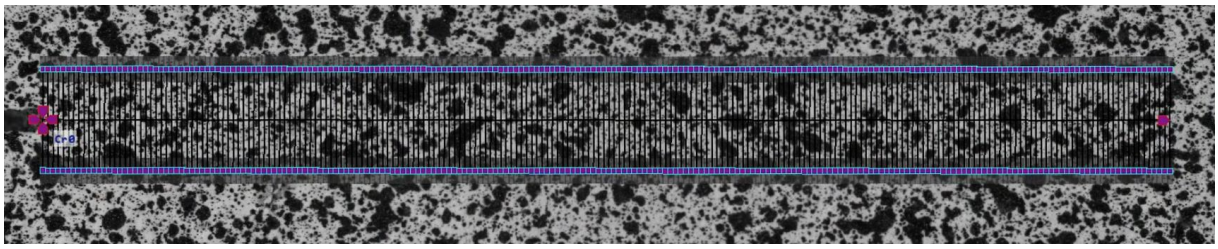

Fig. 44: Speckle pattern on the surface of the MT No. 4 sample, with 200 virtual extensometers (VEs) placed along the measurement line. The distance from the first VE (located at the notch tip on the left) to the last on the right is 14.5 mm.

6.1.2 Experimental Setup

The tests were performed using a Schenck PVQ resonant pulsator with a loading capacity of 60 kN. The camera, lens, and other components shown in Fig. 21 (with the exception of the resonant pulsator) were identical to those used in the previous EP. The exposure time was set to 0.4 ms, which is 20% shorter than in the previous EP, as greater emphasis was placed on preventing motion blur, even though this resulted in darker images.

6.1.3 Testing Procedure

Actions that needed to be taken before the start of the actual test were identical to the previous EP. In this case, the experiment ran without pauses unless a load change was introduced, and the images for evaluation were acquired every n_{sync} frames according to the scheme in Fig. 45. The cycling frequency was $45 - 56\ Hz$.

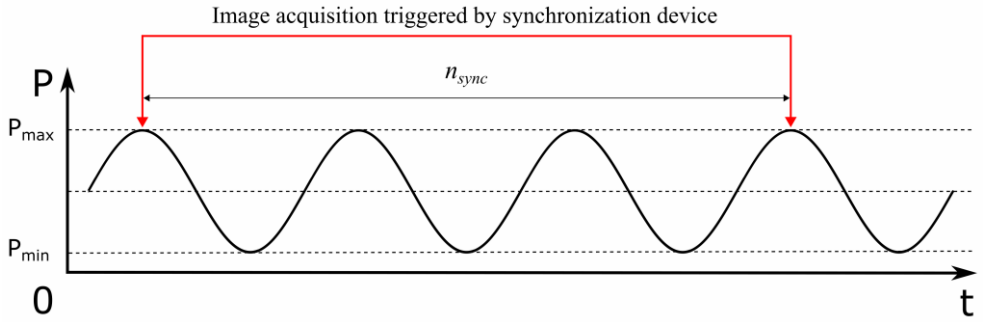

Fig. 45: Schematic of the testing procedure utilizing a synchronization device to trigger image acquisition every n_{sync} cycles, at the moment when the crack is most open (the loading cycle is at its maximum force phase)

For the MT No. 2 sample, a *K*-decreasing test by stepped force shedding was conducted, with the stress ratio held constant at $R = 0.1$. After collecting each dataset at constant force, the test was paused for two reasons: (a) to adjust the force amplitude ($P_a = \frac{P_{max} - P_{min}}{2}$), as summarized in Tab. 12 along with the corresponding n_{sync} values; and (b) to store the data in separate recordings for easier post-processing.

Tab. 12: Overview of force amplitudes (P_a) and n_{sync} parameter for each dataset collected on the MT No. 2 sample.

Dataset No.	P_a *[kN]*	n_{sync} $[-]$
0	14.0	70
1	12.0	70
2	10.0	60
3	9.0	50
4	8.5	50
5	7.5	50
6	6.9	50
7	6.5	50
8	6.2	50

Note on deviations from ASTM E647 [19]:

- The change in P_{max} between consecutive datasets sometimes exceeds the recommended 10%, particularly for the first two adjustments.
- After each change, the crack growth is consistently lower than the recommended $\Delta a_{KD,r} \geq 0.5\ mm$
- Evaluation is performed from a single measured crack size, rather than averaging four

measurements as recommended.

The test for the MT No. 4 sample was performed as *K*-increasing at constant load amplitude of $P_a = 11\ kN$ and $R = 0.1$, so that crack extension itself increased the ΔK and thus the FCGR.

For further evaluation, only the data acquired after the ramp-up phase of loading were considered. The starting point for this evaluation was always assigned a cycle number of $N_{i=0} = 0$.

6.2 Data Processing and Filtering Implementation

This section specifies the image and signal processing settings used to derive the crack length series, motivates the need for filtering due to load-dependent noise, and introduces the fast Inflection point method filtered (fIPMf) as the final workflow. The fIPMf augments the previously introduced fIPM with event-driven updates, adaptive handling of process and measurement noise (Q and R), and monotonicity-preserving refinements. The presentation proceeds from processing parameters and observed noise characteristics to method selection, Kalman filter formulation and enhancements, hyperparameter optimization, performance evaluation, and the integrated workflow with its runtime cost.

6.2.1 Data Processing Settings

The DIC settings were consistent with those listed in Tab. 4, except for the row *Maximal shift of the point*, which had a value of $68\ px$, corresponding to a displacement of $276\ \mu m$. This value represents the maximum displacement observed at the VE endpoints—specifically for the first VE, whose connecting line passed through the notch tip—at the final time step in each dataset.

For comparison, the *maximal shift of the point* for the MT No. 4 sample was $23.9\ px$ at the *last considered time point*[28]. For the MT No. 2 sample across all datasets, the corresponding value was $23.7\ px$, decreasing further to $8.9\ px$, as shown in Tab. 13. These values are substantially lower than those observed in the previous EP, due both to the lower applied load and the higher stiffness of the MT sample compared to the CT sample.

Tab. 13 was additionally extended to include an overview of the maximum $CODP$ values for $l_{ve} = 1.3\ mm$[29]—both at the notch tip location $CODP(x = 0)$ (where the *maximal shift of the point* was evaluated and where VEs experienced the highest displacements), and at the crack tip $CODP(x = a_{fIPM})$. The latter location was added because it indicates the underlying reason for the increasing noise level with decreasing load, a phenomenon observed across the datasets for the MT No. 2 sample, which is evident in Fig. 47. The corresponding load–noise dependence is depicted in Fig. 49.

In dataset No. 8, the *CODP* values at the crack tip location were below $0.6\ \mu m$ throughout the test, resulting in a significantly higher SNR compared to other datasets. For example, in dataset No. 0, the corresponding maximum $CODP(x = a_{fIPM})$ value was $5.3\ \mu m$. Additionally, datasets with higher ordinal numbers exhibited a lower gradient in the area of the inflection point, resulting from the decreasing difference in *CODP* values between the notch tip and crack tip locations (Tab. 13) and from

[28] which refers to the time point considered in the study investigating the effect of the virtual extensometer's length (l_{ve}), described in section 6.3.3.
[29] which is the value selected based on results from the study of virtual extensometer's length (l_{ve}), described in section 6.3.3.

the increasing crack length. Consequently, synchronization device inaccuracies became more prominent when assessing the inflection point in datasets with higher ordinal numbers.

Tab. 13: Overview of the DIC-measured deformation values, expressed as the maximum displacement of a point and the maximum CODP (crack opening displacement projection) values at selected locations at the end of the dataset for the length of virtual extensometers $l_{ve} = 1.3\ mm$

Sample, dataset	*Location*	*Maximal shift of the point*			*Max. CODP*
		[px]	[%[a]]	$[\mu m]$	$[\mu m]$
MT No. 2, Dataset 0	Notch tip	23.7	29.2	96.1	11.9
	Crack tip	23.1	28.6	93.9	5.3
MT No. 2, Dataset 8	Notch tip	8.9	11.0	36.3	3.2
	Crack tip	8.7	10.7	35.2	0.6

[a] of $max(w_{sub}, h_{sub})$

Regarding the other DIC-related parameters of the methodology, $w_{ve} = 14.5\ mm$ was used—this being the maximum value from the interval $w_{ve,r}$ defined in equation (69) —and $n_{ve} = 200$, which corresponds to an f_{ve} value near the upper bound of the interval $f_{ve,r}$ defined in equation (70).

To study the influence of VEs' length, which will be introduced and discussed in this chapter, CODP curves were obtained for each dataset using extensometers with lengths in the interval $l_{ve} \in \langle 0.5, 1.5 \rangle\ mm$ in steps of 0.1 mm. Thus, eleven cases were prepared for each dataset, which will be evaluated and commented upon in section 6.3.3.

6.2.2 Filtering Method Selection

Due to the notable noise in the resulting curves—which became more pronounced as the loading decreased—data filtering was incorporated into the proposed methodology and is included as part of the final workflow (fIPMf). Only the filtered data were subsequently used in the FCGR evaluation in the l_{ve} study and method validation.

Three commonly used data smoothing and noise reduction techniques were considered: the moving average (MA), the Savitzky–Golay filter (SGF), and the Kalman filter (KF). Although the SGF demonstrates accuracy comparable to that of the KF in terms of conformity of the filtered data to the underlying reference [136], [137], the MA yields slightly inferior results. Nevertheless, MA remains widely used due to its simplicity and minimal computational requirements [137].

However, while both MA and SGF are effective in reducing noise, they are inherently non-causal; as window-based methods, they require future data points to compute the current filtered value. This introduces a delay and renders them unsuitable for real-time applications [138]. In contrast, the KF is extensively reported in the literature as suitable for real-time processing ([124], [139], [140])—"because it has merits of real-time, fast, efficient, and strong anti-interference" [140].

6.2.3 Kalman Filter Development

6.2.3.1 Kalman Filter Formulation

Before proceeding to the description of the Kalman filter formulation, it should be noted that the entire

implementation was completed prior to the study investigating the effect of the VEs' length. For its development, data obtained from DIC with $l_{ve,d} = 1.5\,mm$ were used. Other DIC settings were consistent with those listed in Tab. 4, except for the row *Maximal shift of the point*.

When implementing the Kalman filter, it was assumed that the crack length does not change significantly between two consecutive measurements. This led to an identity-based KF with scalar state: $\mathcal{A} = 1$ and $\mathcal{H} = 1$. No control input is included ($\mathcal{G} = 0$). Under these assumptions, equations (23) and (24) reduce to:

$$a_{y,i} = a_{y,i-1} + \omega_{i-1} \tag{82}$$

$$a_{fIPM,i} = a_{y,i} + \psi_{i-1} \tag{83}$$

where $a_{y,i}$ represents the actual crack length ($\mathcal{Y} = \mathfrak{R}$ for *real*), and $a_{fIPMf,i}$ its estimate based on the measured $a_{fIPM,i}$. The index $\mathcal{Y}$ in equations from (82) - (85), and index $\mathcal{Z}$ in equation (85) are placeholders for various subscripts, allowing these equations to be applied universally throughout the following text.

Testing of the KF implementation based on (82) and (83) showed poor performance. Therefore, a two-state variant $\left[a_{y,i}, \frac{da_{y,i}}{dN}\right]$ was examined, but tuning the KF parameters $\boldsymbol{Q}$ and $\boldsymbol{\mathcal{R}}$ proved difficult, and performance was not satisfactory across MT No. 2 datasets (chosen for their wide range of crack-growth rates and noise levels). Consequently, the FCGR was incorporated directly into the scalar process model:

$$a_{y,i} = a_{y,i-1} + \left.\frac{\Delta a_y}{\Delta N}\right|_{N_G^*} (N_{i-1} - N_{i-2}) + \omega_{i-1} \tag{84}$$

where $\left.\frac{\Delta a_y}{\Delta N}\right|_{N_G^*}$ is the most recently updated FCGR, held constant between update events and N_G^* corresponds to the cycle count at which the last update occurred.

6.2.3.2 Event-Driven Update Rule

A new update point N_{G+1}^* is defined as the first cycle count satisfying the *KF update condition* (Fig. 50):

$$N_{G+1}^* = \begin{cases} \min\{N_i > N_G^* : a_y(N_i) - a_y(N_G^*) \geq \Delta a_{\mathcal{Z}}^{thr} \ \vee \ N_i - N_G^* \geq \Delta N^{thr}\}, N_U = 0 \\ \min\{N_i > N_G^* : a_y(N_i) - a_y(N_G^*) \geq \Delta a_{\mathcal{Z}}^{thr}\}, N_U = 1 \end{cases} \tag{85}$$

The parameter N_U is updated once according to the rule:

$$Set\ N_U = 1\ when\ N_i - N_G^* \geq \Delta N^{thr} \tag{86}$$

In these expressions, $\Delta a_{\mathcal{Z}}^{thr}$ and ΔN^{thr} denote the CLI threshold and the cycle increment threshold, respectively. Initially, the crack-based threshold was set to $\Delta a_{\mathcal{Z}}^{thr} = 0.025\,mm$, ensuring at least ten updates occur within $\Delta \mathbb{a}_r \geq 0.25\,mm$.[30] In later stages, this parameter was treated as a hyperparameter,

[30] which is an interval recommended in [19] for final crack growth rate evaluation. Each interval provides one point in the $\frac{d\mathbb{a}}{dN} = f(\Delta K)$ relation.

with its value determined through optimization. The cycle-based threshold was set to $\Delta N^{thr} = 50000$, for reasons discussed in the following paragraph.

The parameter $N_U \in \{0,1\}$ selects which branch of the update KF update condition is active. Initially, $N_U = 0$, meaning that the update is triggered when either the crack-length increment reaches Δa_Z^{thr} or the cycle increment reaches ΔN^{thr}. This ensures an early update in very slow, near-threshold growth regimes, allowing the predictor to use a non-zero growth rate instead of the zero rate with which it is initialized. If an update is triggered by the ΔN^{thr} condition, rule (86) permanently flips the flag to $N_U = 1$. Thereafter, only the Δa_Z^{thr} condition remains active.

The KF update condition is evaluated only for $N_i \geq N_0^*$ to exclude the initial segment dominated by load ramp-up. This segment appears in the measured crack length signal because image acquisition starts before the actual test. The first image of the unloaded specimen is taken for correlation, triggered by an initial pulse sent from the synchronization device to the cameras when it is started.

After this, the system waits for an external input signal from the load cell before further triggering. Once this external signal becomes strong enough, the synchronization device begins operating, which happens relatively quickly. As a result, most of the ramp-up phase is included in the measured crack length data.

During ramp-up—especially at the moment the synchronization device starts triggering—the load is still low, and the measured *CODP* values on the specimen are extremely small. In this situation, signal errors can be non-negligible. This rule therefore gives the user an option to exclude the ramp-up portion from the processed crack length signal.

The index G denotes the most recent point in the sequence $\{N_0^*, N_1^*, \dots, N_G^*\}$ at which the FCGR has been refreshed. With this formulation, equation (84) incorporates the control input model $\mathcal{G}$ via the FCGR, while the control input is $u_{i-1} = (N_{i-1} - N_{i-2})$. Equation (84) replaces equation (82) in the subsequent KF implementation.

To conclude, this approach incorporates FCGR into the KF formulation as a piecewise-constant value, updated at the moments defined by the KF update condition.

6.2.3.3 Kalman Filter Implementation

The employed KF implementation for this use case has, in the prediction phase, the form:

$$a_{fIPMf,i}^{-} = a_{fIPMf,i-1} + \left.\frac{\Delta a_{fIPMf}}{\Delta N}\right|_{N_G^*} (N_{i-1} - N_{i-2}) \tag{87}$$

$$\mathcal{P}_i^{-} = \mathcal{P}_{i-1} + Q \tag{88}$$

In case of the first iteration ($i = 0$) of fIPMf, the algorithm initialized as follows (in in Fig. 50 referred to as initialization parameters):

- $a_{fIPMf,i-1} = a_{fIPM,i}$
- $N_G^* = N_0^* = 5000$ (user-adjustable to accommodate machine-specific ramp-up durations)
- $\left.\frac{\Delta a_{fIPMf}}{\Delta N}\right|_{N_G^*} = 0$
- $N_{i-1} = N_{i-2} = 0$

The FCGR is updated based on the event-driven update rule defined in equation (85) for $\mathcal{Y} = \mathcal{Z} = fIPMf$. Once next update occurs at N^*_{G+1}, following pairs:

$$\left(a_{fIPMf,j}, \mathrm{N}_j\right), j \in \mathcal{J} \tag{89}$$

$$\mathcal{J} = \{i | N^*_G \leq N_i \leq N^*_{G+1}\} \tag{90}$$

are fitted using linear regression, similar to equation (77), but with $a_{fIPM,j}$ replaced by $a_{fIPMf,j}$. The regression coefficient $a_{reg,G}$, representing the slope of the fitted line, is then taken as the updated FCGR:

$$\left.\frac{\Delta a_{fIPMf}}{\Delta N}\right|_{N^*_{G+1}} = a_{reg,G} \tag{91}$$

This value is held constant until the next update event, as defined by equation (85) for $\mathcal{Y} = fIPMf$.

In the correction phase, the Kalman gain, updated state estimate, and a posteriori error variance are computed, respectively, as:

$$\kappa_i = \frac{\mathcal{P}_i^-}{\mathcal{P}_i^- + \mathcal{R}} \tag{92}$$

$$a_{fIPMf,i} = \bar{a}_{fIPMf,i} + \kappa_i (a_{fIPM,i} - \bar{a}_{fIPMf,i}) \tag{93}$$

$$\mathcal{P}_i = (1 - \kappa_i)\mathcal{P}_i^- \tag{94}$$

6.2.4 Enhancements to the Kalman Filter

6.2.4.1 Adaptivity Implementation into Kalman Filter

The performance of the Kalman filter depends critically on the proper selection of $\boldsymbol{Q}$ and $\boldsymbol{\mathcal{R}}$ [141]. An improper choice of these parameters can significantly degrade the filter's performance or even cause it to diverge [142]. The measurement-noise variance $\boldsymbol{\mathcal{R}}$ can often be obtained by offline analysis of the variance of the measurement noise using available data. In contrast, determining $\boldsymbol{Q}$ is usually more challenging, as the underlying process cannot be directly observed [125].

When testing the above-discussed KF implementation on MT No. 2, it was observed that different Q and $\mathcal{R}$ settings led to conflicting performance trade-offs. Parameter selections that worked well for datasets with higher FCGR and lower noise caused KF to follow noise of the measurement excessively in cases with lower FCGR and higher noise. Conversely, tuning for the latter case led to significant underprediction for datasets with higher FCGR, as the filter failed to follow the faster crack growth. This trade-off will hereafter be referred to as the *Q-$\mathcal{R}$ problem*.

This behavior was similar to that observed for the implementation based on equation (82), although it was less pronounced. Nevertheless, the remaining performance limitations motivated a change to an adaptive $\mathcal{R}$ update in order to better handle varying noise conditions. With an adaptive approach, it is still necessary to perform the initial setting of noise variance $\mathcal{R}_{init}$, but the overall performance of the KF depends less on *a priori* knowledge of the process, as the filter learns from each new measurement [141], which is favorable for the fIPMf. The same principle applies to the initial setting of the process

variance Q_{init} when Q is updated adaptively [141]. Additionally, the initial value of the *a posteriori* error variance $\mathcal{P}_{init}$ must be selected as well. The selection of these initial values is detailed in subsection 6.2.2.3.

The innovation-based adaptive estimation (IAE) method was selected due to its straightforward implementation and interpretation, as well as its lower computational overhead compared with, for example, multiple-model adaptive estimation, which runs a set of parallel filters whose results are weighted to obtain the final estimate [141]. Initially, the adaptive procedure described in [141] —which uses the mean innovation over a fixed-size window—was implemented. However, in the present use case this approach reacted too abruptly: when an outlier-induced large innovation exited the window, the estimated $\mathcal{R}$ changed sharply in the following iteration. This behavior was deemed unsuitable for the application.

To address this, the forgetting-factor approach $0 < \gamma_{\mathcal{R}} < 1$ defined in [143] was adopted. This method ensures smoother transitions in $\mathcal{R}$ by incorporating all past innovations with exponentially decreasing weights—the older the innovation, the smaller its influence. Combining the approaches from [141] and [143], the adaptive $\mathcal{R}$ update was implemented as:

$$\mathcal{R}_{i+1}^{cand} = \gamma_{\mathcal{R}}\mathcal{R}_i + (1-\gamma_{\mathcal{R}})\left[\left(a_{fIPM,i} - \bar{a_{fIPMf,i}}\right)^2 - \mathcal{P}_i^-\right] \tag{95}$$

$$\mathcal{R}_{i+1} = \max\left(\min\left(\mathcal{R}_{i+1}^{cand}, \mathcal{R}_{max}^{thr}\right), \mathcal{R}_{min}^{thr}\right) \tag{96}$$

where

- $\gamma_{\mathcal{R}}$: forgetting factor for the adaptive $\mathcal{R}$ update
- $\mathcal{R}_{i+1}^{cand}$: candidate value for $\mathcal{R}$ in the next iteration
- $\left(\mathcal{R}_{min}^{thr}, \mathcal{R}_{max}^{thr}\right)$ limits used to clip extreme candidate values

Testing this implementation showed that the Q–$\mathcal{R}$ problem persisted, as illustrated in Fig. 46 (*Filtered – Q: constant),* although qualitative analysis indicated that the resulting curves were smoother due to the adaptive $\mathcal{R}$.

Consequently, adaptive Q was introduced to better accommodate varying FCGR and complement the adaptive $\mathcal{R}$ in mitigating the Q–$\mathcal{R}$ problem. The IAE-based adaptation of Q described in [141] was initially implemented. While this approach eliminated underprediction, it significantly increased oscillations in the filtered signal, because the filter reacted too strongly to noise, as depicted in Fig. 46 (*Filtered – Q: innovation*). This indicated the need for a compromise between a constant Q overly aggressive adaptation.

In the final formulation, Q adaptation is tied to the obvious discrepancy between the selected process model and the known physical behavior of the system—the crack growth is not linear but accelerates with increasing crack length. Accordingly, Q is updated only at the event-driven points of equation (85) for $\mathcal{Y} = \mathcal{Z} = fIPMf$—the same points where $\mathcal{G}$ is updated in equation (87). Rather than innovation-based updates, Q uses the change in $\mathcal{G}$ between successive update points:

$$Q_{N_{G+1}^*}^{cand} = \gamma_Q Q_{N_G^*} + (1-\gamma_Q)\left[\left(\left.\frac{\Delta a_{fIPMf}}{\Delta N}\right|_{N_{G+1}^*} - \left.\frac{\Delta a_{fIPMf}}{\Delta N}\right|_{N_G^*}\right)^2 \kappa_i^2\right] \tag{97}$$

$$Q_{N^*_{G+1}} = \max\left(\min\left(Q^{cand}_{N^*_{G+1}}, Q^{thr}_{max}\right), Q^{thr}_{min}\right) \tag{98}$$

where

- $0 < \gamma_Q < 1$: forgetting factor for the adaptive Q update
- $Q^{cand}_{N^*_{G+1}}$: candidate value for Q for the next interval, until the N^*_{G+2} update is triggered
- $\left(Q^{thr}_{min}, Q^{thr}_{max}\right)$ limits used to clip extreme candidate values

Finally, advance the event index:

$$G = G + 1 \tag{99}$$

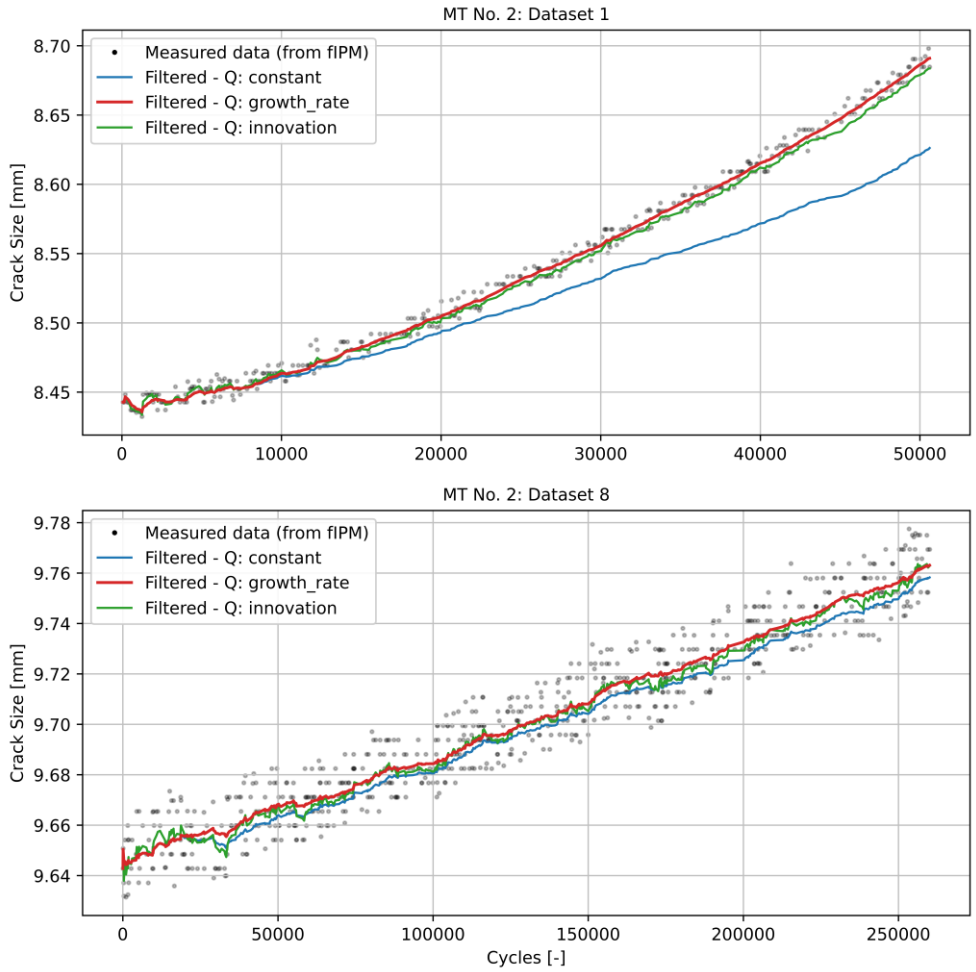

Fig. 46: Kalman filter-filtered signals compared with measured data from the fast Inflection point method (fIPM) for: a) constant Q (process variance), b) adaptive Q based on changes in fatigue crack growth rate (FCGR) (fIPMf), and c) innovation-based adaptive Q. Two cases are shown: MT No. 2: Dataset 1 (higher FCGR, lower noise) and MT No. 2: Dataset 8 (lower FCGR, higher noise). Dataset 1 was chosen over Dataset 0 for its greater number of cycles and more pronounced curvature. The input parameters Q_{init}, $\mathcal{R}_{init}$, γ_Q, γ_R, Δa^{thr}_{fIPMf} and $\mathcal{P}_{init}$—where the subscript "init" denotes values used in the initial iteration of the KF within fIPMf—are listed in Tab. 14. Virtual extensometers' length $l_{ve,d} = 1.5\ mm$. Note that the vertical axis represents crack size (crack-length value from fIPM/fIPMf + corresponding notch length).

By synchronizing Q updates with the control input transition $\mathcal{G}$, the process noise adaptation is linked to

changes in the estimated FCGR. This ties the process error to the model–reality discrepancy, reflecting the inherent non-linearity of actual crack growth behavior and effectively solves the Q-$\mathcal{R}$ problem, as illustrated in the examples in Fig. 46 (*Filtered – Q: growth_rate*). The same case is shown in Fig. 47 (*Filtered – Refinement Mode: none*) and will hereafter be referred to as the case without refinement.

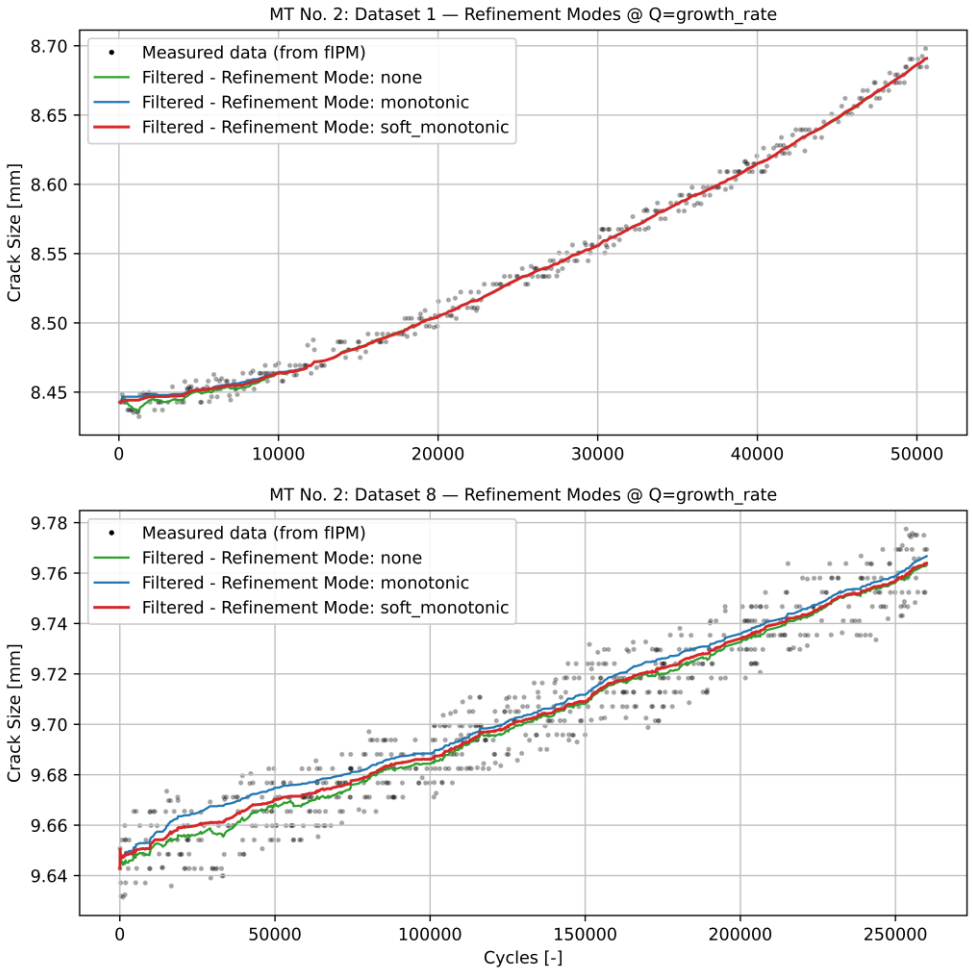

Fig. 47: Kalman filter-filtered signals using adaptive Q (process variance) based on fatigue crack growth rate (FCGR) change, compared with measured data (fIPM) for refinement modes: a) none (corresponding to Filtered – Q: growth_rate in Fig. 46), b) monotonic and c) soft monotonic (fIPMf – fast Inflection point method filtered). Two cases are shown: MT No. 2: Dataset 1 (higher FCGR, lower noise) and MT No. 2: Dataset 8 (lower FCGR, higher noise). Dataset 1 was chosen over Dataset 0 for its greater number of cycles and more pronounced curvature. The input parameters Q_{init}, $\mathcal{R}_{init}$, γ_Q, γ_R, Δa_{fIPMf}^{thr} and $\mathcal{P}_{init}$ are listed in Tab. 14. Virtual extensometers' length $l_{ve,d} = 1.5\ mm$. Note that the vertical axis represents crack size (crack-length value from fIPM/fIPMf + corresponding notch length).

6.2.4.2 Kalman Filter Refinement for Monotonic Crack Growth

Finally, the KF output was refined to enforce the physically meaningful property that crack growth is monotonic; decreases in crack length estimates have no physical basis.

- Monotonic refinement: $If\ a_{fIPMf,i} < a_{fIPMf,i-1}: a_{fIPMf,i} = a_{fIPMf,i-1}$. This works well for low-noise datasets but tends to overpredict in high-noise cases (Fig. 47, *Filtered – Refinement Mode: monotonic*).
- Soft monotonic refinement: Introduced to handle high-noise cases while avoiding overprediction. It defines the threshold:

$$\tau_i = \frac{1}{L_{soft}} \sum_{j=0}^{L_{soft}-1} a_{fIPMf,i-1-j}, i \geq L_{soft} \quad (100)$$

where $L_{soft} = 3$ in this work. The update rule is formulated as:

$$a_{fIPMf,i} = \begin{cases} \tau_i, a_{fIPMf,i} < \tau_i \\ \frac{a_{fIPMf,i-2} + a_{fIPMf,i}}{2}, a_{fIPMf,i} \geq \tau_i \wedge a_{fIPMf,i} < a_{fIPMf,i-1} \\ a_{fIPMf,i}, otherwise \end{cases} \quad (101)$$

This approach checks the current estimate against τ_i instead of only the previous value. If the estimate falls below τ_i, it is raised to τ_i. If it exceeds τ_i but is also lower than the previous estimate, the previous estimate is treated as an outlier and replaced with the mean of the current and antepenultimate values. In this way, spurious drops are suppressed while persistent overprediction—typical of the strict monotonic approach—is avoided, as illustrated in Fig. 47 (*Filtered – Refinement Mode: soft_monotonic*). This refinement step is applied in the workflow prior to evaluating the *KF update condition*.

6.2.4.3 Hyperparameters for Kalman Filter

As described in the preceding subsections (6.2.3 – 6.2.4.2), the implemented Kalman filter requires several parameters to be set for effective operation. These parameters—also included in the set of initialization parameters (Fig. 50) and listed in Tab. 14 —were treated as hyperparameters and optimized to ensure robust performance. The optimization was conducted on all MT No. 2 datasets, which are well suited for this purpose as they span a wide range of crack-growth rates and noise levels, providing a comprehensive basis for tuning.

The hyperparameter tuning was carried out using a two-stage optimization procedure implemented with the Optuna Bayesian optimization framework [144]. This framework applies a probabilistic model (Tree-structured Parzen Estimator, TPE) to guide the search for optimal parameter combinations. In contrast to purely random search, Bayesian optimization uses the results of previous trials to update a surrogate model of the objective function, focusing subsequent sampling in regions of the parameter space that are more likely to yield improvements. This strategy enables more efficient convergence to near-optimal solutions, especially in high-dimensional search spaces.

The objective function to be minimized was defined as the total mean square error (MSE) between the Kalman filter output (fIPMf) and a smooth reference curve obtained via SGF. The SGF was configured with a polynomial order of 2 and a window length of 100 points, ensuring a robust, low-noise reference while preserving the underlying crack growth trend. This loss function penalized deviations between the filtered series and the SGF baseline equally across all considered datasets, with the final value being the sum of per-dataset MSE values.

In the first optimization stage, each hyperparameter was allowed to vary over a deliberately wide interval (“First interval” in Tab. 14) to explore the full plausible parameter space. This stage consisted of 25 000 trials, where each trial refers to one complete run of the Kalman filter on all considered datasets using a specific set of hyperparameters proposed by the optimization algorithm. Approximately 80 % of trials were pruned early using Optuna’s median pruning strategy. In this approach, a trial is stopped when its

intermediate performance falls below the median performance of completed trials at the same evaluation stage—in this study meaning the point when one dataset has been processed within a trial—thereby discarding underperforming configurations before all datasets are processed and reallocating resources to more promising candidates. The outcome of this stage was a set of high-performing regions of the parameter space, identified by extracting the hyperparameter values corresponding to the top 5 % lowest-loss (best) trials.

Tab. 14: Parameters required for the proper functioning of the implemented Kalman filter, treated as variables (hyperparameters) in the two hyperparameter optimization stages, along with their optimal values and the search intervals used in the first and second optimizations.

Hyperparameter[a]	*Final values*	*First interval*	*Second interval*
$\mathrm{Q}_{\mathrm{init}}\ [mm^2]$	$\mathbf{1.44 \times 10^{-7}}$	$(10^{-12}, 10^{-2})$	$(10^{-7}, 10^{-6})$
$\mathcal{R}_{\mathrm{init}}\ [mm^2]$	$\mathbf{2.11 \times 10^{-6}}$	$(10^{-8}, 10^{-2})$	$(5 \times 10^{-7}, 5 \times 10^{-5})$
$\gamma_Q\ [-]$	$\mathbf{0.956}$	$(0.1, 0.999)$	$(0.88, 0.99)$
$\gamma_{\mathcal{R}}\ [-]$	$\mathbf{0.992}$	$(0.1, 0.999)$	$(0.99, 0.999)$
$\Delta a_{\mathrm{fIPMf}}^{thr}\ [mm]$	$\mathbf{0.0123}$	$(0.005, 0.1)$	$(0.01, 0.025)$
$\mathcal{P}_{\mathrm{init}}\ [mm^2]$	$\mathbf{0.0125}$	$(10^{-6}, 10^{0})$	$(0.002, 1.0)$

[a] meaning of the particular hyperparameters is discussed throughout subsections 6.2.3 – 6.2.4

The "Second interval" in Tab. 14 was then defined according to the bounds spanned by these top-performing configurations. A second optimization run was carried out over these narrower, high-potential ranges. This stage comprised 20 000 trials, again with approximately 80 % pruning. By concentrating the search within these refined intervals, the optimization process could more effectively exploit the most promising parameter regions found in stage one, achieving higher precision in parameter estimation.

The final hyperparameter values in Tab. 14 represent the configuration with the lowest total MSE in the second-stage optimization. This configuration provided robust performance across datasets with widely varying FCGR and noise levels.

6.2.4.4 Final Q and $\mathcal{R}$ Threshold Bounds

The threshold bounds $\left(Q_{min}^{thr}, Q_{max}^{thr}\right)$ and $\left(\mathcal{R}_{min}^{thr}, \mathcal{R}_{max}^{thr}\right)$ are used to clip Q and $\mathcal{R}$ in order to remove extreme candidate values and prevent KF instability under unforeseen conditions. To set these bounds, the distributions of Q and $\mathcal{R}$ across all MT No. 2 datasets were analyzed; the results are shown in Fig. 48. For this study, a wide parameter range corresponding to the first *interval* in Tab. 14 was used.

For Q, values tend to decrease from Q_{init}, but not substantially—the modus bin includes Q_{init}. For $\mathcal{R}$, values increase rapidly from $\mathcal{R}_{\mathrm{init}}$, and the modus bin lies approximately one order of magnitude above $\mathcal{R}_{\mathrm{init}}$. Based on these observations, the bounds for Q and $\mathcal{R}$ were set such that the observed minima and maxima are padded by a safety margin. An exception is $\mathcal{R}_{min}^{thr}$: a small accumulation appeared at the lower limit of the *first interval* in Tab. 14, which is considered non-physical (such low noise is unlikely), especially given the overall increase from $\mathcal{R}_{\mathrm{init}}$, including in the lowest-noise dataset. Therefore, $\mathcal{R}_{min}^{thr}$

was set by adding a safety margin to $\mathcal{R}_{\text{init}}$.

Tab. 15: Values of Q (process variance) and $\mathcal{R}$ (noise variance) extracted from the histograms in Fig. 48, together with the final thresholds

Parameter	*Min. value*	*Max. value*	*Modus bin*	*Final thresholds*
$Q\ [mm^2]$	5.25×10^{-8}	1.44×10^{-7}	$(1.41 \pm 0.03) \times 10^{-7}$	$(5 \times 10^{-9}, 1 \times 10^{-6})$
$\mathcal{R}\ [mm^2]$	1.00×10^{-7}	8.46×10^{-5}	$(6.56 \pm 0.57) \times 10^{-5}$	$(1 \times 10^{-7}, 7 \times 10^{-4})$

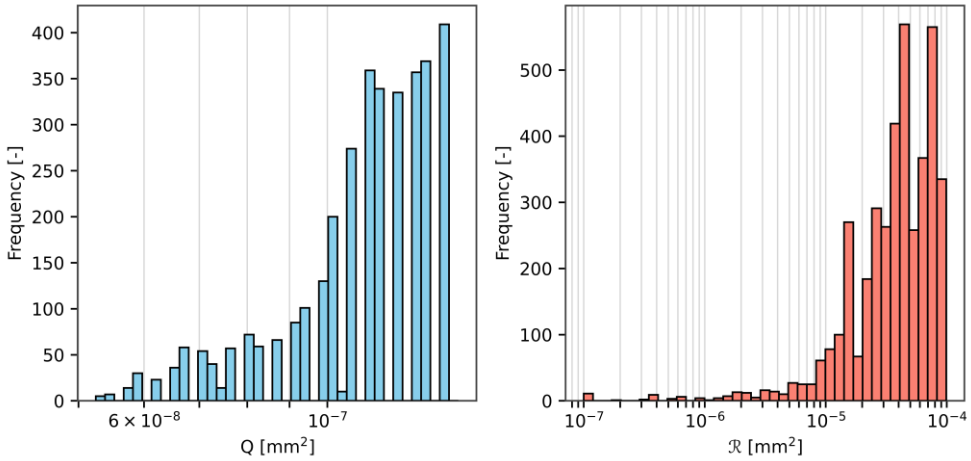

Fig. 48: Q (process variance) and $\mathcal{R}$ (noise variance) value distributions across all MT No. 2 datasets

6.2.5 Kalman Filter Performance Evaluation

The effectiveness of the Kalman filter in reducing noise in the measured crack length signal was assessed by comparing noise levels in both the raw DIC-derived crack length data and the Kalman-filtered output against a smooth reference curve. The reference was obtained using the same SGF configuration employed during hyperparameter optimization.

Noise was quantified as the standard deviation of the residuals, calculated as the difference between the evaluated crack length series (raw or filtered) and its SGF-based reference. The results are presented in Fig. 49.

For the measured (unfiltered) crack length data, noise levels increased sharply with decreasing load, following an approximate power-law dependence. This behavior is consistent with the load–noise relationship discussed in the previous subsections (6.2.1 – 6.2.2), where the decrease in *max. CODP* values between MT No. 2 dataset 0 and dataset 8 (Tab. 13) indicates the underlying reason for the increasing noise level with decreasing load.

Application of the Kalman filter reduced the crack length noise by approximately one order of magnitude, resulting in noise amplitudes well below 1 μm across all LLs. The residual variation in filtered noise exhibited only a slight downward trend with decreasing load, which—relative to the pronounced variation in the unfiltered case—can be considered essentially constant.

To complement the noise analysis, the MAE of the filtered crack length signal was computed relative to the SGF-smoothed reference curve derived from the measured data. The MAE remained consistently smaller than the noise level of the unfiltered signal but slightly higher than the residual noise in the

filtered signal.

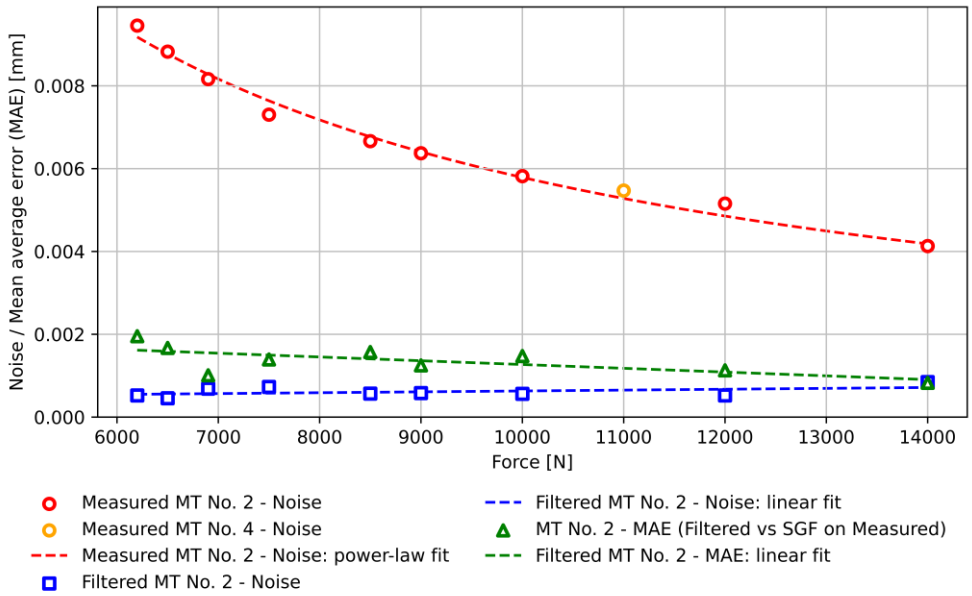

Fig. 49: Load–noise dependence for both measured and filtered data, together with load–MAE (mean absolute error) dependence for the filtered data, where the MAE is calculated with respect to the smoothed reference curve obtained from measured data. Virtual extensometers' length $l_{ve,d} = 1.5\ mm$

A mild increase in MAE with decreasing load was observed. Qualitative inspection indicated that this trend is mainly attributable to the soft monotonic refinement step. While this refinement enforces physically realistic monotonic crack growth and suppresses spurious drops, it can also shift certain points slightly away from the SGF reference, marginally increasing the MAE. This trade-off is considered acceptable, as the refinement significantly improves robustness in high-noise conditions.

It can be concluded that the implemented Kalman filter, combined with soft monotonic refinement, substantially reduces noise in the measured crack length signal—down to sub-micron levels—while preserving the underlying growth trend. Its performance remains stable across all tested LLs, making it well suited for integration into the final fIPMf workflow.

6.2.6 Fast Inflection Point Method Filtered

The fast variant of IPM, filtered using the proposed Kalman filter (fIPMf), is adopted as the final approach in this work and forms the backbone of the proposed methodology. Fig. 50 presents the fIPMf flowchart, which builds on the flowcharts shown in Fig. 43 and Fig. 30. Testing indicates that it increases the fIPM processing time by no more than 0.2 ms per image.

6.2.7 Summary and Conclusion

This section consolidates a coherent processing pipeline for extracting and stabilizing crack-length estimates under varying test conditions. The resulting workflow couples event-triggered updates with adaptive noise handling and monotonicity safeguards, yielding smooth, physically consistent histories at negligible computational cost. Overall, the approach is practical and reproducible across datasets, providing a robust foundation for the subsequent validation and application presented later.

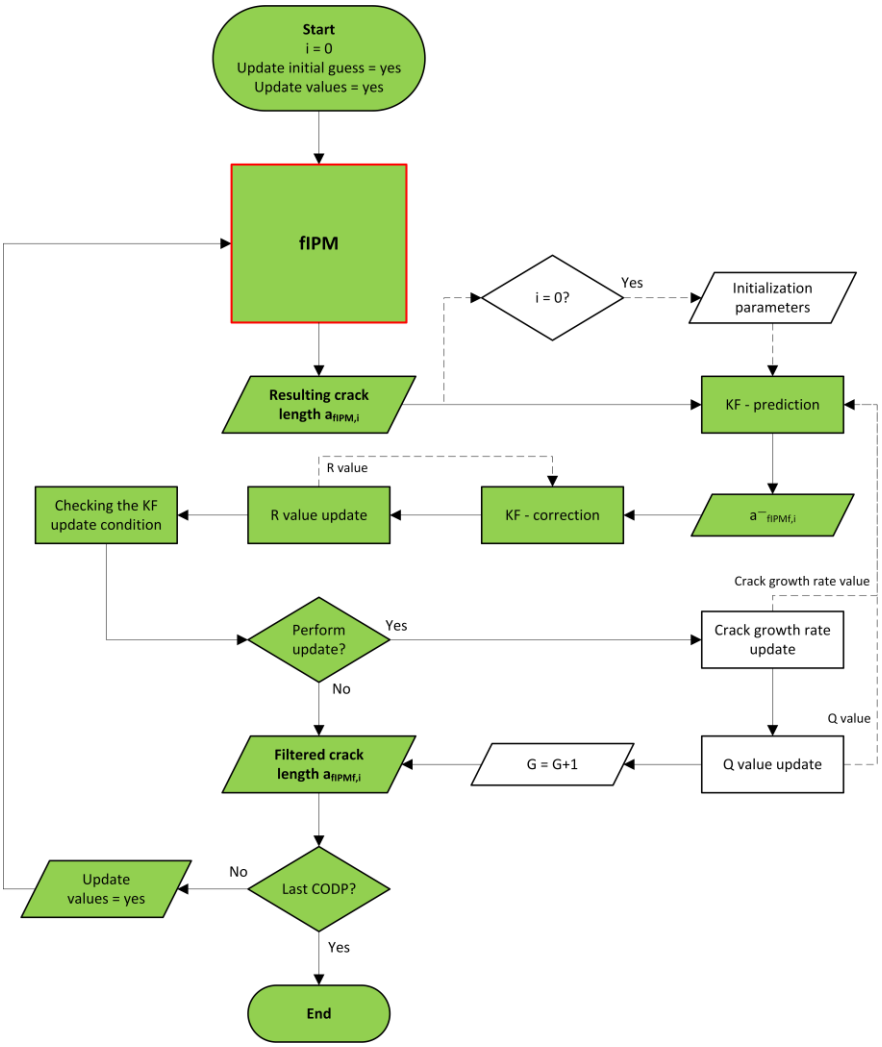

Fig. 50: Flowchart of fast IPM (Inflection point method) filtered (fIPMf). This builds upon the scheme in Fig. 43. The most frequent path is indicated in green, and the blocks outlined in red correspond to the encapsulation depicted in Fig. 43.

6.3 Validation of Measurement and Method

Although the primary aim of this chapter is to validate the proposed method (fIPMf) in terms of crack length assessment and FCGR determination during running fatigue tests, this chapter also examines the influence of the VEs' length l_{ve} on the same datasets. Consequently, the presentation of the validation and parameter study results is interlinked.

VEs are used to obtain CODP curves from DIC images, which serve as input for fIPMf. Their length, l_{ve}, is therefore a key parameter influencing the results of the method. The influence of the VEs' length was previously investigated for the IPM version of the algorithm in section 4.4. In that study, the minimum possible value was $l_{ve} = 1.5\ mm$, imposed by the polished band in the specimens used for VIM validation. Thus, only values larger than $1.5\ mm$ were examined.

In contrast, the MT specimens analyzed here feature a speckle pattern over the entire ROI, which enables the study of l_{ve} values smaller than $1.5\ mm$. To ensure comparability with baseline data, all results are expressed in terms of FCGR(da/dN) and SIF (specifically the maximum load-cycle value, K_{max}).

6.3.1 Baseline Data (VIM Tests)

The baseline validation data were kindly provided by the Institute of Physics of Materials in Brno and are used here with their permission. These measurements were obtained using the VIM technique on samples of the same geometry and material, tested on the same machine. The specimens were designated MT No. 1–4; notably, MT No. 2 and MT No. 4 were later also used for fIPMf validation in this chapter.

An overview of the VIM tests is given in Tab. 16. All tests were performed under *K*-decreasing loading, except for MT No. 3, where, after an initial *K*-decreasing test, a *K*-increasing test followed. For all tests, the stress ratio was kept constant at $R = 0.1$, the same as in the measurements for fIPMf evaluation.

FCGR were evaluated using average crack size values across four measurements, i.e., the front and back side for two cracks present. In all cases, the change in P_{max} between consecutive datasets was below the recommended 10%, with a modus of 2.5%. After each reduction of P_{max}, the increment Δa remained consistently below the recommended $\Delta a_{KD,r} > 0.5\,mm$. For the readout condition, the recommended $\Delta a_r > 0.25mm$ was consistently met for $K_{max} > 11.2\ MPa\sqrt{m}$.

Tab. 16: Overview of MT No. 1–4 tests performed using VIM (Visual inspection method), ($R = 0.1$)

MT No.	P_a [a] *[kN]*	K_{max} [b] $[MPa\sqrt{m}]$	$\frac{da}{dN}$ [c] $\left[\frac{mm}{cycle}\right]$	$N_{overall}$ [d] $[10^3]$	*Points* [e] $[-]$
1	$\langle 11.70 - 8.21 \rangle$	$\langle 9.75 - 7.85 \rangle$	$\langle 1.70 \times 10^{-6} - 1.67 \times 10^{-8} \rangle$	1968	12
2	$\langle 11.70 - 5.76 \rangle$	$\langle 9.17 - 6.02 \rangle$	$\langle 1.63 \times 10^{-6} - 2.50 \times 10^{-10} \rangle$	5189	21
3	$\langle 13.63 - 6.06 \rangle$, 9.00	$\langle 11.97 - 6.47 \rangle$, $\langle 9.10 - 17.29 \rangle$	$\langle 5.97 \times 10^{-6} - 5.00 \times 10^{-9} \rangle$, $\langle 6.25 \times 10^{-7} - 3.73 \times 10^{-5} \rangle$	4853, 2040	18, 34
4	$\langle 13.63 - 6.54 \rangle$	$\langle 11.22 - 6.88 \rangle$	$\langle 4.40 \times 10^{-6} - 3.75 \times 10^{-9} \rangle$	5132	19

[a] cycle force amplitude; [b] cycle maximum stress intensity factor; [c] fatigue crack growth rate; [d] overall number of cycles achieved in test; [e] in the $da/dN = f(K_{max})$ plot

In addition to the raw VIM data, datapoints of the corresponding NASGRO fit were provided. From these datapoints, the NASGRO coefficients were reconstructed by fitting according to equation (40). The VIM datapoints and NASGRO fit are shown in Fig. 57 alongside the results of the fIPMf method.

Tab. 17: Overview of fitted NASGRO parameters (white) and selected inputs (gray). Variable definitions are provided in section 3.5. Results are shown with (w/ clo.) and without (w/o clo.) crack closure.

$C_{PL}\left[mm(MPa\sqrt{m})^{-m_{PL}}\right]$	m_{PL} $[-]$	p_{NG} $[-]$	ΔK_{th} $[MPa\sqrt{m}]$	f_{NG} $[-]$	q_{NG} $[-]$	K_c $[MPa\sqrt{m}]$
6.69×10^{-8} (w/ clo.) 1.10×10^{-8} (w/o clo.)	2.89	0.701	6.30	0.518 (w/ clo.) R (w/o clo.)	0	N/A

During fitting, the $RMSE_{log_{10}}$ defined in equation (108) (see subsection 6.3.3) was minimized. The parameter q_{NG} consistently reached the lower bound of its interval; lowering this bound further improved the fit. Ultimately, q_{NG} was set to zero, as the datapoints appeared to originate from a NASGRO equation omitting the fracture toughness cutoff. The resulting fitting parameters are summarized in Tab. 17.

The parameters used to evaluate Newman's crack-opening function $f_{NG}(R)$ (equation (42)) are listed in Tab. 18. Calculations assume plane-stress conditions. The nominal far-field stress was set using a load

amplitude of $P_a = 9\ kN$ chosen as the modus value in Tab. 16. The material properties were taken from ČSN EN 10025-2 [145]; the yield strength σ_y was taken as the minimum declared value, and the ultimate tensile strength σ_u as the mid-interval value.

Tab. 18: Overview of inputs (white) used to calculate the Newman crack opening function and intermediate results (gray), the meaning of variables is explained in detail in section 3.5.

$P_{max}\ [N]$	$\sigma_y\ [MPa]$	$\sigma_u\ [MPa]$	$R\ [-]$	$\beta\ [-]$	$\frac{\sigma_{max}}{\sigma_0}\ [-]$
20000	235	435	0.1	1.0	0.166

6.3.2 Evaluation on MT Samples Using fIPMf

For the MT No. 2 datasets (Fig. 51), each dataset represents a single point in the $da/dN - K_{max}(\mathbb{a})$ dependence, since the tests were relatively short and the recommended $\Delta\mathbb{a}_r \geq 0.25\ mm$ was satisfied only for datasets No. 1 and 2. The FCGR for a particular dataset was evaluated as:

$$\left(\frac{da}{dN}\right)_{fIPMf} = \frac{a_{fIPMf}(N_{end}) - a_{fIPMf}(N_0^*)}{N_{end} - N_0^*} \tag{102}$$

and the corresponding maximum SIF as:

$$K_{max} = (1-R)^{-1}\Delta K_{MT}(\mathbb{a}_{mid,ET}) \tag{103}$$

$$\mathbb{a}_{mid,ET} = \frac{a_{fIPMf}(N_0^*) + a_{fIPMf}(N_{end})}{2} + \mathbb{a}_{n,MT2} \tag{104}$$

where $\mathbb{a}_{mid,ET}$ is the crack size at the midpoint of the evaluation interval, which, in this case, spans the entire test. The $\mathbb{a}_{n,MT2}$ is used here because the evaluation refers to the MT No. 2 specimen; in general, one may write $\mathbb{a}_n$.

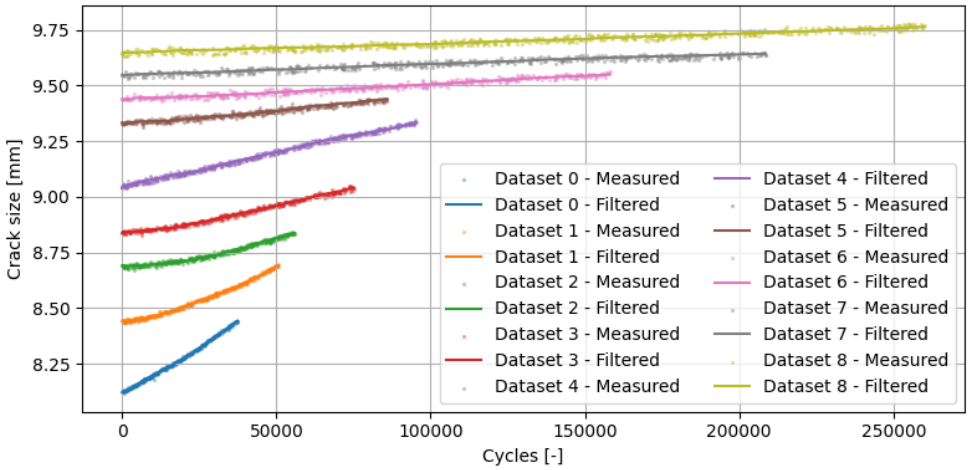

Fig. 51: MT No. 2 datasets No. 0–8 with measured and filtered crack size values obtained at virtual extensometers' length $l_{ve} = 1.3\ mm$. The vertical axis represents crack size (crack-length value from fIPM/fIPMf + corresponding notch length). Data are plotted from N_0^* and offset to zero.

For the MT No. 4 dataset, the larger crack extension during the test made it possible to extract multiple

points for the $da/dN - K_{max}(\mathbb{a})$ dependence. The cycle interval boundaries N_j^{**} were determined according to equation (85), with the following modifications:

- N_G^* was replaced by N_G^{**},
- $\mathcal{Y} = fIPMf$, $\mathcal{Z} = FCGR$, $N_U = 1$,
- $N_0^{**} = 5000$,
- and $\Delta a_{FCGR}^{thr} = 0.4\,mm$, which yielded 10 datapoints.

The FCGR for each interval j was then calculated as:

$$\left(\frac{da}{dN}\right)_{fIPMf,j} = \frac{a_{fIPMf}(N_j^{**}) - a_{fIPMf}(N_{j-1}^{**})}{N_j^{**} - N_{j-1}^{**}}, j \in \{1, \dots, G\} \tag{105}$$

and the corresponding maximum SIF as:

$$K_{max,j} = (1-R)^{-1}\Delta K_{MT}(\mathbb{a}_{mid,PT,j}), j \in \{1, \dots, G\} \tag{106}$$

$$\mathbb{a}_{mid,PT,j} = \frac{a_{fIPMf}(N_{j-1}^{**}) + a_{fIPMf}(N_j^{**})}{2} + \mathbb{a}_{n,MT4}, j \in \{1, \dots, G\} \tag{107}$$

where $\mathbb{a}_{mid,PT,j}$ is the crack size at the midpoint of the evaluation interval j, which covers only part of the test. The $\mathbb{a}_{n,MT4}$ is used here because the evaluation refers to the MT No. 4 specimen; in general, one may write $\mathbb{a}_n$. Here, G denotes the most recent update-event index (see subsections 6.2.3.2 – 6.2.3.3), and thus equals the number of completed evaluation intervals produced by the event-driven rule (85).

Additionally, only intervals with $N_G^{**} < 450000$ were considered. This restriction was applied to exclude the later part of the dataset to ensure comparability across the entire range of l_{ve} values. As demonstrated in Fig. 52, this part of the data showed a marked reduction in FCGR as well as in the maximum measured crack size. Closer inspection of the specimen images revealed that the crack path deviated slightly from a straight line, causing surface discontinuities to interfere with the correlation subsets at the VE endpoints.

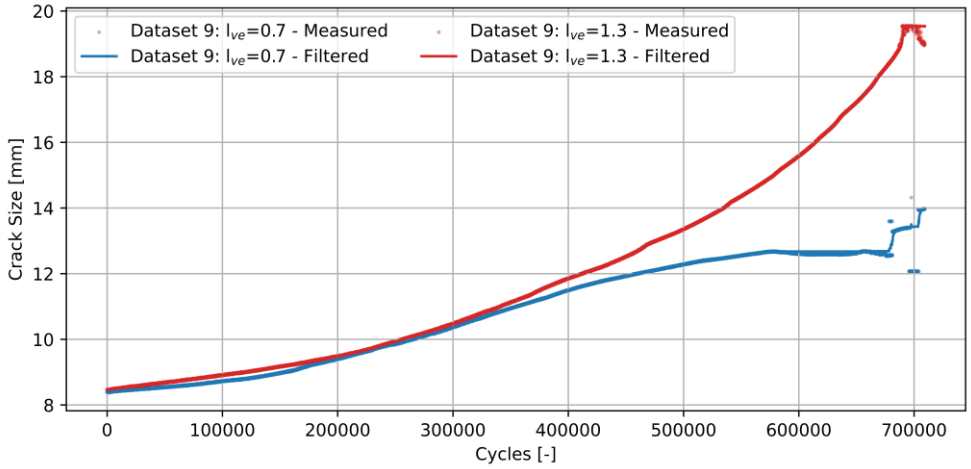

Fig. 52: Measured and filtered crack size values for the MT No. 4. The vertical axis represents crack size (crack-length value from fIPM/fIPMf + corresponding notch length). Data are plotted from N_0^* and offset to zero.

This phenomenon was proposed in section 4.6 as a potential undesirable effect when considering $l_{ve} <$

1.5. Here, it became noticeable for $l_{ve} < 1.3$, where it progressively shifted the saturation point of the FCGR curve—i.e., the plateau indicating no further crack growth in fIPMf—towards lower cycle counts and crack size values. This limitation should be kept in mind by users of the method.

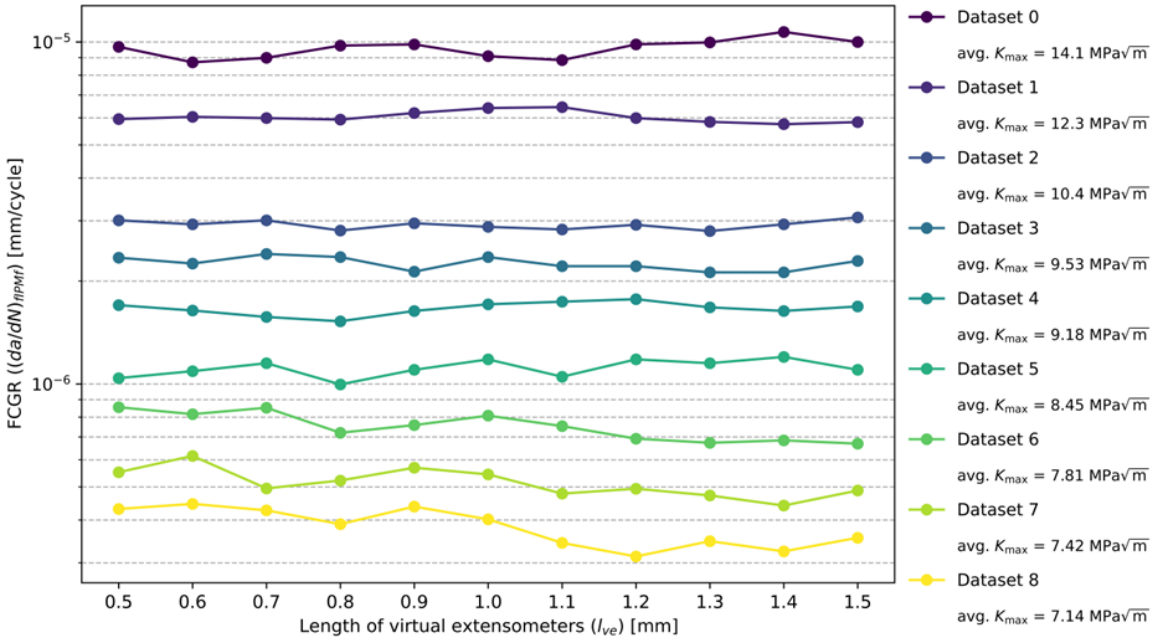

Fig. 53: Crack growth rate as a function of virtual extensometers' length (l_{ve}) for MT No. 2 datasets. The average K_{max} value across all l_{ve} cases is indicated for each dataset.

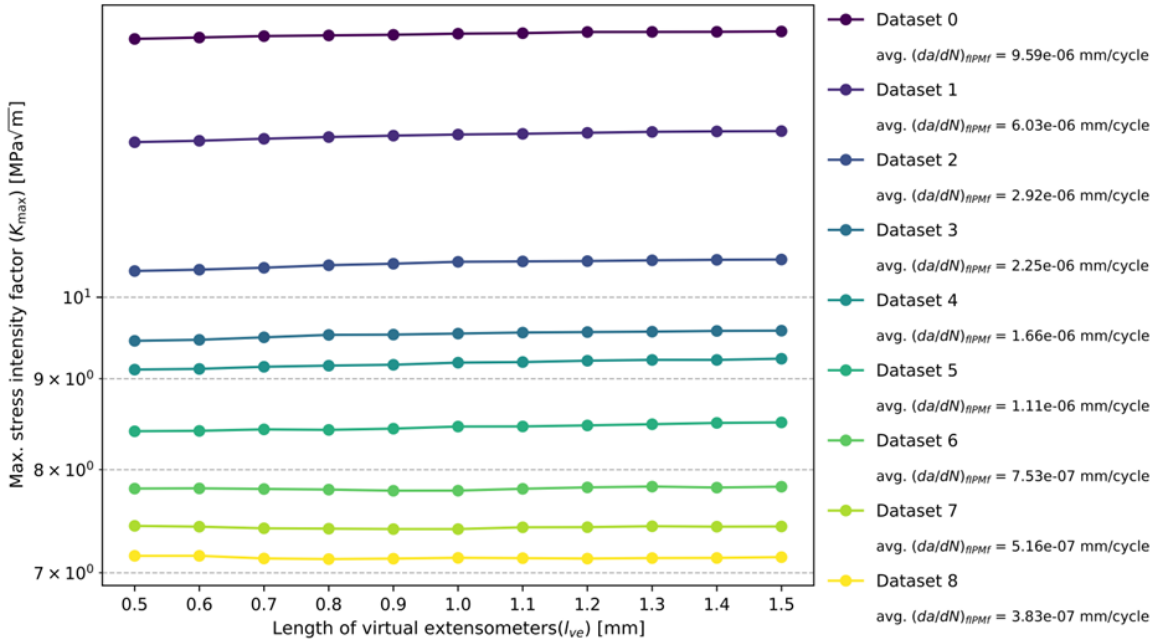

Fig. 54: Maximum stress intensity factor K_{max} as a function of virtual extensometers' length l_{ve} for MT No. 2 datasets. Each dataset also shows the average da/dN across all l_{ve} cases.

6.3.3 Influence of Virtual Extensometers' Length and Error Analysis

For the MT No. 2 sample, which covers a wide range of applied loads, the influence of the VEs' length on the measured FCGR values was first evaluated (Fig. 53). For datasets No. 0–5, no significant dependence was observed. However, for datasets No. 6–8, tested at lower loads, the FCGR values

exhibited an increasing trend toward smaller l_{ve}.

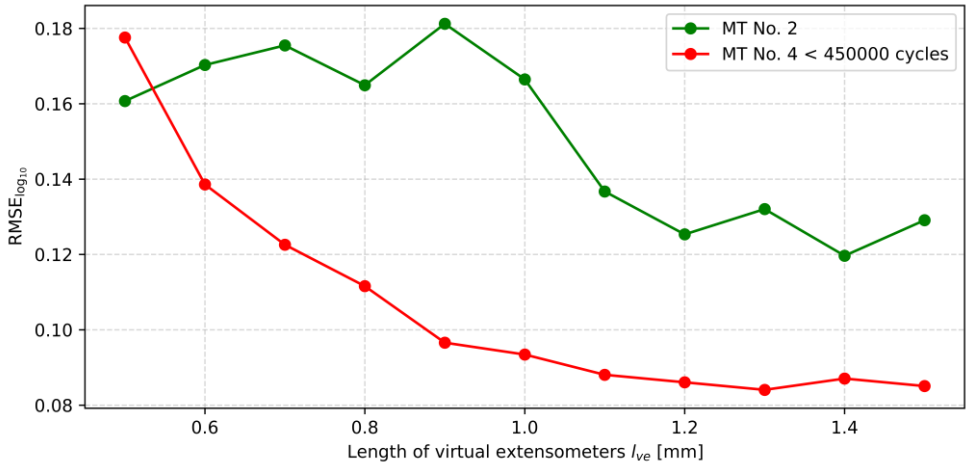

Fig. 55: Comparison of fIPMf (fast Inflection point method filtered) crack growth rates with values predicted by the NASGRO equation from baseline data, for various virtual extensometers' lengths.

The dependence of the calculated K_{max} on the VEs' length was then assessed (Fig. 54). For datasets No. 0–5, corresponding to higher loads, K_{max} decreased gradually from $l_{ve} = 1.5\ mm$, with the decline becoming more pronounced for $l_{ve} < 1\ mm$. Since this trend is not visible in Fig. 53 (at least not for datasets No. 0–4), it suggests that lowering l_{ve} leads to a systematic reduction in the predicted crack length at higher loads. This tendency persists across the entire interval in a relatively uniform manner—thereby keeping the crack growth rate itself unaffected by the trend. For datasets No. 6–8, the values remained relatively constant, with a slight increase at smaller l_{ve}.

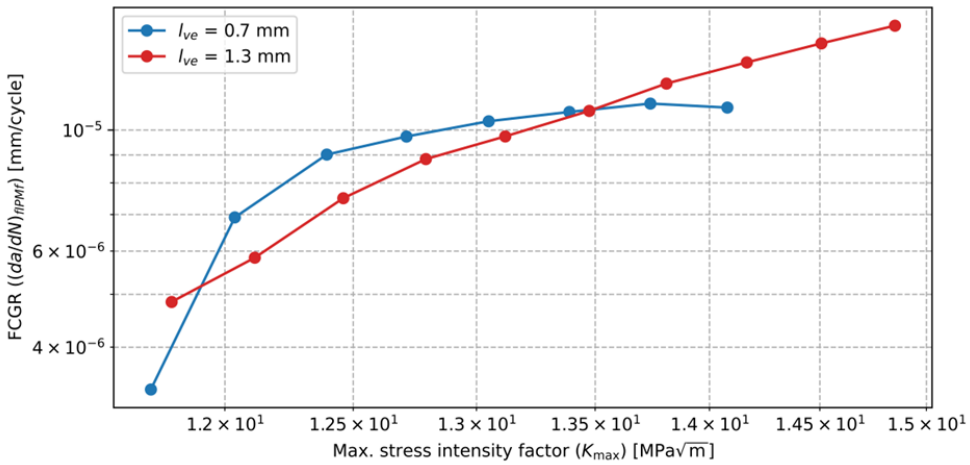

Fig. 56: Crack growth rate evaluation for the MT No. 4 sample (restricted to crack growth below 450000 cycles)

These datapoints, together with those obtained for MT No. 4, were compared with the baseline NASGRO curve using the RMSE in log_{10} space defined as:

$$RMSE_{log_{10}} = \sqrt{\frac{1}{N_{dp}} \sum_{k=1}^{N_{dp}} \left(log_{10}\left(\frac{da}{dN}\right)_{fIPMf}(K_{max,k}) - log_{10}\left(\frac{da}{dN}\right)_{NG}(K_{max,k}) \right)^2} \qquad (108)$$

where N_{dp} is the total number of fIPMf data points used in the comparison (for MT No. 2, the sum over

all considered datasets; for MT No. 4, the interval-split points from the single dataset). $K_{max,k}$ is obtained at the appropriate mid-interval crack sizes, using definitions (103) and (106).

The results (Fig. 55) show that for MT No. 2, the error increased when $l_{ve} < 1.1\ mm$, matching the rise in FCGR in datasets No. 6–8 (Fig. 53). For MT No. 4, the overall error was smaller, likely due to larger Δa used in the evaluation, but it increased steadily toward the end of the dataset (Fig. 55), reflecting the crack path deviation and subset interference as described in subsection 6.3.2.

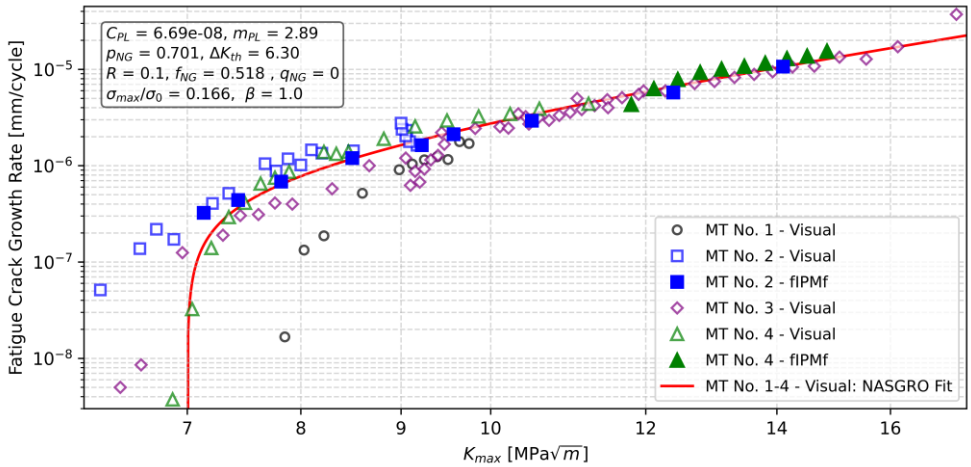

Fig. 57: Raw baseline data measured with VIM (Visual inspection method) and tests evaluated by fIPMf (fast Inflection point method filtered), shown together with the NASGRO fit using all VIM datasets. Units: $C_{PL}\ \left[mm\left(MPa\sqrt{m}\right)^{-m_{PL}}\right]$ *for mm/cycle and for* $\Delta K_{th}\ \left[MPa\sqrt{m}\right]$.

Overall, the results look very promising across the tested range. The best error value corresponds to a deviation of approximately 21% from the baseline [31], while the worst indicates about 51%. However, qualitative comparison of the $da/dN - K_{max}$(a) curves (Fig. 56) shows, for example at $l_{ve} = 0.7\ mm$, that for lower values of l_{ve} the results deviate from the expected linear shape quite noticeably, indicating that the measurement is not fundamentally correct. This finding is consistent with the observations in subsection 6.3.2, where it was shown that crack–subset interference can shift the saturation point of the curve to lower crack sizes and cycle counts. The quantitative overview of residual errors and approximate deviations, including the datasets obtained using VIM, is provided in Tab. 19.

Tab. 19: Overview of $RMSE_{log_{10}}$ *(root mean square error) and deviations from baseline (NASGRO).*

	fIPMf [a], $l_{ve} = 1.3\ mm$ [b]		*VIM* [c]			
MT No.	*2*	*4*	*1*	*2*	*3*	*4*
$RMSE_{log_{10}}$	*0.120*	*0.084*	*0.613*	*0.185*	*0.152*	*0.121*
Deviation [%]	≅ 32	≅ 21	≅ 310	≅ 53	≅ 42	≅ 32

[a] fast Inflection point method filtered; [b] virtual extensometers' length; [c] Visual inspection method

Based on these findings, a recommended value of $l_{ve,r} = 1.3\ mm$ was chosen as the midpoint of the stable interval $1.1 \leq l_{ve} \leq 1.5$. Selecting the higher end of this range is prudent, as it reduces the risk of crack-subset interference. Finally, datapoints for $l_{ve,r} = 1.3\ mm$ are plotted alongside the baseline

[31] calculated as $100\left(10^{RMSE_{log_{10}}} - 1\right)$

and NASGRO predictions in Fig. 57.

6.3.4 Summary and Conclusion

The validation carried out in this chapter shows that the proposed fIPMf method provides reliable results for FCGR assessment and performs on a comparable level with the established VIM baseline. The method was tested across a range of VEs' lengths, and the outcomes confirm that it maintains good accuracy and robustness within a broad interval.

While excessively small VEs' lengths were shown to produce distortions due to crack–subset interference, a practical working range was identified in which the measurements remain stable and consistent. Within this range, the deviations from baseline data remain acceptable, confirming that the approach can be applied for fatigue crack growth evaluation on data obtained during running tests.

Taken together, the results indicate that the fIPMf method is suitable for crack length and growth rate measurements and delivers accuracy comparable to established techniques. This makes it a practical option for further applications in experimental fatigue analysis.

7 Additional Measurements

To complement the previous fIPMf-based measurements performed on MT specimens, two additional CT specimens were tested and evaluated.

7.1 Experimental Program for Additional Data Acquisition

The experimental program for this chapter (hereafter, the *current EP)* closely follows the *Experimental program for Data Acquisition* in section 6.1 (hereafter, the *previous EP*). In what follows, the previous EP is referenced to highlight the changes introduced here.

Two CT specimens prepared in accordance with [19] were used: S235(JR) and AISI 304L, hereafter abbreviated as CTCS and CTSS, respectively. Both specimens had identical dimensions $W = 50\,mm$ and $B = 10\,mm$. The corresponding notch lengths were: $a_{n,CTCS} = 12.62\,mm$ (straight-through) and $a_{n,CTSS} = 12.53\,mm$ (chevron). A speckle pattern was applied over the entire ROI.

Tests were performed on an Amsler 20 HFP 5100 resonant pulsator. Compared with the previous EP, a telecentric lens (WWK10-110-111, $m_{opt} = 1$) with a viewing area of approximately $14.1 \times 7.5\,mm$. was used. A green $20\,W$ LED spotlight replaced the two high-power light sources used previously. Although the rated power was lower, focusing the beam on the ROI provided comparable illumination. It also reduced glare in the laboratory, making the setup less distracting for other personnel.

For both specimens, a *K*-increasing test was conducted with a single reduction in load. The stress ratio was held constant at $R = 0.1$. The cycling frequency was $78 - 92\,Hz$. Tab. 20 summarizes the test.

Tab. 20: Overview of force amplitudes (P_a), n_{sync}, and the total number of cycles ($N_{overall}$) for each dataset collected on the CT S235 (CTCS) and CT AISI 304L (CTSS) samples

	$P_a\ [kN]$	$N_{overall}\ [10^3]$	$n_{sync}\ [-]$
CTCS Dataset 0	3.25	260	100
CTCS Dataset 1	2.75	134	100
CTSS Dataset 0	3.25	89	50
CTSS Dataset 1	2.75	87	50

Note on deviations from ASTM E647 [19]:

- The change in P_{max} between consecutive datasets exceeds the recommended 10%
- Single measured crack size is used rather than the recommended average of two measurements.

7.2 Data Processing

The DIC settings matched the previous EP, except that *Maximal shift of the point* across all datasets was $67\,px$ (corresponding to a displacement of $234\,\mu m$). Following the recommendation in subsection 6.3.3, $l_{ve} = 1.3\,mm$ was used. Due to the smaller FoV, $w_{ve} = 12.5\,mm$ and $n_{ve} = 168$.

Crack lengths were extracted using the fIPMf method presented in Chapter 6. For SIF evaluation, the notch length was added to the measured crack lengths to obtain the crack sizes (see Fig. 58).

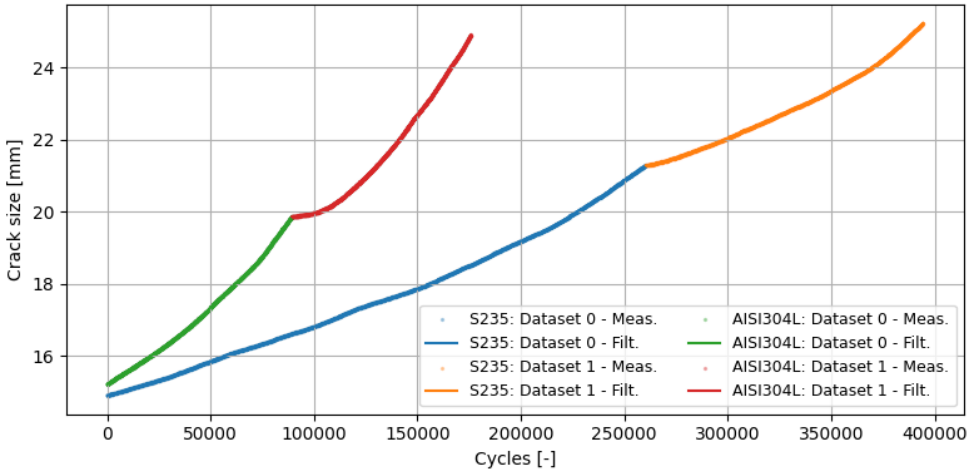

Fig. 58: Measured and filtered crack size values for the CT specimens of S235 and AISI 304L over two consecutive datasets, with the load reduced in the second dataset. The vertical axis represents crack size (crack-length value from fIPMf + corresponding notch length). Data are plotted from $N_0^* = 5000$ and offset to zero.

FCGR was evaluated according to equation (105); interval boundaries were determined using equation (85). The only difference from subsection 6.3.2 was $\Delta a_{FCGR}^{thr} = 0.25\ mm$, which corresponds to $min(\Delta a_r)$ [19]. The corresponding SIF ranges were then obtained:

$$\Delta K_{k,j}(a) = \Delta K_{CT}\left(a_{mid,PT,k,j}\right), j \in \{1, \dots, G\}, k \in \{CTCS, CTSS\} \tag{109}$$

$$a_{mid,PT,k,j} = \frac{a_{fIPMf,k}\left(N_{k,j-1}^{**}\right) + a_{fIPMf,k}\left(N_{k,j}^{**}\right)}{2} + a_{n,k}, j \in \{1, \dots, G\}, k \in \{CTCS, CTSS\} \tag{110}$$

After the load reduction, the CLI of $\Delta a_{NE} = 0.5\ mm$ was excluded from the FCGR evaluation, consistent with $min(\Delta a_{KD,r})$ [19].

7.3 Results

The resulting data point of CTCS and CTSS are plotted in Fig. 59 together with Paris law fits for each specimen separately.

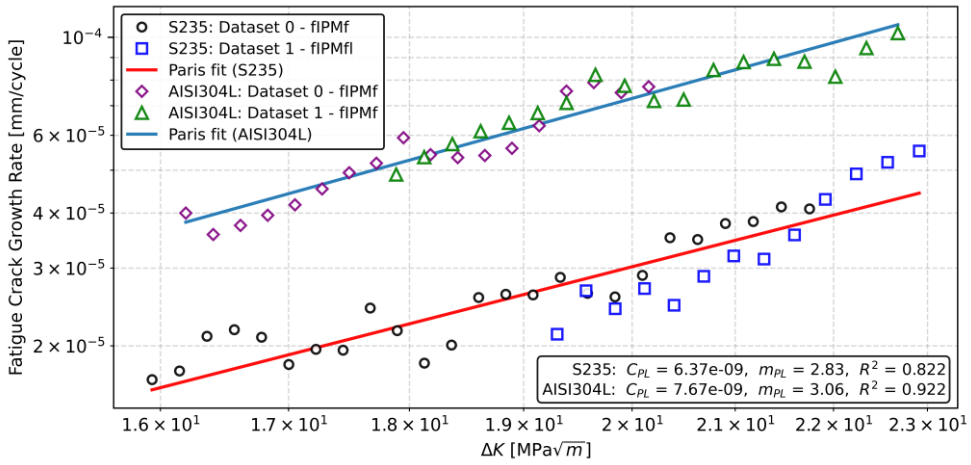

Fig. 59: Data points from tests of CT specimens of S235 and AISI 304L evaluated using fIPMf (fast Inflection point method filtered), shown with the Paris law fit for each specimen separately.

Because no baseline from the same specimens was available, the results were compared with values reported in the literature. Tab. 21 compares the Paris-law coefficients obtained for CTCS with published data for S235; since W, B, and R differ among sources, these inputs are listed for reference.

For CTCS, the Paris coefficients do not differ substantially from the literature, particularly for studies with the same thickness. They also align closely with the coefficients obtained in subsection 6.3.1 using the NASGRO equation on multiple MT datasets. Slightly higher values for the MT specimen can be attributed to its lower thickness (lower constraint), which tends to promote slightly faster crack growth.

Tab. 21. Input parameters (grey) together with the Paris-law coefficients C_{PL} and m_{PL}, and the coefficient of determination R^2 for fatigue tests on S235 CT reported in the literature and obtained in this work (CTCS). Crack closure is not considered.

Source	$\{W, B\}$ $[mm]$	R $[-]$	$C_{PL}\left[mm\left(MPa\sqrt{m}\right)^{-m_{PL}}\right]$	m_{PL} $[-]$	R^2 $[-]$
CTCS	{50,10}	0.10	6.37×10^{-9}	2.83	0.822
MT NASGRO (subsection 6.3.1)	{60,6}	0.10	11.0×10^{-9}	2.89	N/A
(2022, Comlekci et al.) [146][a]	{40,10}	0.00	3.25×10^{-8}	2.53	N/A
(2020, Seitl et al.) [147]	{50,10}	0.10	2.00×10^{-9}	3.26	0.910
(Carvalho et al.) [148][b]	{50,4}	0.01	7.79×10^{-10}	3.71	0.988
(Carvalho et al.) [148][b]	{50,4}	0.50	2.24×10^{-10}	4.00	0.991

[a] The original unit of C_{PL} in the article was $m\left(MPa\sqrt{m}\right)^{-m_{PL}}$, so the value was multiplied by 10^3 to express it in $mm\left(MPa\sqrt{m}\right)^{-m_{PL}}$, consistent with the units used in this work.

[b] The original unit of C_{PL} in the article was $mm(N(mm)^{-1.5})^{-m_{PL}}$, so the value was multiplied by $10^{1.5m_{PL}}$ to express it in $mm\left(MPa\sqrt{m}\right)^{-m_{PL}}$, consistent with the units used in this work.

For CTSS, the Paris-law constants are listed in Tab. 22 together with literature values for AISI 304L under comparable conditions. Because the published studies do not always share the same W, B, and R, these parameters are reported for context. In this case, the crack-growth curve for CTSS is noticeably less steep than most literature datasets. When focusing on directly comparable conditions ($B = 10\ mm$ and $R = 0.1$), the discrepancy is pronounced, especially relative to [151].

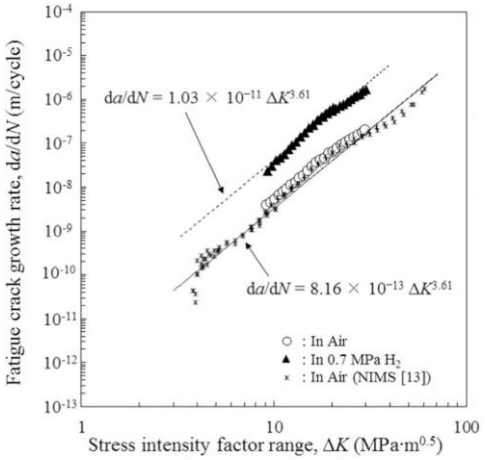

Fig. 60: Fatigue crack growth rate plot [152] showing a steeper crack growth in the interval $\Delta K \in (10, {\sim}18)\ MPa\sqrt{m}$ followed by a noticeably less steep slope in $\Delta K \in ({\sim}18{,}30)\ MPa\sqrt{m}$.

Tab. 22: Input parameters (grey) together with the Paris law coefficients C_{PL} and m_{PL} and the coefficient of determination R^2 for fatigue tests on CT samples from AISI 304L material found in literature and performed within this work (CTCS). The crack closure is not considered if not directly indicated.

Source	$\{W, B\}$ $[mm]$	R $[-]$	$C_{PL}\left[mm\left(MPa\sqrt{m}\right)^{-m_{PL}}\right]$	m_{PL} $[-]$	R^2 $[-]$
CTSS	{50,10}	0.10	7.67×10^{-9}	3.06	0.922
(2009, Kalnaus et al.) [149] (crack closure considered)	{31,3.8}	{0.1, 0.2, 0.5, 0.75,0.85}	1.25×10^{-10}	3.97	N/A
(2023, Subasic et al.) [150][a] rolling direction	{50,13}	-1	2.25×10^{-9}	3.34	N/A
(2023, Subasic et al.) [150][a] transversal direction	{50,13}	-1	1.572×10^{-9}	3.43	N/A
(2022, Seitl et al.) [151][b] (1.4306)	{50,10}	0.1	3.00×10^{-11}	4.7	0.480
(2022, Seitl et al.) [151][c] (1.4307)	{50,10}	0.1	2.00×10^{-11}	4.98	0.650
MT No. 2 and MT No. 4: Paris-law fit in Region I[d]	{60,6}	0.10	3.27×10^{-11}	5.07	0.988
(2019, Nagaishi et al.) [152]	{51,10}	0.1	8.16×10^{-10}	3.61	N/A

[a] The original unit of C_{PL} in the article was $m\left(MPa\sqrt{m}\right)^{-m_{PL}}$, so the value was multiplied by 10^3 to express it in $mm\left(MPa\sqrt{m}\right)^{-m_{PL}}$, consistent with the units used in this work.

[b] The original unit of C_{PL} in the article was reported as $\frac{mm}{cycle} MPa\sqrt{m}$, which is inconsistent with the Paris law used in both the article and this work (equation (38)). Therefore, the numerical value of C_{PL} is regarded as correct, and the unit in the table is considered an error.

[c] The original unit of C_{PL} in the article was reported as $\frac{m}{cycle} MPa\sqrt{m}$, which is inconsistent with the Paris law used in both the article and this work (equation (38)). Therefore, the numerical value of C_{PL} is regarded as correct, unit in the table is considered an error, with the correct unit being $m\left(MPa\sqrt{m}\right)^{-m_{PL}}$. However, evaluating the Paris law with the reported constants at $\Delta K = 10\ MPa\sqrt{m}$ and comparing it with the $da/dN - \Delta K$ plot shows a discrepancy of three orders of magnitude. Therefore, the table likely contains an additional unit error, and the correct unit should be $mm\left(MPa\sqrt{m}\right)^{-m_{PL}}$, consistent with the values used in this work.

[d] Included to illustrate the consequences of applying the Paris law in Region I (near-threshold), where it is not valid (see subsection 3.5.2). Material: 235

A closer inspection of the source curves shows that in [152] (where the discrepancy is smaller), the interval $\Delta K \in (10, \sim 18)\ MPa\sqrt{m}$ exhibits a steeper $da/dN - \Delta K$ slope than $\Delta K \in (\sim 18{,}30)\ MPa\sqrt{m}$ for *In Air* datasets (Fig. 60). The CTSS measurements correspond more closely to the latter interval, which helps explain the observed difference.

In the second study with comparable inputs [151], where the difference is larger, the $da/dN - \Delta K$ plot for 1.4307 (Fig. 61) uses $\Delta K \in (\sim 4.5, \sim 10.5)\ MPa\sqrt{m}$ (for $B = 10mm$). The very low FCGR near the lower bound suggests proximity to ΔK_{th}, implying that a non-negligible portion of the data used for the Paris fit lies in the near-threshold Region I (see subsection 3.5.2), where the Paris law does not apply. A similar observation holds for 1.4306.

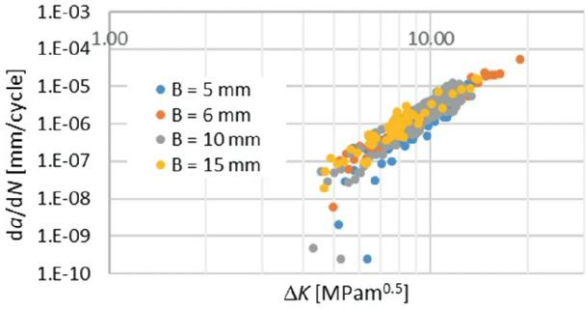

Fig. 61: Fatigue crack growth rate plot for AISI 304L (1.4307, $B = 10\ mm$) [151] showing data in the interval $\Delta K = (\sim 4.5, \sim 10.5)\ MPa\sqrt{m}$, with many points near the (assumed – see the discussion in section 7.3) ΔK_{th} indicating that they fall within Region I (see subsection 3.5.2), where the Paris law does not apply.

This remains a hypothesis, as the threshold value is not reported in the article. However, when near-threshold data are intentionally included in a Paris fit (see Fig. 62 for MT No. 2 and MT No. 4, where ΔK_{th} is known (subsection 6.3.1)), similarly high slope is obtained—even for a different material. Therefore, the results from [151] are not suitable for direct comparison with CTSS.

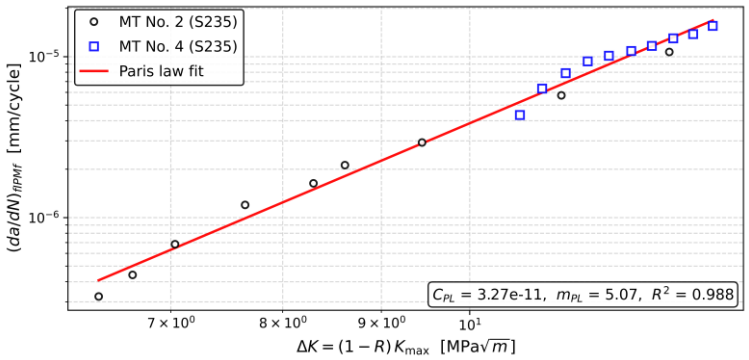

Fig. 62: Example of a Paris-law fit to data in the near-threshold Region I (see subsection 3.5.2), where the Paris law does not apply.

7.4 Summary and conclusion

This chapter adds two CT datasets—S235JR (CTCS) and AISI 304L (CTSS)—to complement earlier MT-based fIPMf measurements. The setup mirrors the previous program, using telecentric optics and focused LED lighting; tests followed a K-increasing regimen with one load reduction at $R = 0.1$. Crack lengths were extracted using fIPMf and converted to crack size for SIF/FCGR evaluation, using the same intervalization and exclusion rules as the prior methodology, with minor documented deviations from ASTM E647.

The CTCS results show Paris-region behavior in line with the literature and, importantly, with the earlier NASGRO evaluation on MT datasets; modest differences likely reflect thickness-related constraint effects. Conversely, the CTSS fit is less steep than many published datasets under nominally comparable conditions. Detailed examination of the cited sources indicates that differing ΔK windows and the inclusion of near-threshold data can bias Paris fits, rendering those sources not directly comparable.

8. Methodology Summary & Implementation Guide

This chapter consolidates the thesis into a single, implementable workflow for real-time crack length and fatigue crack growth rate (FCGR) assessment using digital image correlation (DIC). It is written so that a reader can deploy the method without having to re-read earlier chapters in detail, while still pointing to the exact places where key definitions, settings and justifications are given.

At a glance: The methodology couples (i) a practical, experimental setup for continuous imaging under cyclic loading, (ii) 1D DIC extraction of crack opening displacement projection (CODP) curves, (iii) the Inflection point method (IPM) with code-level and scheme-level accelerations, and (iv) a lightweight, adaptive Kalman filter with a soft-monotonicity safeguard—referred to as fIPMf (fast IPM, filtered)—to yield stable crack-length histories at ≈20 FPS (frames per second) on the reported hardware, with markedly lower load-dependence than threshold methods. See the algorithmic backbone in Chapters 4–6, esp. sections 4.3–4.6, 5.2 and 6.2.

The resulting throughput ≈ 20 FPS (section 4.6 and subsection 5.2.5) matches STM (Strain threshold method) and is approximately an order of magnitude faster than full-field DIC at similar resolution windows (see subsection 5.2.6).

In addition, the thesis provides a concise, practically oriented theoretical framework (Chapter 3)—a summary of key concepts and relationships sufficient for routine yet informed application of the proposed methodology.

8.1 Instrumentation and Specimen Preparation

8.1.1 Optics & Cameras

- Global-shutter machine-vision camera. Use a monochrome CCD/CMOS camera with low noise, high dynamic range, and high quantum efficiency; a global shutter is essential to avoid motion-induced distortion during high-speed cycling (rolling shutter is not suitable) (see subsection 3.1.1.1).
- Telecentric lens (TL). Choose a TL to eliminate perspective (parallax) errors and minimize distortion (see subsection 3.1.1.2). Practical trade-offs: higher f-number (lower lens speed) and shallow depth of field (DoF); larger field of view (FoV) requires a larger-diameter TL.
- Reference working configuration used here. FLIR 8.9 MP global-shutter camera + TC3MHR016-C telecentric at 0.85× magnification; FoV ≈16.7 × 8.8 mm. Use a focusing slide to fine-adjust the working distance, given the TL's shallow DoF (see subsection 4.1.2).
- Robust mechanical mounting. Mount cameras and lenses on a rigid, well-damped structure (preferably decoupled from the cycling machine frame). Ambient vibrations can introduce significant errors, especially with a compliant camera fixture (see subsection 3.1.8).
- It is generally recommended to pre-heat the camera for 1–2 h to a thermal steady state before calibration/measurement (see subsection 3.1.8).

8.1.2 Illumination

- Intense, cool, even light. Provide strong LED (light-emitting diode) lighting to support short (sub-ms) exposure times that suppress motion blur; LEDs also minimize heating of

optics/sensor. Avoid over-illumination that saturates pixels and keep lighting stable throughout the test. In cases of extremely short shutters, strobed light is an option, although it might be unpleasant for laboratory technicians.

- Exposure guideline. The thesis used 0.5 ms exposure (0.4 ms in the later program) specifically to prevent motion blur at resonance-test frequencies. Two 50 W LED sources placed close to the specimen ensured adequate SNR at these shutter speeds. Even more convenient would be using spotlights, which focus the light on a smaller area and thus would not dazzle laboratory technicians.

8.1.3 Specimen Surface (DIC Readiness)

- Apply a high-contrast speckle over the entire region of interest (see Fig. 44, subsection 6.1.1).
- Do not leave a polished band. The polished mirror band was only for validation (same-side VIM (Visual inspection method) and DIC) and is not required by the final methodology.
- Speckle quality. Aim at ~50% coverage; speckle size 3×3 to 7×7 px; pattern should be stable and non-glossy (see subsection 3.1.6).
- Practical note: batch preparation of speckles is fast (in the low tens of minutes for several specimens) and no more demanding than polishing for VIM.

8.1.4 Calibration and Reference Frame

- Perform a 2D DIC calibration prior to testing to assign pixel scale (mm/px) (see subsection 3.1.4—for a TL, it is usually sufficient to perform calibration via the "known-dimension" approach (see subsection 4.1.3), as this kind of lens does not suffer from parallax error (see subsection 3.1.1.2).
- Optionally, perform calibration using a calibration grid, which also allows lens-distortion correction and automatic axis definition (see subsection 3.1.4) to further enhance the accuracy of the measurement.
- Acquire a reference (undeformed) frame of the specimen for correlation before or at the start of the test prior to applying load (see subsection 4.1.3).

8.2 Acquisition under Cyclic Loading

8.2.1 Synchronization & Timing

- Use a synchronization device to trigger image capture every n_{sync} cycles and at a consistent phase near P_{max}, when the crack is maximally open (Fig. 45; subsection 6.1.3).
- During ramp-up, images may already be recorded; although small displacement levels make timing errors more visible, the processing pipeline is built to exclude this segment (see the Kalman filter update rule in subsections 6.2.3.2 – 6.2.3.3).

8.2.2 Frame Rate & Frequency

- On the reported resonant machines, cycling frequencies during the tests were in the ~45–90 Hz range; analyzing every n_{sync}^{th} cycle (typical n_{sync} in this thesis was 50 – 100) produced smooth crack length histories with practical throughput (see subsections 4.1.3, 5.2.6 and 6.1.3).

8.3 Multi-Camera Layouts for FCGR Compliance

To comply with the FCGR (da/dN) standards, for instance ASTM E647 [19], the crack length used for FCGR evaluation should be averaged across all present growing cracks, as the through-thickness asymmetry and left–right differences can bias single-side readings. This averaging across all present cracks was demonstrated in the VIM baseline datasets in subsection 6.3.1. Although the experimental procedures used in this thesis measured only one crack length, the thesis explicitly notes that using a single measured crack length is a deviation from the standard's recommendation (subsection 6.1.3).

8.3.1 Recommendations to comply with standards:

- Use a multi-camera setup:
  - Compact tension specimen: instrument both faces → 2 cameras (one per face)
  - Middle tension specimen: instrument both faces of both cracks → 4 cameras (one per face per crack)
- Synchronize the cameras (can be triggered by the same synchronization device) to capture images at moments described here in subsection 8.2.1.
- Process each stream independently with the same configuration and settings (in parallel on different processor cores).
- Then, for FCGR evaluation, average the resulting crack lengths across all present growing cracks per [19].

8.4 Data Extraction by 1D DIC

Use virtual extensometers (VEs) along the anticipated crack path to extract the CODP curves efficiently in real time using DIC. This is adequate when the standard assumes straight-line propagation and out-of-plane motion is negligible (see section 2.3, the introduction at the beginning of Chapter 3, section 3.2, and subsection 4.2.2).

8.4.1 User-Selected DIC settings

- Number of VEs (n_{ve}) and span (w_{ve}). To ensure the performance of the method, it is recommended to use $w_{ve,r} \in \langle 10.0, 14.5 \rangle\, mm$ and then calculate n_{ve} based on the recommended VE spatial frequency $f_{ve,r} \in \langle 11, 14 \rangle\, mm^{-1}$ (see section 4.6). The first VE should be placed so that it passes through the notch tip.
- VE length (l_{ve}). Recommended $l_{ve,r} = 1.3\, mm$ as the midpoint of the stable interval $1.1 \leq l_{ve} \leq 1.5\, mm$. Adhering to this recommendation reduces the risk of crack-subset interference, which is discussed in subsections 6.3.2 – 6.3.3.
- Subset size and aspect ratio. Beyond the DIC settings discussed in subsections 4.2.2 and 6.1.1, subset choice must reflect speckle size/density (see subsection 3.1.6) and the subset-size trade-offs (see subsection 3.1.5.2). Practical tip validated during IPM development: keep a ~4:1 aspect ratio with the smaller subset dimension along the crack path (see section 4.6). An example used in the thesis: 21×81 px.
- Correlation & interpolation. Use robust, illumination-insensitive criteria (e.g., ZNCC/ZNSSD) and sub-pixel interpolation, consistent with subsections 3.1.5–3.1.5.1.

8.5 fIPMf Crack Length Estimation

- Detect the inflection point on CODP curve via Gaussian process regression to identify the crack tip robustly without thresholds.
- Run the adaptive Kalman filter with soft-monotonic refinement to suppress synchronization-related temporal noise and stabilize the time series.
- The complete, optimized pipeline is given in Fig. 50 (subsection 6.2.6) and builds on the development described in sections and subsections 4.3 – 6.2.5.

8.6 FCGR Evaluation

- From the obtained crack size histories, compute da/dN using the averaged crack length across the synchronized cameras as discussed in subsection 8.3.1.
- Use the recommended intervalization ($\Delta a \geq 0.25\ mm$) per [19] when assembling points for the $da/dN - \Delta K$ (FCGR – stress intensity factor range) curve.
- Practical symbols and relations are summarized in section 3.5.

8.7 Scope, Limitations, Checks & Troubleshooting

8.7.1 Checks Before Test Start

- Mounting and its stability (ensure a rigid, vibration-resistant camera mount; avoid compliant fixtures).
- Camera(s) have been preheated, and the lens is in focus (preheat under measurement conditions for ~1–2 h before calibration)
- Lock any zoom/aperture rings (if present).
- Illumination is uniform and stable; there are no problematic reflections (use polarization filters if needed)
- There are no unnecessary heat sources near the optical path that could disturb the image.
- There is sufficient contrast in the image; the speckle pattern is intact in the region of interest.
- The system is calibrated; an undeformed reference image has been captured.
- DIC and synchronization settings have been applied.
- Viewing window/port is clean (for environmental chambers).
- The enabled camera framerate exceeds that required by the synchronization device.
- Avoid sensor gain; prefer illumination (to prevent noise amplification)
- Confirm applicability: avoid starting with very short cracks ($\lesssim 1.5$ mm) where accuracy degrades.
- Adhere to material scope: methodology is validated for metallic materials.

8.7.2 Checks at the Beginning of the Test

- The acquired images are not blurred; if blurred, shorten exposure and/or increase illumination.
- If blur persists, out-of-plane motion may have moved the specimen surface out of focus. In that case, either limit out-of-plane motion, readjust the focus to encompass the motion, or use a TL with higher DoF if the previous two options do not help or are not applicable.

- Tracked DIC points stick to their expected locations; if points are lost/misplaced, increase subset size and/or adjust correlation/search parameters.
- If recording, verify sustained write speed equals acquisition rate; otherwise use a fast local SSD (solid state drive) and/or increase n_{sync}; check free disk space.

8.7.3 Checks During the Test

- Ensure points are still being tracked—points may be lost due to sudden changes in lighting (unexpected glare) or sample position (e.g., someone trips over cables or bumps the camera); prevent such events.
- The crack is growing straight and does not interfere with correlation subsets (see subsections 6.3.2 – 6.3.3). This can be assessed based on qualitatively incorrect intermediate results or visually by checking the path of the crack in the acquired images (the crack tip will not be visible due to the presence of the speckle pattern, but a certain distance behind it, the crack path will be evident from the cracked paint).
- For long cracks, ensure growth has not reached the VE window edge; fIPMf needs data on both sides of the inflection point (see section 4.6). This can be assessed by the equivalent approach described in the previous bullet point.

8.7.4 Verify After the Test

- Check the crack path for deviation from a straight line; look for interference between the crack and correlation subsets that would bias results (see subsections 6.3.2 – 6.3.3).
- Confirm paint adhesion — no peeling near the crack tip.

9 Conclusion

This thesis set out to develop a robust, real-time DIC (digital image correlation) methodology for measuring fatigue crack length that eliminates the need for threshold tuning—a central weakness of threshold-based approaches such as STM (Strain threshold method), whose thresholds are strongly load-dependent and also vary across materials and individual specimens necessitating recalibration and reducing the comparability of results across specimens. In parallel, it sought to replace labor-intensive stop-and-measure VIM (Visual inspection method) readings, enabling uninterrupted, automated testing, in line with fatigue crack growth rate standards. In addition, the thesis provides a concise, practically oriented theoretical framework (Chapter 3)—a summary of key concepts and relationships sufficient for routine yet informed application of the proposed methodology.

The core contribution is a threshold-free, physics-based estimator—the Inflection-Point Method (IPM)—and its fast, filtered implementation (fIPMf). The workflow first uses DIC to extract a crack opening displacement projection (CODP) curve along the expected crack path. Gaussian process regression (a nonparametric regressor that mitigates spatial DIC noise) then identifies the inflection point on the CODP curve, which corresponds to the crack tip. An adaptive Kalman filter with a soft-monotonicity safeguard suppresses temporal noise arising from synchronization inaccuracies and stabilizes the time series. With the optimized processing scheme (fIPMf), the pipeline reaches approximately 20 frames per second on the reported hardware configuration—matching STM throughput and exceeding full-field DIC by roughly an order of magnitude.

Extensive validation shows the methodology meets the accuracy and robustness requirements for metal fatigue testing. Using stopped-test frames to validate IPM and the underlying inflection-point principle—thereby avoiding the acquisition-timing errors present in running tests, IPM matches the VIM baseline with a root mean square error (RMSE) ≈ 31 μm, whereas STM yields an RMSE of ≈ 274 μm. Crucially, IPM shows negligible sensitivity to load level relative to STM. This validation employed an unprecedented setup that enabled VIM and DIC to be used on the same side of the specimen, thereby eliminating bias from through-thickness crack-growth asymmetry.

Another component of the validation program was performed solely on DIC data acquired during continuously running tests. In this case, fIPMf estimates crack-growth rates within approximately 20–30% of a baseline derived from NASGRO (NASA crack growth rate model/equation)-fitted VIM datasets—comparable to the variability across the VIM datasets themselves.

Sensitivity studies cover both DIC and algorithmic parameters. General guidance is provided for case-specific, user-selected settings (e.g., subset size), while quantitative ranges are given where a robust operating window exists (e.g., number of VEs – virtual extensometers). The influence of VEs' length is examined in depth; a practical working range is identified, and a recommended setting is proposed that balances accuracy and robustness for growth-rate evaluation.

The methodology was applied across multiple metals, specimen geometries (sizes, thicknesses, and types), and load levels. Particular attention was given to load changes due to the STM's sensitivity, supporting routine laboratory use, including K-decreasing (stress intensity factor) tests to determine the threshold ΔK_{th} below which no measurable crack growth occurs.

Regarding scope and limitations, accuracy degrades for very short cracks ($\lesssim$ 1.5 mm) due to low-SNR

(signal-to-noise ratio) DIC-measured displacements near crack initiation. The method also requires data on both sides of the inflection point; therefore, operation near the edge of the VE window is not recommended. Within these bounds, the optimized pipeline achieves the reported frame rate and stability.

Achievements relative to the stated objectives:

1. Create a DIC-based methodology for crack-length measurement: Achieved via the IPM → fIPM → fIPMf workflow, with adaptive fitting and filtering.
2. Validate against a non-DIC baseline (VIM) across materials/sizes/load levels: Completed on paired test programs; the methodology delivers accuracy comparable to VIM in real-time operation.
3. Compare with another DIC method (STM): IPM/fIPMf outperform STM in accuracy, exhibit substantially lower load dependence, and match its throughput.
4. Investigate sensitivity to input parameters: Conducted for DIC parameters (e.g., VE length) and IPM settings, yielding practical recommendations as general guidance and, where applicable, quantitative value ranges.

In conclusion, the thesis delivers a validated, threshold-free, real-time DIC methodology for assessing fatigue crack length and crack growth in metals, avoiding test interruptions, achieving VIM-comparable accuracy during running tests, and surpassing STM with substantially lower sensitivity to load level (despite STM's wide adoption in research and by DIC vendors). The approach combines an online, adaptive pipeline that learns during acquisition and responds to changes, incorporating monotonicity safeguards for continuous operation, thereby eliminating per-test and per-material threshold tuning. In addition, the work validates the inflection-point principle for DIC fatigue testing in metals, demonstrating feasibility under uninterrupted operation. All four objectives were met, establishing a practical foundation for future extensions (e.g., to other material classes) and for deeper automation of fatigue-test workflows.

List of Abbreviations

1D	one-dimensional (DIC, approach)
2D	two-dimensional (DIC, measurement, displacement)
3D	three-dimensional (DIC, crack, displacement)
ACPD	alternating current potential drop (technique)
ASTM	American Society for Testing and Materials
CC	cross-correlation (criterion family)
CCD	charge-coupled device (camera sensor)
CLI	crack length increment
CMOS	complementary metal-oxide semiconductor (camera sensor)
COD	crack opening displacement
CODP	crack opening displacement projection
CT	compact tension (specimen)
CTCS	compact tension sample from construction steel (S235JR) in Chapter 7
CTOD	crack tip opening displacement
CTSS	compact tension sample from stainless steel (AISI 304L) in Chapter 7
DCPD	direct current potential drop (technique)
DIC	digital image correlation (method)
DTM	deformation threshold method
DVC	digital volume correlation (method)
EP	experimental program
FCGR	fatigue crack growth rate
fIPM	fast Inflection point method
fIPMf	fast Inflection point method, filtered
FoV	field of view
FPS	frames per second
FPZ	fracture process zone
GD	Gaussian distribution
GP	Gaussian process
GPR	Gaussian process regression
hpars	hyperparameters
IAE	Innovation-based adaptive estimation
IP	inflection point
IPM	Inflection point method
IPMd	dynamic dataset processed by IPM
IPMs	static dataset processed by IPM
KF	Kalman filter
LED	light-emitting diode
LL	load level
lp	line pair
MA	moving average (filter)
MAE	mean absolute error (metric)
MAPE	mean absolute percentage error (metric)
MSE	mean square error (metric)
MT	middle tension (specimen)
NASA	National Aeronautics and Space Administration
NASGRO	NASA crack-growth equation/model (NASa and GROwth)
NCC	normalized cross-correlation (criterion)
NSSD	normalized sum of squared differences (criterion)

N/A	not available
OH	optimized hyperparameters (storage variable)
P1	Phase 1 of IPM (GPR global)
P2	Phase 2 of IPM (GPR local)
P3	Phase 3 of IPM (GPR smoothing)
RBF	radial basis function (kernel)
RMSE	root mean square error (metric)
ROI	region of interest
SENB	single-edge notch bending (specimen)
SGF	Savitzky–Golay filter
SIF	stress intensity factor
SNR	signal-to-noise ratio
SSD	sum of squared differences (criterion family)
SSD	solid-state drive (storage)
STD	standard-deviation based criterion
std	standard deviation
STM	Strain threshold method
SVR	support vector regression
TL	telecentric lens
VE	virtual extensometer
VIM	Visual inspection method (with a traveling microscope)
WD	working distance
WOL	wedge opening loading (specimen/fixture)
w/ (clo.)	with (considering the effect of crack closure)
w/o (clo.)	without (considering the effect of crack closure
X-FEM	extended finite element method
ZNCC	zero-normalized cross-correlation (criterion)
ZNSSD	zero-normalized sum of squared differences (criterion)

List of Symbols

IPM / fIPM / fIPMf Related

Tab. 23: List of symbols specific to the IPM / fIPM / fIPMf description, development, validation, and comparison

Symbol	*Name / short explanation*	*Units*
a_b	Baseline crack length	mm
a_{bm}	Mid-baseline crack length	mm
a_C	Crack-length criterion value	mm
a_{fIPM}	Crack length resulting from fIPM	mm
a_{fIPMf}	Crack length resulting from fIPMf (KF-corrected)	mm
$\bar{a_{fIPMf}}$	KF-predicted crack length from fIPMf	mm
a_{IPM}	Crack length resulting from IPM	mm
a_P	Preliminary crack length (before acceptance)	mm
$a_{P,inp}$	Stored preliminary crack length from the last accepted iteration	mm
a_S	Crack-length storage variable	mm
$a_{n,MT2}$	Notch length for the MT 2 sample	mm
$a_{n,MT4}$	Notch length for the MT 4 sample	mm
A_c	Reference point at the notch tip	—
B_c	Midpoint between B_{cL} and B_{cR} indicating the crack tip	—
B_{cL}	Left boundary point of the visually reliable crack-tip region	—
B_{cR}	Right boundary point of the visually reliable crack-tip region	—
$CODP(x)$	Crack opening displacement projection curve – measured curve	mm
$CODP_{P1}(x)$	Crack opening displacement projection curve reconstructed via GPR in IPM Phase 1	mm
$CODP_{P2}(x)$	Crack opening displacement projection curve reconstructed via GPR in IPM Phase 2	mm
$CODP_{P3}(x)$	Crack opening displacement projection curve reconstructed via GPR in IPM Phase 3	mm
d_{CL}	Crack-length difference in the STD_{crit} calculation interval	mm
$\overline{d_{CL}}$	Mean crack-length difference over the STD_{crit} calculation interval	mm
$\left(\frac{da}{dN}\right)_{fIPMf}$	FCGR used to construct the $da/dN - K_{max}(a)$ dependence	mm/cycle
f_{ve}	VE spatial frequency	mm^{-1}
$f_{ve,r}$	Recommended VE spatial frequency	mm^{-1}

Symbol	*Name / short explanation*	*Units*
$f_{ve,l,r}$	Recommended lower bound for f_{ve}	mm^{-1}
$f_{ve,u,r}$	Recommended upper bound for f_{ve}	mm^{-1}
F_{dd}	Derivative distinction factor (used in Condition 2)	—
$F_{dd,f}$	Final value of the derivative distinction factor (used in Condition 2)	—
F_{id}	Interval decrement factor for the second P2/P3	—
$F_{id,f}$	Final value of the interval decrement factor for the second P2/P3	—
F_{li}	Localization interval factor (sets nominal length of the localization interval)	—
$F_{li,f}$	Final value of the localization interval factor (sets nominal length of the localization interval)	—
g	Readout-error-corrected baseline used in metrics	mm
G	Count of update events in the event-driven update rule; index/number of the last update event	—
$h_{sub,d}$	Subset height used during IPM development	px
$h_{sub,r}$	Recommended subset height	px
i	Index of the IPM / fIPM / fIPMf iteration	—
$\mathcal{I}$	Localization interval used in P2/P3	mm
$\mathcal{I}_f$	Final localization interval used in P2/P3	mm
$\mathcal{I}_{C1,f}$	Final correction-1 interval	mm
$\mathcal{I}_{C2,f}$	Final correction-2 interval	mm
J	Index of the latest updated value $a_{S,k}$	—
$\mathcal{J}$	Set of indices contained in the interval used to update FCGR in the control input model	—
l_{ct}	Length of crack-tip readout-error band around a_{bm}	mm
l_{ve}	Length of virtual extensometers used in DIC	mm
$l_{ve,d}$	Length of virtual extensometers used in DIC during development	mm
$l_{ve,r}$	Recommended length of virtual extensometers used in DIC	mm
L_{soft}	The length of interval which is used for soft monotonic update rule	—
ℓ_f	Final length scale value in IPM	mm
$\ell_{l,f}$	Lower bound of final length scale value in IPM	mm
$\ell_{u,f}$	Upper bound of final length scale value in IPM	mm
ℓ_{study}	Initial hyperparameters study range for length scale	mm
$\mathcal{L}$	Overall/combined loss function	—

Symbol	*Name / short explanation*	*Units*
m	Local data-decimation level (IPM)	—
m_d	Local data decimation level used in development (IPM)	—
m_f	Final value of local data decimation level	—
MAE	Mean absolute error (of crack length)	mm
MAE_{IPMs}	Mean absolute error of the crack length evaluation on the static IPM dataset using final algorithm-parameter values	mm
MAE_{norm}	Normalized mean absolute error (used in $\mathscr{D}$)	—
$MAPE$	Mean absolute percentage error (of crack length)	%
$MAPE_{IPMs}$	Mean absolute percentage error of the crack length evaluation on the static IPM dataset using final algorithm-parameter values	%
$MAPE_{norm}$	Normalized mean absolute percentage error	—
n	Global data-decimation level (IPM)	—
n_{adapt}	Window length for STD_{crit} calculation	—
n_{CODP}	P1 repetition interval (run GPR-global every n_{CODP} iterations)	—
n_d	Global data decimation level used in development (IPM)	—
n_f	Final value of the global data decimation level	—
n_s	Number of GPR smoothings	—
$n_{s,f}$	Final number of GPR smoothing	—
n_{sync}	Synchronization period – camera is triggered once every n_{sync} cycles to acquire an image for DIC	—
n_{ve}	Number of VEs used in DIC	—
$n_{ve,d}$	Number of VEs used in DIC for IPM development	—
$n_{ve,r}$	Recommended number of VEs used in DIC	—
N_{dp}	Number of datapoints used in comparison metrics	—
N_{tp}	Number of timepoints used in comparison metrics	—
N_U	Decision flag for the event-driven update rule	—
N^*	Cycle count at which the update of FCGR in control input model occurs	—
N_0^*	Input specifying the starting point of the first FCGR update interval in the event-driven update rule	—
N_G^*	Cycle count at which the last update of FCGR in control input model occurred	—
N^{**}	Cycle count at which the FCGR evaluation to obtain a datapoint in $da/dN - K_{max}(\mathbb{a})$ occurs	—

Symbol	*Name / short explanation*	*Units*
N_0^{**}	Input specifying the starting point of the first FCGR interval in the event-driven update rule for evaluating $da/dN - K_{max}(\mathbb{a})$	—
N_G^{**}	Cycle count at which the last FCGR interval in the event-driven update rule for evaluating $da/dN - K_{max}(\mathbb{a})$ ends	—
$\boldsymbol{OH}$	Stored vector for optimized hyperparameters (propagated when P1 is skipped)	—
$\mathcal{P}_{init}$	Initial value of the *a posteriori* error variance	mm^2
Q^{cand}	Candidate value of the process noise variance	—
Q_{init}	Initial value of the process noise variance	mm^2
Q_{max}^{thr}	Maximum value that the process noise variance can take	mm^2
Q_{min}^{thr}	Minimum value that the process noise variance can take	mm^2
$RMSE$	Root mean square error (of crack length)	mm
$RMSE_{IPMs}$	Root mean square error of the crack length evaluation on the static IPM dataset using final algorithm-parameter values	mm
$RMSE_{log_{10}}$	RMSE in log-log coordinates	—
$RMSE_{norm}$	Normalized root mean square error	—
$\mathcal{R}^{cand}$	Candidate value of measurement noise variance	—
R_{init}	Initial value of the measurement noise variance	mm^2
$\mathcal{R}_{max}^{thr}$	Maximum value that the measurement noise variance can take	mm^2
$\mathcal{R}_{min}^{thr}$	Minimum value that the measurement noise variance can take	mm^2
$\mathfrak{N}$	Index meaning *real*	—
STD_{crit}	Adaptive standard-deviation criterion for CLI-based outliers	mm
$w_{sub,d}$	Subset width used in IPM development	px
$w_{sub,r}$	Recommended subset width	px
w_{ve}	CODP window width used for VE extraction	mm
$w_{ve,d}$	CODP window width used for VE extraction in IPM development	mm
$w_{ve,l,r}$	Recommended lower bound for w_{ve}	mm
$w_{ve,r}$	Recommended value of w_{ve}	mm
$w_{ve,u,r}$	Recommended upper bound for w_{ve}	mm
x	Object space coordinate along crack path	mm
x_{A_c}	x-coordinate of point A_c	mm
x_{B_c}	x-coordinate of point B_c	mm
x_{ip1}	Inflection-point location from P1	mm

Symbol	*Name / short explanation*	*Units*
$x_{ip1,inp}$	Stored IP-location guess used in P2/P3 when P1 is skipped	mm
x_{ip2}	Inflection-point location from P2	mm
x_{ip3}	Inflection-point location from P3	mm
$x_{l_{ve}}$	Distance of the virtual extensometer from the notch tip	mm
y	Object space coordinate perpendicular to crack path	mm
$\mathcal{Y}$	Placeholder subscript 1	—
$\mathcal{Z}$	Placeholder subscript 2	—
$\gamma_{\mathcal{R}}$	Forgetting factor for the adaptive $\mathcal{R}$ update in fIPMf	—
γ_Q	Forgetting factor for the adaptive Q update in fIPMf	—
Γ_{bm}	Deviation from the baseline for mid-baseline crack length	mm
Γ_{IPMd}	Deviation from the baseline for crack length from IPM dynamic dataset	mm
Γ_{IPMs}	Deviation from the baseline for crack length from IPM static dataset	mm
Γ_{STM}	Deviation from the baseline for crack length from Strain threshold method	mm
δ_{cl}	Crack-length assessment error for VIM	mm
Δa_{fIPMf}^{thr}	Crack-length increment threshold for fIPMf event-driven update rule	mm
Δa_{FCGR}^{thr}	Crack-length increment threshold for the event-driven update rule used in FCGR evaluation of $da/dN - K_{max}(𝕒)$	mm
$\left.\frac{\Delta a_{fIPMf}}{\Delta N}\right\|_{N_G^*}$	Most recently updated value of FCGR in the KF process model	mm/cycle
Δl_{ve}	Change in length of the virtual extensometer	mm
ΔN^{thr}	Cycle increment threshold for the event-driven update rule	—
ε_{th}	Threshold strain used in Strain threshold method (STM)	%
$\sigma_{n,f}^2$	Final noise level value in IPM	mm²
$\sigma_{n,l,f}^2$	Lower bound of final noise level value in IPM	mm²
$\sigma_{n,u,f}^2$	Upper bound of final noise level value in IPM	mm²
$\sigma_{n,study}^2$	Initial hyperparameters study range for σ^2_n	mm²
τ	Threshold value for soft monotonic update rule	mm

Gaussian Process Regression (GPR)

Tab. 24: List of symbols related to Gaussian process regression (GPR) – general explanation.

Symbol	*Name / short explanation*	*Units*
$\mathcal{D}$	Dataset (size M) of noiseless observations	—
$k(\cdot,\cdot)$	Combined kernel (covariance) function composed of an RBF kernel and a white-noise kernel.	—
$k_w(\cdot,\cdot)$	White-noise kernel function – adds the effect of noise to the diagonal of the training covariance matrix.	—
$\boldsymbol{K}$	Training covariance matrix ($M \times M$)	—
$\boldsymbol{K}^*$	Cross-covariance matrix ($M \times M^*$) used for inference (training vs. test inputs)	—
ℓ	Length-scale hyperparameter of the RBF kernel	—
M	Number of observations	—
M^*	Number of inference (test) inputs	
$p(\cdot)$	Probability distribution (repeated in Tab. 25)	—
s	Observed input	—
s^*	Inference (test) input – a single new input not in $\mathcal{D}$; in formulas appears indexed as s_m^*, $\mathrm{m} \in \{1, \dots, \mathrm{M}^*\}$	—
$\mathcal{S}$	Set of observed inputs (size M)	—
t	Observed output at s	—
$\boldsymbol{t}^*$	Inferred outputs at s^* stacked over $\mathrm{m} \in \{1, \dots, \mathrm{M}^*\}$ (size M^*)	—
$\mathcal{T}$	Set of observed outputs (size M)	—
$\boldsymbol{T}$	Observed outputs stacked as vector (size M)	
σ_n^2	Noise-level (variance) hyperparameter	—
σ_f^2	Kernel amplitude (signal variance)	—

Kalman Filter (KF)

Tab. 25: List of symbols related to Kalman filter. In section 3.4, variables are presented as matrices and vectors (general case); in Chapter 6, they contain only a single value and are therefore used as scalars.

Symbol	*Name / short explanation*	*Units [mm assumed for $\boldsymbol{x}_i, \boldsymbol{u}_{i-1}$ and $\boldsymbol{z}_i$]*
$\boldsymbol{A}$	State transition model (matrix)	—
$\boldsymbol{G}$	Control-input model (matrix)	—
$\boldsymbol{H}$	Observation (measurement) model (matrix)	—

Symbol	*Name / short explanation*	*Units [mm assumed for $\boldsymbol{x}_i, \boldsymbol{u}_{i-1}$ and $\boldsymbol{z}_i$]*
$\mathcal{N}(\cdot,\cdot)$	Normal (Gaussian) distribution	—
$p(\cdot)$	Probability distribution (repeated in Tab. 24)	—
$\boldsymbol{P}$	*A posteriori* error covariance (matrix)	mm²
$\boldsymbol{P}^-$	*A priori* error covariance (matrix)	mm²
$\boldsymbol{Q}$	Process noise covariance (matrix)	mm²
$\boldsymbol{R}$	Measurement noise covariance (matrix)	mm²
$\boldsymbol{u}$	Control input (vector)	mm
$\boldsymbol{x}$	State (vector)	mm
$\hat{\boldsymbol{x}}$	*A posteriori* state estimate (vector)	mm
$\hat{\boldsymbol{x}}^-$	*A priori* state estimate (vector)	mm
$\boldsymbol{z}$	Measurement (vector)	mm
$\boldsymbol{\kappa}$	Kalman gain (matrix)	—
$\boldsymbol{\psi}$	Measurement noise (vector)	mm
$\boldsymbol{\omega}$	Process noise (vector)	mm

Optics and DIC

Tab. 26: List of symbols related to optics and DIC – general explanation.

Symbol	*Name / short explanation*	*Units*
AD	Actual distance in the distorted image (for distortion quantification)	px
$C_{CC}(\cdot)$	Cross-correlation criterion	—
$C_{SSD}(\cdot)$	Sum of squared differences criterion	—
$\mathcal{C}(\mathbb{x}_0, \mathbb{y}_0)$	Point at the subset center in the reference image.	px *(per coord.)*
$\mathcal{C}'(\mathbb{x}'_0, \mathbb{y}'_0)$	Matched point at the subset center in the deformed image.	px *(per coord.)*
$\mathbb{C}$	Image contrast	%
$d_{Rayleigh,img}$	Rayleigh diffraction limit (minimum resolvable spot spacing) in the image plane (on sensor)	nm
$d_{Rayleigh,obj}$	Rayleigh diffraction limit (minimum resolvable spot spacing) in the measured (object) plane	nm
$\boldsymbol{D}(\mathbb{u}, \mathbb{v})$	Displacement vector of the center point from the reference to the deformed image	px
D_{opt}	Optical distortion	%
D_{TV}	TV distortion	%

Symbol	*Name / short explanation*	*Units*
DH	Height deviation at the FoV edge (TV distortion)	px
DoF	Depth of field	mm
$f_{GL}(\mathbb{x}_j, \mathbb{y}_k)$	Gray level at coordinates $(\mathbb{x}_j, \mathbb{y}_k)$ in the reference image	—
$\mathbb{f}$	Lens focal length	mm
$\mathbb{f}/\#$	F-number	—
$g_{GL}(\mathbb{x}'_j, \mathbb{y}'_k)$	Gray level at coordinates $(\mathbb{x}'_j, \mathbb{y}'_k)$ in the deformed image	—
$\boldsymbol{\mathbb{h}}$	Vector of unknown parameters in the first-order shape function	—
h_{FoV}	Height of the field of view (object space)	mm
h_{sensor}	Height of the sensor	mm
h_{sub}	Height of the subset	px
H	Height of the inscribed/circumscribed rectangle in the distorted image (TV distortion)	px
$I_{opt,max}$	Peak optical intensity in an Airy-disk cross-section, e.g., as illuminance	lx
$I_{opt,min}$	Minimum optical intensity between two Airy disks, e.g., as illuminance	lx
m_{opt}	Optical magnification of the imaging system	—
n_{px}	Number of pixels in the camera sensor	—
PD	Predicted (undistorted) distance in the image	px
$Q(\mathbb{x}_j, \mathbb{y}_j)$	Arbitrarily selected point in the subset in the reference image	px *(per coord.)*
$Q'(\mathbb{x}'_j, \mathbb{y}'_j)$	Corresponding selected point in the subset in the reference image	px *(per coord.)*
s_{px}	Pixel size	mm
$\mathbb{u}$	Displacement component along $\mathbb{x}$	px
$\mathbb{v}$	Displacement component along $\mathbb{y}$	px
w_{sub}	Width of the subset	px
WD	Working distance (object–lens distance)	mm
$\mathbb{x}$	Reference image $\mathbb{x}$-coordinate	px
$\mathbb{x}'$	Deformed image $\mathbb{x}$-coordinate	px
$\mathbb{y}$	Reference image $\mathbb{y}$-coordinate	px
$\mathbb{y}'$	Deformed image $\mathbb{y}$ -coordinate	px
$\Delta\mathbb{x}$	Local offset from subset center in $\mathbb{x}$ to arbitrary subset point	px
$\Delta\mathbb{y}$	Local offset from subset center in $\mathbb{y}$ to arbitrary subset point	px
λ	Light wavelength	nm

Symbol	*Name / short explanation*	*Units*
ξ_{image}	Image spatial frequency limit (Nyquist)	lp/mm
ξ_{object}	Object-space resolution (smallest resolvable spot on object)	mm
ξ_{sensor}	Sensor spatial frequency limit (Nyquist)	lp/mm

Fatigue Crack Growth Rate

Tab. 27: List of symbols related to fatigue crack growth rate evaluation – general explanation.

Symbol	*Name / short explanation*	*Units*
a	Crack length (from notch tip to crack tip) as output of IPM, fIPM, fIPMf	mm
$\mathbb{a}$	Crack size (from center line/loading line to crack tip)	mm
$\mathbb{a}_{mid,ET}$	Crack size at the midpoint of an interval that spans the entire test	mm
$\mathbb{a}_{mid,PT}$	Crack size at the midpoint of an interval that covers only part of the test	mm
$\mathbb{a}_n$	Notch length	mm
$A_{MT,nom}$	Nominal cross-sectional area of MT specimen	mm^2
A_0, A_1, A_2, A_3	Coefficients in Newman crack-opening function $f_{NG}(R)$	—
B	Specimen thickness (standardized dimension)	mm
C_{PL}	Paris-law constant in FCGR models	$mm\left(MPa\sqrt{m}\right)^{-m_{PL}}$
$da/dN, d\mathbb{a}/dN$	Fatigue crack growth rate (FCGR) – same quantity; notation distinguishes values from IPM/fIPM/fIPMf vs. other methods.	mm/cycle
$(d\mathbb{a}/dN)_{NG}$	FCGR from NASGRO	mm/cycle
$(d\mathbb{a}/dN)_{PL}$	FCGR from Paris law	mm/cycle
$(d\mathbb{a}/dN)_{PL,mod}$	FCGR from Paris law modified form	mm/cycle
$f_{NG}(R)$	Newman crack-opening function	—
K	Stress intensity factor (SIF), Mode I	$MPa\sqrt{m}$
K_c	Critical SIF (at fracture)	$MPa\sqrt{m}$
K_{IC}	Fracture toughness	$MPa\sqrt{m}$
K_{max}	Maximum SIF in a cycle	$MPa\sqrt{m}$
K_{min}	Minimum SIF in a cycle	$MPa\sqrt{m}$
K_{op}	Crack-opening SIF (at opening onset)	$MPa\sqrt{m}$
m_{PL}	Paris-law exponent	—
N	Cycle count	—

Symbol	*Name / short explanation*	*Units*
N_{end}	Cycle count at the end of the test	—
$N_{overall}$	Cycle count for the entire test ($N_{end} - N_{start}$)	—
N_{start}	Cycle count at the beginning of the test	—
p_{NG}	NASGRO exponent governing threshold term	—
P_{a}	Amplitude of applied load (half of the load range)	N
P_{max}	Maximum applied load in a cycle	N
P_{min}	Minimum applied load in a cycle	N
q_{NG}	NASGRO exponent for fracture-toughness cutoff	—
R	Stress ratio characterizing the loading cycle	—
W	Specimen width (standardized dimension)	mm
$Y_{CT}(\alpha)$	Dimensionless geometry function for CT specimen SIF calculation	—
α	Relative crack size – normalized to specimen width	—
β	Constraint factor in Newman model	—
$\Delta a, \Delta \mathbb{a}$	Crack length/size increment over an interval, respectively	mm
Δa_{NE}	Actual crack-length increment that is not included in the FCGR evaluation after reducing the cyclic load.	mm
$\Delta \mathbb{a}_r$	Recommended (ASTM E647) crack length increment to use in FCGR evaluation	mm
$\Delta \mathbb{a}_{KD,r}$	Recommended (ASTM E647) crack length increment value for *K*-decreasing tests to use in FCGR evaluation	mm
ΔK	SIF range per cycle	$MPa\sqrt{m}$
ΔK_{CT}	SIF range per cycle for CT specimen	$MPa\sqrt{m}$
ΔK_{eff}	Effective SIF range per cycle accounting for crack closure	$MPa\sqrt{m}$
ΔK_{MT}	SIF range per cycle for MT specimen	$MPa\sqrt{m}$
ΔK_{th}	Threshold SIF range below which no fatigue crack growth occurs	$MPa\sqrt{m}$
ΔP	Load range per cycle	N
σ	Nominal far-field stress	MPa
σ_{max}	Maximum nominal far-field stress	MPa
$\sigma_{max,CT}$	Maximum nominal far-field stress for CT specimen	MPa
$\sigma_{max,MT}$	Maximum nominal far-field stress for MT specimen	MPa
σ_{min}	Minimum nominal far-field stress	MPa
σ_o	Flow stress (average of yield and ultimate strengths) in Newman model	MPa

Symbol	*Name / short explanation*	*Units*
σ_u	Ultimate strength	MPa
σ_y	Yield strength	MPa

Miscellaneous

Tab. 28: List of symbols not fitting into any other larger logical group.

Symbol	*Name / short explanation*	*Units*
a_{reg}	Linear-regression slope coefficient	mm
a_{STM}	Crack length obtained by using the Strain threshold method (STM)	mm
b_{reg}	Linear-regression intercept coefficient	mm
COD	Crack opening displacement	mm
COD_{DIC}	Opening profile used by [2018, L. Patriarca, et al.]	mm
$CTOD$	Crack-tip opening displacement	mm
I	Identity matrix	—
j	Locally used index	—
k	Locally used index	—
r	Radial distance in the polar coordinate system with the origin at the crack tip	mm
R^2	Coefficient of determination	—
v_{VO}	Displacement perpendicular to crack faces in [2019, J. M. Vasco-Olmo, et al.] setup	mm
x_{VO}	Coordinate along the crack path in [2019, J. M. Vasco-Olmo, et al.] setup	mm
$x_{VO,t}$	Horizontal crack-tip coordinate in the approach of [2019, J. M. Vasco-Olmo, et al.]	mm
y_{th}	Threshold displacement used in the deformation threshold method (DTM)	mm
y_{VO}	Coordinate perpendicular to crack faces in [2019, J. M. Vasco-Olmo, et al.] setup	mm
$y_{VO,t}$	Vertical crack-tip coordinate in the approach of [2019, J. M. Vasco-Olmo, et al.]	mm
θ	Angular distance in the polar coordinate system with the origin at the crack tip	rad
ϖ	Locally used index	—
ς	The kernel argument in GPR	—

References

[1] S. D. Antolovich, A. Saxena, and W. W. Gerberich, “Fracture mechanics – An interpretive technical history,” *Mech Res Commun*, vol. 91, pp. 46–86, Jul. 2018, doi: 10.1016/J.MECHRESCOM.2018.03.003.

[2] A. Wöhler, “Versuche über die Festigkeit der Eisenbahnwagenachsen,” *Zeitschrift für Bauwesen*, vol. 10, pp. 160–161, 1860.

[3] D. Kirkaldy, *Results of an experimental inquiry into the tensile strength and other properties of various kinds of wrought-iron and steel By David Kirkaldy*. England: Printed for and sold by the author, 1866, 1866.

[4] A. Wöhler, “Über die Festigkeitsversuche mit Eisen und Stahl,” *Zeitschrift für Bauwesen*, vol. 20, pp. 73–106, 1870.

[5] G. Charpy, “Note sur l’Essai des Métaux à la Flexion par Choc de Barreaux En-taillés, (Note on High Rate Flexion Testing of Notched Metal Bars),” *Mémoires et Comptes-Rendus de la Sociétédes Ingénieurs Civils de France*, 1901.

[6] G. Charpy, “Sur l’Essai des Metaux par Flexion de Barreaux Entaillés (The Testing of Metals by the Flexion of Notched Bars),” *Memoires de la Societédes Ingénieurs Civils de France*, 1904.

[7] C. E. Inglis, “Stresses in a plate due to the presence of cracks and sharp corners,” *Proc Inst Naval Arch*, vol. 55, pp. 219–230, 1913.

[8] A. A. Griffith, *The phenomena of rupture and flow in solids*. England, 1920.

[9] A. Griffith, “The theory of rupture,” *Proc First Int Congr Appl Mech*, pp. 55–63, 1924.

[10] B. Cotterell, “The past, present, and future of fracture mechanics,” *Eng Fract Mech*, vol. 69, no. 5, pp. 533–553, Mar. 2002, doi: 10.1016/S0013-7944(01)00101-1.

[11] G. R. Irwin, “Fracture dynamics. Fracturing of metals,” *American Society for Metals*, pp. 147–166, 1948.

[12] G. R. Irwin, “Analysis of Stresses and Strains Near the End of a Crack Traversing a Plate,” *J Appl Mech*, vol. 24, no. 3, pp. 361–364, 1957.

[13] E. Orowan, “Fracture and strength of solids,” *Reports on progress in physics*, vol. 12, no. 1, pp. 185–232, 1949.

[14] A. Wells, “Unstable crack propagation in metals: cleavage and fast fracture,” in *Proceedings of the crack propagation symposium*, 1961, p. 26028.

[15] J. R. Rice, “A Path Independent Integral and the Approximate Analysis of Strain Concentration by Notches and Cracks,” *J Appl Mech*, vol. 35, no. 2, pp. 379–386, 1968.

[16] P. C. Paris, *The growth of cracks due to variations in load*. Lehigh University, 1962.

[17] R. J. Bucci, P. C. Paris, R. W. Hertzberg, R. A. Schmidt, and A. F. Anderson, “Fatigue threshold crack propagation in air and dry argon for a Ti-6Al-4V alloy,” *ASTM STP*, vol. 513, pp. 125–140, 1972.

[18] P. Pokorný, T. Vojtek, L. Náhlík, and P. Hutař, “Crack closure in near-threshold fatigue crack propagation in railway axle steel EA4T,” *Eng Fract Mech*, vol. 185, pp. 2–19, 2017, doi: 10.1016/j.engfracmech.2017.02.013.

[19] ASTM International, “ASTM E647-23a: Standard Test Method for Measurement of Fatigue Crack Growth Rates,” 2023, *ASTM International, 100 Barr Harbor Drive, PO Box C700, West Conshohocken, PA 19428-2959, United States*.

[20] International Digital Image Correlation Society, E. M. C. Jones, and M. A. Iadicola, “A Good Practices Guide for Digital Image Correlation,” Oct. 2018, doi: 10.32720/idics/gpg.ed1.

[21] M. A. Sutton, W. J. Wolters, W. H. Peters, W. F. Ranson, and S. R. McNeill, “Determination of displacements using an improved digital correlation method,” *Image Vis Comput*, vol. 1, no. 3, pp. 133–139, 1983.

[22] J. Zhao, Y. Sang, and F. Duan, “The state of the art of two-dimensional digital image correlation computational method,” *Engineering Reports*, vol. 1, no. 2, Sep. 2019, doi: 10.1002/eng2.12038.

[23] J. Ahn, E. He, L. Chen, J. Dear, Z. Shao, and C. Davies, “In-situ micro-tensile testing of AA2024-T3 fibre laser welds with digital image correlation as a function of welding speed,” *International Journal of Lightweight Materials and Manufacture*, vol. 1, no. 3, pp. 179–188, Sep. 2018, doi: 10.1016/j.ijlmm.2018.07.003.

[24] H. Schreier, J.-J. Orteu, and M. A. Sutton, *Image Correlation for Shape, Motion and Deformation Measurements*. Boston, MA: Springer US, 2009. doi: 10.1007/978-0-387-78747-3.

[25] B. M. B. Grant, H. J. Stone, P. J. Withers, and M. Preuss, “High-temperature strain field measurement using digital image correlation,” *J Strain Anal Eng Des*, vol. 44, no. 4, pp. 263–271, May 2009, doi: 10.1243/03093247JSA478.

[26] M. Velez and Y. Gong, “Measuring the coefficient of thermal expansion of free-standing enamel films,” *Int J Appl Glass Sci*, vol. 10, no. 1, pp. 3–6, Jan. 2019, doi: 10.1111/ijag.12437.

[27] F. Hild and S. Roux, “Measuring stress intensity factors with a camera: Integrated digital image correlation (I-DIC),” *Comptes Rendus. Mécanique*, vol. 334, no. 1, pp. 8–12, Dec. 2005, doi: 10.1016/j.crme.2005.11.002.

[28] S. Seitl, L. Malíkova, J. Sobek, P. Frantík, and P. Lopez-Crespo, “Williams expansion-based approximation of the stress field in an Al 2024 body with a crack from optical measurements,” *Frattura ed Integrità Strutturale*, vol. 11, no. 41, pp. 323–331, Jun. 2017, doi: 10.3221/IGF-ESIS.41.43.

[29] Y. Li and W. Jiang, “DIC-based *J* -integral evaluation of laser repaired cracks with micro/nanomaterial addition,” *Fatigue Fract Eng Mater Struct*, vol. 42, no. 10, pp. 2262–2275, Oct. 2019, doi: 10.1111/ffe.13040.

[30] C. Chen, D. Ye, L. Zhang, and J. Liu, “DIC-based studies of the overloading effects on the fatigue crack propagation behavior of Ti-6Al-4V ELI alloy,” *Int J Fatigue*, vol. 112, pp. 153–164, Jul. 2018, doi: 10.1016/j.ijfatigue.2018.03.017.

[31] S. Gothivarekar, S. Coppieters, A. Van de Velde, and D. Debruyne, “Advanced FE model validation of cold-forming process using DIC: Air bending of high strength steel,” *International*

Journal of Material Forming, vol. 13, no. 3, pp. 409–421, May 2020, doi: 10.1007/s12289-020-01536-1.

[32] V. Sebera, L. Muszyński, J. Tippner, M. Noyel, T. Pisaneschi, and B. Sundberg, "FE analysis of CLT panel subjected to torsion and verified by DIC," *Mater Struct*, vol. 48, no. 1–2, pp. 451–459, Jan. 2015, doi: 10.1617/s11527-013-0195-1.

[33] T. J. Beberniss and D. A. Ehrhardt, "High-speed 3D digital image correlation vibration measurement: Recent advancements and noted limitations," *Mech Syst Signal Process*, vol. 86, pp. 35–48, Mar. 2017, doi: 10.1016/j.ymssp.2016.04.014.

[34] P. Neri, A. Paoli, A. V. Razionale, and C. Santus, "Low-speed cameras system for 3D-DIC vibration measurements in the kHz range," *Mech Syst Signal Process*, vol. 162, p. 108040, Jan. 2022, doi: 10.1016/j.ymssp.2021.108040.

[35] A. Saxena and S. J. Hudak Jr, "Review and extension of compliance information for common crack growth specimens," *Int J Fract*, vol. 14, no. 5, pp. 453–468, 1978.

[36] G. R. Irwin and J. A. Kies, "Critical energy rate analysis of fracture strength," *Spie Milestone series MS*, vol. 137, pp. 136–141, 1997.

[37] G. Wilkowski and W. Maxey, "Review and applications of the electric potential method for measuring crack growth in specimens, flawed pipes, and pressure vessels," in *Fourteenth National Symposium on Fracture Mechanics*, 2020, pp. 266–294.

[38] W. Deans and C. Richards, "A Simple and Sensitive Method of Monitoring Crack and Load in Compact Fracture Mechanics Specimens Using Strain Gages," *J Test Eval*, vol. 7, no. 3, pp. 147–154, May 1979, doi: 10.1520/JTE11216J.

[39] D. R. Donaldson and W. E. Anderson, "Crack propagation behavior of some airframe materials," in *Proceedings of the Crack Propagation Symposium*, 1961, pp. 375–441.

[40] P. K. Liaw, H. R. Hartmann, and E. J. Helm, "Corrosion fatigue crack propagation testing with the KRAK-GAGE® in salt water," *Eng Fract Mech*, vol. 18, no. 1, pp. 121–131, Jan. 1983, doi: 10.1016/0013-7944(83)90101-7.

[41] P. C. Paris and B. R. Hayden, "A new system for fatigue crack growth measurement and control," in *ASTM Symposium on Fatigue Crack Growth*, 1979.

[42] J. E. Srawley and W. F. Brown, *Fracture toughness testing*, vol. 52030. National Aeronautics and Space Administration, 1965.

[43] A. M. Sullivan and T. W. Crooker, "A crack-opening-displacement technique for crack length measurement in fatigue crack growth rate testing—development and evaluation," *Eng Fract Mech*, vol. 9, no. 1, pp. 159–166, 1977.

[44] ČSN ISO 12108, "Kovové materiály - Zkoušení únavy - Metoda růstu únavové trhliny," *Česká agentura pro standardizaci*, 2019.

[45] ČSN ISO 12135, "Kovové materiály - Jednotná metoda zkoušky pro určení kvazistatické lomové houževnatosti.," *Česká agentura pro standardizaci*, 2018.

[46] ASTM E 1820, "Standard Test Method for Measurement of Fracture Toughness," *ASTM*

International, 2015.

[47] W. G. Clark and L. J. Ceschini, "Fatigue precracking of spin-burst toughness specimens," *Exp Mech*, vol. 9, no. 3, pp. 123–128, Mar. 1969, doi: 10.1007/BF02327698.

[48] C. A. Middleton, A. Gaio, R. J. Greene, and E. A. Patterson, "Towards Automated Tracking of Initiation and Propagation of Cracks in Aluminium Alloy Coupons Using Thermoelastic Stress Analysis," *J Nondestr Eval*, vol. 38, no. 1, p. 18, Mar. 2019, doi: 10.1007/s10921-018-0555-4.

[49] B. V. Farahani, F. Direito, P. J. Sousa, P. J. Tavares, and P. M. P. G. Moreira, "Electronic Speckle Pattern Interferometry for fatigue crack monitoring," *Procedia Structural Integrity*, vol. 37, pp. 873–879, 2022, doi: 10.1016/j.prostr.2022.02.021.

[50] A. J. Rosakis and K. Ravi-Chandar, "On crack-tip stress state: An experimental evaluation of three-dimensional effects," *Int J Solids Struct*, vol. 22, no. 2, pp. 121–134, 1986, doi: 10.1016/0020-7683(86)90002-8.

[51] D. NOWELL, R. J. H. PAYNTER, and P. F. P. DE MATOS, "Optical methods for measurement of fatigue crack closure: moiré interferometry and digital image correlation," *Fatigue Fract Eng Mater Struct*, vol. 33, no. 12, pp. 778–790, Dec. 2010, doi: 10.1111/j.1460-2695.2010.01447.x.

[52] E. A. PATTERSON and E. J. OLDEN, "Optical analysis of crack tip stress fields: a comparative study," *Fatigue Fract Eng Mater Struct*, vol. 27, no. 7, pp. 623–635, Jul. 2004, doi: 10.1111/j.1460-2695.2004.00774.x.

[53] W. Zhou *et al.*, "Study of Crack Growth of Transparent Materials Subjected to Laser Irradiation by Digital Holography," *Applied Sciences*, vol. 12, no. 15, p. 7799, Aug. 2022, doi: 10.3390/app12157799.

[54] F. Mathieu, F. Hild, and S. Roux, "Identification of a crack propagation law by digital image correlation," *Int J Fatigue*, vol. 36, no. 1, pp. 146–154, Mar. 2012, doi: 10.1016/j.ijfatigue.2011.08.004.

[55] M. L. Williams, "On the Stress Distribution at the Base of a Stationary Crack," *J Appl Mech*, vol. 24, no. 1, pp. 109–114, Mar. 1957, doi: 10.1115/1.4011454.

[56] J. Abanto-Bueno and J. Lambros, "Investigation of crack growth in functionally graded materials using digital image correlation," *Eng Fract Mech*, vol. 69, no. 14–16, pp. 1695–1711, Sep. 2002, doi: 10.1016/S0013-7944(02)00058-9.

[57] J. R. Yates, M. Zanganeh, and Y. H. Tai, "Quantifying crack tip displacement fields with DIC," *Eng Fract Mech*, vol. 77, no. 11, pp. 2063–2076, Jul. 2010, doi: 10.1016/j.engfracmech.2010.03.025.

[58] J. Réthoré, F. Hild, and S. Roux, "Extended digital image correlation with crack shape optimization," *Int J Numer Methods Eng*, vol. 73, no. 2, pp. 248–272, Jan. 2008, doi: 10.1002/nme.2070.

[59] S. Roux, J. Réthoré, and F. Hild, "Digital image correlation and fracture: an advanced technique for estimating stress intensity factors of 2D and 3D cracks," *J Phys D Appl Phys*, vol. 42, no. 21, p. 214004, Nov. 2009, doi: 10.1088/0022-3727/42/21/214004.

[60] E. Fagerholt, E. Østby, T. Børvik, and O. S. Hopperstad, "Investigation of fracture in small-scale

SENT tests of a welded X80 pipeline steel using Digital Image Correlation with node splitting," *Eng Fract Mech*, vol. 96, pp. 276–293, Dec. 2012, doi: 10.1016/j.engfracmech.2012.08.007.

[61] J. D. Carroll, W. Abuzaid, J. Lambros, and H. Sehitoglu, "High resolution digital image correlation measurements of strain accumulation in fatigue crack growth," *Int J Fatigue*, vol. 57, pp. 140–150, Dec. 2013, doi: 10.1016/j.ijfatigue.2012.06.010.

[62] E. Mündecke and V. Mechtcherine, "Tensile behaviour of strain-hardening cement-based composites (SHCC) with steel reinforcing bars," *Cem Concr Compos*, vol. 105, p. 103423, Jan. 2020, doi: 10.1016/j.cemconcomp.2019.103423.

[63] G. Ruocci *et al.*, "Digital Image Correlation and Noise-filtering Approach for the Cracking Assessment of Massive Reinforced Concrete Structures," *Strain*, vol. 52, no. 6, pp. 503–521, Dec. 2016, doi: 10.1111/str.12192.

[64] N. Gehri, J. Mata-Falcón, and W. Kaufmann, "Automated crack detection and measurement based on digital image correlation," *Constr Build Mater*, vol. 256, p. 119383, Sep. 2020, doi: 10.1016/j.conbuildmat.2020.119383.

[65] W. Dong, Z. Wu, X. Zhou, N. Wang, and G. Kastiukas, "An experimental study on crack propagation at rock-concrete interface using digital image correlation technique," *Eng Fract Mech*, vol. 171, pp. 50–63, Feb. 2017, doi: 10.1016/j.engfracmech.2016.12.003.

[66] S. Y. Alam, A. Loukili, and F. Grondin, "Monitoring size effect on crack opening in concrete by digital image correlation," *European Journal of Environmental and Civil Engineering*, vol. 16, no. 7, pp. 818–836, Jul. 2012, doi: 10.1080/19648189.2012.672211.

[67] B. Omondi, D. G. Aggelis, H. Sol, and C. Sitters, "Improved crack monitoring in structural concrete by combined acoustic emission and digital image correlation techniques," *Struct Health Monit*, vol. 15, no. 3, pp. 359–378, May 2016, doi: 10.1177/1475921716636806.

[68] P. López-Crespo, R. L. Burguete, E. A. Patterson, A. Shterenlikht, P. J. Withers, and J. R. Yates, "Study of a Crack at a Fastener Hole by Digital Image Correlation," *Exp Mech*, vol. 49, no. 4, pp. 551–559, Aug. 2009, doi: 10.1007/s11340-008-9161-1.

[69] S. Vanlanduit, J. Vanherzeele, R. Longo, and P. Guillaume, "A digital image correlation method for fatigue test experiments," *Opt Lasers Eng*, vol. 47, no. 3–4, pp. 371–378, Mar. 2009, doi: 10.1016/j.optlaseng.2008.03.016.

[70] A. Rezaie, R. Achanta, M. Godio, and K. Beyer, "Comparison of crack segmentation using digital image correlation measurements and deep learning," *Constr Build Mater*, vol. 261, p. 120474, Nov. 2020, doi: 10.1016/j.conbuildmat.2020.120474.

[71] J. M. Vasco-Olmo, F. A. Díaz, F. V. Antunes, and M. N. James, "Characterisation of fatigue crack growth using digital image correlation measurements of plastic CTOD," *Theoretical and Applied Fracture Mechanics*, vol. 101, pp. 332–341, Jun. 2019, doi: 10.1016/j.tafmec.2019.03.009.

[72] E. Durif, M. Fregonese, J. Rethore, and A. Combescure, "Development of a Digital Image Correlation controlled fatigue crack propagation experiment," *EPJ Web Conf*, vol. 6, p. 31012, Jun. 2010, doi: 10.1051/epjconf/20100631012.

[73] S. J. O'Connor, D. Nowell, and K. I. Dragnevski, "Measurement of fatigue crack deformation on the macro- and micro-scale: Uniform and non-uniform loading," *Int J Fatigue*, vol. 89, pp. 66–76, Aug. 2016, doi: 10.1016/j.ijfatigue.2016.02.032.

[74] J. Carroll *et al.*, "Investigation of fatigue crack closure using multiscale image correlation experiments," *Eng Fract Mech*, vol. 76, no. 15, pp. 2384–2398, Oct. 2009, doi: 10.1016/j.engfracmech.2009.08.002.

[75] D. NOWELL, M. E. KARTAL, and P. F. P. DE MATOS, "Digital image correlation measurement of near-tip fatigue crack displacement fields: constant amplitude loading and load history effects," *Fatigue Fract Eng Mater Struct*, vol. 36, no. 1, pp. 3–13, Jan. 2013, doi: 10.1111/j.1460-2695.2012.01707.x.

[76] S. Rabbolini, S. Beretta, and S. Foletti, "Fatigue crack growth in low cycle fatigue: an analysis of crack closure based on image correlation," *Procedia Structural Integrity*, vol. 1, pp. 158–165, 2016, doi: 10.1016/j.prostr.2016.02.022.

[77] C. M. Stewart and E. Garcia, "Fatigue crack growth of a hot mix asphalt using digital image correlation," *Int J Fatigue*, vol. 120, pp. 254–266, Mar. 2019, doi: 10.1016/j.ijfatigue.2018.11.024.

[78] M. Besel and E. Breitbarth, "Advanced analysis of crack tip plastic zone under cyclic loading," *Int J Fatigue*, vol. 93, pp. 92–108, Dec. 2016, doi: 10.1016/j.ijfatigue.2016.08.013.

[79] B. Ščerba, T. Adamec, P. Pokorný, T. Návrat, M. Vajdák, and L. Náhlík, "Inflection point principle combined with digital image correlation and machine learning for crack length measurement in fatigue tests," *Theoretical and Applied Fracture Mechanics*, vol. 139, p. 105052, Oct. 2025, doi: 10.1016/j.tafmec.2025.105052.

[80] L. Patriarca, S. Foletti, and S. Beretta, "A comparison of DIC-based techniques to measure crack closure in LCF," *Theoretical and Applied Fracture Mechanics*, vol. 98, pp. 230–243, Dec. 2018, doi: 10.1016/j.tafmec.2018.09.020.

[81] Imetrum, "Crack Length Gauge: identifying the threshold value for DCB specimens," 2022. Accessed: Dec. 02, 2023. [Online]. Available: https://support.imetrum.com/support/solutions/articles/80001044765-crack-length-gauge-identifying-the-threshold-value-for-dcb-specimens

[82] X-Sight, "ALPHA DIC SOFTWARE MODULES: CRACK PROBE." Accessed: Dec. 02, 2023. [Online]. Available: https://www.xsight.eu/alpha-digital-image-correlation-software-modules/#CL

[83] G. I. Barenblatt, "The Mathematical Theory of Equilibrium Cracks in Brittle Fracture," *Advances in Applied Mechanics*, vol. 7, pp. 55–129, 1962, doi: https://doi.org/10.1016/S0065-2156(08)70121-2.

[84] D. S. Dugdale, "Yielding of steel sheets containing slits," *J Mech Phys Solids*, vol. 8, no. 2, pp. 100–104, May 1960, doi: 10.1016/0022-5096(60)90013-2.

[85] J. J. Zhang, "Chapter 4 - Basic rock fracture mechanics," in *Applied Petroleum Geomechanics*, J. J. Zhang, Ed., Gulf Professional Publishing, 2019, pp. 133–161. doi:

https://doi.org/10.1016/B978-0-12-814814-3.00004-6.

[86] H. Askes and E. C. Aifantis, “Gradient elasticity in statics and dynamics: An overview of formulations, length scale identification procedures, finite element implementations and new results,” *Int J Solids Struct*, vol. 48, no. 13, pp. 1962–1990, Jun. 2011, doi: 10.1016/j.ijsolstr.2011.03.006.

[87] G. Sciarra and S. Vidoli, “Asymptotic Fracture Modes in Strain-Gradient Elasticity: Size Effects and Characteristic Lengths for Isotropic Materials,” *J Elast*, vol. 113, no. 1, pp. 27–53, Sep. 2013, doi: 10.1007/s10659-012-9409-y.

[88] P. Skalka, P. Navrátil, and M. Kotoul, “Novel approach to FE solution of crack problems in the Laplacian-based gradient elasticity,” *Mechanics of Materials*, vol. 95, pp. 28–48, Apr. 2016, doi: 10.1016/j.mechmat.2015.12.007.

[89] T. L. Anderson, *Fracture Mechanics: Fundamentals and Applications, Third Edition*, 3rd ed. CRC Press, 2005.

[90] M. Kotoul *et al.*, “Ab initio aided strain gradient elasticity theory in prediction of nanocomponent fracture,” *Mechanics of Materials*, vol. 136, p. 103074, Sep. 2019, doi: 10.1016/j.mechmat.2019.103074.

[91] A. Gosch, J. Geier, F. Arbeiter, M. Berer, and G. Pinter, “Methods for automated crack length detection in fracture mechanical fatigue tests of unreinforced polymers,” *Procedia Structural Integrity*, vol. 28, pp. 1184–1192, 2020, doi: 10.1016/j.prostr.2020.11.100.

[92] B. K. Bay, T. S. Smith, D. P. Fyhrie, and M. Saad, “Digital volume correlation: Three-dimensional strain mapping using X-ray tomography,” *Exp Mech*, vol. 39, no. 3, pp. 217–226, Sep. 1999, doi: 10.1007/BF02323555.

[93] W. Lepage, “A practical guide to DIC,” *Digitalimagecorrelation.org. Tulsa: The University of Tulsa*, Accessed: Jul. 24, 2025. [Online]. Available: https://digitalimagecorrelation.org/

[94] G. Hollows and N. James, “System Throughput, f/#, and Numerical Aperture,” Edmund Optics Knowledge Center. Accessed: Jul. 24, 2025. [Online]. Available: https://digitalimagecorrelation.org/

[95] Correlated Solutions, “Digital Image Correlation: Overview of Principles and Software,” Correlated Solutions, Incorporated. Accessed: Jul. 24, 2025. [Online]. Available: https://downloads.correlatedsolutions.com/condensed-shortcourse.pdf

[96] G. Hollows and N. James, “The Advantages of Telecentricity,” Edmund Optics Knowledge Center. Accessed: Jul. 24, 2025. [Online]. Available: https://www.edmundoptics.com/knowledge-center/application-notes/imaging/advantages-of-telecentricity/

[97] G. Hollows and N. James, “Telecentric Design Topics,” Edmund Optics Knowledge Center. Accessed: Jul. 24, 2025. [Online]. Available: https://www.edmundoptics.com/knowledge-center/application-notes/imaging/telecentric-design-topics/

[98] G. Hollows and N. James, “Distortion and Telecentricity,” Edmund Optics Knowledge Center. Accessed: Feb. 07, 2024. [Online]. Available: https://www.edmundoptics.com/knowledge-

center/application-notes/imaging/distortion-and-the-telecentricity-specification/

[99] R. Štourač, "Telecelentrický objektiv - přednosti a charakteristiky," Kinalisoft s.r.o. Accessed: Jul. 24, 2025. [Online]. Available: https://www.prumysloveobjektivy.cz/pages/view/telecelentricky-objektiv-prednosti-a-charakteristiky

[100] G. Hollows and N. James, "Telecentric Lens Size Control," Edmund Optics Knowledge Center. Accessed: Jul. 24, 2025. [Online]. Available: https://www.edmundoptics.com/knowledge-center/application-notes/imaging/telecentric-lens-size-control/

[101] G. Hollows and N. James, "Resolution," Edmund Optics Knowledge Center. Accessed: Jul. 24, 2025. [Online]. Available: https://www.edmundoptics.com/knowledge-center/application-notes/imaging/resolution/

[102] K. Weisshart, " The Basic Principle of Airyscanning," Carl Zeiss Microscopy GmbH. Accessed: Jul. 24, 2025. [Online]. Available: https://pages.zeiss.com/rs/896-XMS-794/images/ZEISS-Microscopy_The-Basic-Principle-of-Airyscanning.pdf

[103] G. Hollows and N. James, "Contrast," *Edmund Optics Knowledge Center*, Accessed: Jul. 24, 2025. [Online]. Available: https://www.edmundoptics.com/knowledge-center/application-notes/imaging/contrast/

[104] EDMUND OPTICS, "Introduction to Modulation Transfer Function," *EO: Edmund optics*, Accessed: Jul. 24, 2025. [Online]. Available: https://www.edmundoptics.eu/knowledge-center/application-notes/optics/introduction-to-modulation-transfer-function/

[105] F. Devernay and O. Faugeras, "Straight lines have to be straight," *Mach Vis Appl*, vol. 13, no. 1, pp. 14–24, Aug. 2001, doi: 10.1007/PL00013269.

[106] S. YONEYAMA, A. KITAGAWA, K. KITAMURA, and H. KIKUTA, "In-Plane Displacement Measurement Using Digital Image Correlation with Lens Distortion Correction," *JSME International Journal Series A*, vol. 49, no. 3, pp. 458–467, 2006, doi: 10.1299/jsmea.49.458.

[107] G. B. Ikokou and J. Smit, "HYPERBOLIC DISTORTION MODEL FOR RADIAL DISTORTION CORRECTION," *The International Archives of the Photogrammetry, Remote Sensing and Spatial Information Sciences*, vol. XLII-2/W13, pp. 1667–1671, Jun. 2019, doi: 10.5194/isprs-archives-XLII-2-W13-1667-2019.

[108] G. Hollows and N. James, "Distortion," *Edmund Optics Knowledge Center*, Accessed: Jul. 24, 2025. [Online]. Available: https://www.edmundoptics.com/knowledge-center/application-notes/imaging/distortion/

[109] Image Engineering, "Distortion," IMAGE ENGINEERING GMBH & CO. KG. Accessed: Jul. 24, 2025. [Online]. Available: https://www.image-engineering.de/library/image-quality/factors/1062-distortion

[110] B. Pan, K. Qian, H. Xie, and A. Asundi, "Two-dimensional digital image correlation for in-plane displacement and strain measurement: a review," *Meas Sci Technol*, vol. 20, no. 6, p. 062001, Jun. 2009, doi: 10.1088/0957-0233/20/6/062001.

[111] H. Lu and P. D. Cary, "Deformation measurements by digital image correlation: Implementation

of a second-order displacement gradient," *Exp Mech*, vol. 40, no. 4, pp. 393–400, Dec. 2000, doi: 10.1007/BF02326485.

[112] S. Yaofeng and J. H. L. Pang, "Study of optimal subset size in digital image correlation of speckle pattern images," *Opt Lasers Eng*, vol. 45, no. 9, pp. 967–974, Sep. 2007, doi: 10.1016/j.optlaseng.2007.01.012.

[113] B. Pan, H. Xie, Z. Wang, K. Qian, and Z. Wang, "Study on subset size selection in digital image correlation for speckle patterns," *Opt Express*, vol. 16, no. 10, p. 7037, May 2008, doi: 10.1364/OE.16.007037.

[114] P. Reu, "All about speckles: Speckle Size Measurement," *Exp Tech*, vol. 38, no. 6, pp. 1–2, Nov. 2014, doi: 10.1111/ext.12110.

[115] M. A. Sutton, J. H. Yan, V. Tiwari, H. W. Schreier, and J. J. Orteu, "The effect of out-of-plane motion on 2D and 3D digital image correlation measurements," *Opt Lasers Eng*, vol. 46, no. 10, pp. 746–757, Oct. 2008, doi: 10.1016/j.optlaseng.2008.05.005.

[116] S. Ma, J. Pang, and Q. Ma, "The systematic error in digital image correlation induced by self-heating of a digital camera," *Meas Sci Technol*, vol. 23, no. 2, p. 025403, Feb. 2012, doi: 10.1088/0957-0233/23/2/025403.

[117] C. E. Rasmussen and C. K. I. Williams, *Gaussian Processes for Machine Learning*. The MIT Press, 2005. doi: 10.7551/mitpress/3206.001.0001.

[118] J. Wang, "An Intuitive Tutorial to Gaussian Process Regression," *Comput Sci Eng*, vol. 25, no. 4, pp. 4–11, Jul. 2023, doi: 10.1109/MCSE.2023.3342149.

[119] "Scikit-learn: Machine Learning in Python," Scikit-learn. Accessed: Jul. 24, 2025. [Online]. Available: https://scikit-learn.org/

[120] Z. Liu, C. Lyu, J. Huo, S. Wang, and J. Chen, "Gaussian Process Regression for Transportation System Estimation and Prediction Problems: The Deformation and a Hat Kernel," *IEEE Transactions on Intelligent Transportation Systems*, vol. 23, no. 11, pp. 22331–22342, Nov. 2022, doi: 10.1109/TITS.2022.3155527.

[121] R. H. Byrd, P. Lu, J. Nocedal, and C. Zhu, "A Limited Memory Algorithm for Bound Constrained Optimization," *SIAM Journal on Scientific Computing*, vol. 16, no. 5, pp. 1190–1208, Sep. 1995, doi: 10.1137/0916069.

[122] scikit-learn developers, "Gaussian Processes." Accessed: Jan. 18, 2024. [Online]. Available: https://scikit-learn.org/stable/modules/gaussian_process.html

[123] R. E. Kalman, "A New Approach to Linear Filtering and Prediction Problems," *Journal of Basic Engineering*, vol. 82, no. 1, pp. 35–45, Mar. 1960, doi: 10.1115/1.3662552.

[124] M. Khodarahmi and V. Maihami, "A Review on Kalman Filter Models," *Archives of Computational Methods in Engineering*, vol. 30, no. 1, pp. 727–747, Jan. 2023, doi: 10.1007/s11831-022-09815-7.

[125] G. Welch and G. Bishop, "An Introduction to the Kalman Filter," University of North Carolina at Chapel Hill, 2006. Accessed: Aug. 08, 2025. [Online]. Available: https://www.cs.unc.edu/~welch/media/pdf/kalman_intro.pdf

[126] “Terminology Relating to Fatigue and Fracture Testing,” Feb. 01, 2023, *ASTM International, West Conshohocken, PA*. doi: 10.1520/E1823-23.

[127] R. G. Forman and S. R. Mettu, “Behavior of surface and corner cracks subjected to tensile and bending loads in Ti-6Al-4V alloy,” Aug. 1990. [Online]. Available: https://www.osti.gov/biblio/5555321

[128] “Development of the NASA/FLAGRO computer program for analysis of airframe structures,” Sep. 1994. Accessed: Aug. 18, 2025. [Online]. Available: https://ntrs.nasa.gov/citations/19950008059

[129] J. C. Newman, “A crack opening stress equation for fatigue crack growth,” *Int J Fract*, vol. 24, no. 4, pp. R131–R135, Apr. 1984, doi: 10.1007/BF00020751.

[130] M. A. Sutton, “Digital Image Correlation for Shape and Deformation Measurements,” 2008, pp. 565–600. doi: 10.1007/978-0-387-30877-7_20.

[131] M. Schmid, D. Rath, and U. Diebold, “Why and How Savitzky–Golay Filters Should Be Replaced,” *ACS Measurement Science Au*, vol. 2, no. 2, pp. 185–196, Apr. 2022, doi: 10.1021/acsmeasuresciau.1c00054.

[132] P. S. Palar, K. Zakaria, L. R. Zuhal, K. Shimoyama, and R. P. Liem, “Gaussian Processes and Support Vector Regression for Uncertainty Quantification in Aerodynamics,” in *AIAA Scitech 2021 Forum*, Reston, Virginia: American Institute of Aeronautics and Astronautics, Jan. 2021. doi: 10.2514/6.2021-0181.

[133] S. S. Hossain, B. V. Ayodele, S. S. Ali, C. K. Cheng, and S. I. Mustapa, “Comparative Analysis of Support Vector Machine Regression and Gaussian Process Regression in Modeling Hydrogen Production from Waste Effluent,” *Sustainability*, vol. 14, no. 12, p. 7245, Jun. 2022, doi: 10.3390/su14127245.

[134] A. Botchkarev, “Performance Metrics (Error Measures) in Machine Learning Regression, Forecasting and Prognostics: Properties and Typology,” *arXiv.org*, 2018, doi: 10.48550/arxiv.1809.03006.

[135] V. Plevris, G. Solorzano, N. P. Bakas, and M. E. A. Ben Seghier, “Investigation of performance metrics in regression analysis and machine learning-based prediction models,” European Community on Computational Methods in Applied Sciences, 2022. doi: 10.23967/eccomas.2022.155.

[136] J. Baek, J. Choi, and H. Jung, “Filtering Correction Method and Performance Comparison for Time Series Data,” *Journal of information and communication convergence engineering*, vol. 20, no. 2, pp. 125–130, 2022, Accessed: Aug. 08, 2025. [Online]. Available: https://doi.org/10.6109/jicce.2022.20.2.125

[137] N. Borhan, I. Saleh, and W. Rahiman, “Comparative Analysis of Filtering Techniques for AGV Indoor Localization with Ultra-Wideband Technology,” *Pertanika J Sci Technol*, vol. 32, no. 5, pp. 2151–2164, Aug. 2024, doi: 10.47836/pjst.32.5.13.

[138] R. Rajagopalan, “Generalized causal moving average (GCMA) smoothing filter for real-time applications,” F. T. Luk, Ed., Dec. 2003, p. 426. doi: 10.1117/12.509703.

[139] C. K. Chui and G. Chen, *Kalman Filtering*. Cham: Springer International Publishing, 2017. doi: 10.1007/978-3-319-47612-4.

[140] Q. Li, R. Li, K. Ji, and W. Dai, "Kalman Filter and Its Application," in *2015 8th International Conference on Intelligent Networks and Intelligent Systems (ICINIS)*, IEEE, Nov. 2015, pp. 74–77. doi: 10.1109/ICINIS.2015.35.

[141] A. H. Mohamed and K. P. Schwarz, "Adaptive Kalman Filtering for INS/GPS," *J Geod*, vol. 73, no. 4, pp. 193–203, May 1999, doi: 10.1007/s001900050236.

[142] A. Almagbile, J. Wang, and W. Ding, "Evaluating the Performances of Adaptive Kalman Filter Methods in GPS/INS Integration," *Journal of Global Positioning Systems*, vol. 9, no. 1, pp. 33–40, Jun. 2010, doi: 10.5081/jgps.9.1.33.

[143] S. Akhlaghi, N. Zhou, and Z. Huang, "Adaptive adjustment of noise covariance in Kalman filter for dynamic state estimation," in *2017 IEEE Power & Energy Society General Meeting*, IEEE, Jul. 2017, pp. 1–5. doi: 10.1109/PESGM.2017.8273755.

[144] T. Akiba, S. Sano, T. Yanase, T. Ohta, and M. Koyama, "Optuna: A Next-generation Hyperparameter Optimization Framework," *KDD 2019 Applied Data Science track*, Jul. 2019, Accessed: Aug. 12, 2025. [Online]. Available: https://doi.org/10.48550/arXiv.1907.10902

[145] "ČSN EN 10025-2 (420904)," *Technické normy ČSN*, Nov. 2020.

[146] T. Comlekci, J. M. Pérez, L. Milne, Y. Gorash, and D. Mackenzie, "Structural steel crack propagation experimental and numerical analysis," *Procedia Structural Integrity*, vol. 42, pp. 694–701, 2022, doi: 10.1016/j.prostr.2022.12.088.

[147] S. Seitl, P. Pokorný, P. Miarka, J. Klusák, Z. Kala, and L. Kunz, "Comparison of fatigue crack propagation behaviour in two steel grades S235, S355 and a steel from old crane way," *MATEC Web of Conferences*, vol. 310, p. 00034, Mar. 2020, doi: 10.1051/matecconf/202031000034.

[148] D. L. Carvalho, A. L. L. Silva, A. M. P. de Jesus, and A. A. Fernandes, "FATIGUE BEHAVIOUR OF STRUCTURAL STEELS. COMPARISON OF STRAIN-LIFE AND FATIGUE CRACK PROPAGATION DATA COMPORTAMENTO À FADIGA DE AÇOS ESTRUTURAIS. RELAÇÕES DEFORMAÇÃO-VIDA E TAXAS DE PROPAGAÇÃO DE," 2015. [Online]. Available: https://api.semanticscholar.org/CorpusID:208304334

[149] S. Kalnaus, F. Fan, Y. Jiang, and A. K. Vasudevan, "An experimental investigation of fatigue crack growth of stainless steel 304L," *Int J Fatigue*, vol. 31, no. 5, pp. 840–849, May 2009, doi: 10.1016/j.ijfatigue.2008.11.004.

[150] M. Subasic, B. Alfredsson, C. F. O. Dahlberg, M. Öberg, and P. Efsing, "Mechanical Characterization of Fatigue and Cyclic Plasticity of 304L Stainless Steel at Elevated Temperature," *Exp Mech*, vol. 63, no. 8, pp. 1391–1407, Oct. 2023, doi: 10.1007/s11340-023-00992-5.

[151] S. Seitl, P. Pokorný, J. Klusák, S. Duda, and G. Lesiuk, "Effect of Specimen Thickness on Fatigue Crack Growth Resistance in Paris Region in AISI 304 STEEL," 2022, pp. 291–297. doi: 10.1007/978-3-030-97822-8_34.

[152] N. Nagaishi, M. Yoshikawa, S. Okazaki, J. Yamabe, F. Yoshida, and H. Matsunaga, "Evaluation

of fatigue life and fatigue limit of circumferentially-notched Type 304 stainless steel in air and hydrogen gas based on crack-growth property and cyclic stress-strain response," *Eng Fract Mech*, vol. 215, pp. 164–177, Jun. 2019, doi: 10.1016/j.engfracmech.2019.05.005.

[153] Teledyne FLIR LLC, "Blackfly S USB3." Accessed: Nov. 16, 2023. [Online]. Available: https://www.flir.com/products/blackfly-s-usb3/

[154] N. Moës, J. Dolbow, and T. Belytschko, "A finite element method for crack growth without remeshing," *Int J Numer Methods Eng*, vol. 46, no. 1, pp. 131–150, Sep. 1999, doi: 10.1002/(SICI)1097-0207(19990910)46:1<131::AID-NME726>3.0.CO;2-J.

[155] I. Sobel and G. Feldman, *An Isotropic 3x3 Image Gradient Operator*. 2015. doi: 10.13140/RG.2.1.1912.4965.

[156] V. Veselý, J. Sobek, L. Šestáková, P. Frantík, and S. Seitl, "Multi-parameter crack tip stress state description for estimation of fracture process zone extent in silicate composite WST specimens," *Frattura ed Integrità Strutturale*, vol. 7, no. 25, pp. 69–78, Apr. 2013, doi: 10.3221/IGF-ESIS.25.11.

[157] C. W. Lim, G. Zhang, and J. N. Reddy, "A higher-order nonlocal elasticity and strain gradient theory and its applications in wave propagation," *J Mech Phys Solids*, vol. 78, pp. 298–313, May 2015, doi: 10.1016/j.jmps.2015.02.001.

[158] THE INTERNATIONAL SOCIETY FOR OPTICS AND PHOTONICS, "Marginal and Chief Rays," THE INTERNATIONAL SOCIETY FOR OPTICS AND PHOTONICS. Optipedia • SPIE Press books opened for your reference. Accessed: Jul. 24, 2025. [Online]. Available: https://spie.org/publications/spie-publication-resources/optipedia-free-optics-information/pm92_161_marginal_chief_rays

[159] R. Kumar, "What are Global Shutter and Rolling shutter Cameras? How to choose the one that fits the application?," E-con Systems: Think Camera. Accessed: Jul. 24, 2025. [Online]. Available: https://www.e-consystems.com/blog/camera/technology/what-are-global-shutter-and-rolling-shutter-how-to-choose-the-one-that-fits-the-application/

[160] CBC GROUP, "Machine Vision Lens M1628-MPW3," Computar. Accessed: Jul. 24, 2025. [Online]. Available: https://www.computar.com/products/m1628-mpw3

[161] OPTO ENGINEERING, "TCLWD series: 132 mm working distance telecentric lenses for sensors up to 2/3"." Accessed: Jul. 24, 2025. [Online]. Available: https://www.opto-e.com/en/products/tclwd-series